A Study of High Transverse Momentum

Eta Meson Production

by

Dana Duane Skow

Submitted in Partial Fulfillment

of the

Requirements for the Degree

DOCTOR OF PHILOSOPHY

Supervised by: Professor Frederick Lobkowicz

Department of Physics and Astronomy
College of Arts and Sciences

University of Rochester

Rochester, New York

1990

CURRICULUM VITAE

Dana Duane Skow

The author ███████████████████████████
He has lived in ██████████████████████████████████████
██ He
considers himself an Iowan.

In 1979, the author enrolled in a 3-2 chemical engineering program at Augustana College in Rock Island, Illinois. After three years he was elected Student Government President at Augustana and Brown Fellow at Washington University, St. Louis. In the choice between the two institutions, politics won out and the author spent 1983 at Augustana, graduating valedictorian, with a bachelor's degree in Physics and Mathematics ... and courting his future wife. At Augustana he was elected to Phi Beta Kappa, Sigma Pi Sigma, Omicron Delta Kappa, Mortar Board, and Gamma Alpha Beta fraternities.

After graduating from Augustana, the author was ████████████████████
███████████████████████████ for the summer preceeding his enrollment at the University of Rochester in Rochester, New York. At Rochester, he was named a Rush Rhees Fellow and began working on E706 as a research assistant with professors Tom Ferbel, Fred Lobkowicz, and Paul Slattery. A simple statement, "I know how to turn on a scope," destined him to spend the next five years developing, testing, building, inspecting, installing, operating, debugging, maintaining and documenting the readout electronics for the Liquid Argon Calorimeter used in E706.

Acknowledgements

Where to begin.... I must thank my parents for their support and encouragement throughout the years...as well the hundreds of people who had a hand in guiding my schooling.

I'd like to thank my collaborators on E706, especially the postdocs and my fellow grad students with whom I've shared this experience and from whom I've learned so much. At the University of Rochester, I thank Fred Lobkowicz, Tom Ferbel, and Paul Slattery for sharpening my wit and toughening my hide. Bettys Cook and Bauer helped me tie my shoes and survive the realities of bureaucracy. I owe a special debt to Tom Droege, Charlie Nelson and the rest of the PIGs for teaching me what electronics I know and adopting me into their fold (sty?).

Several people made important contributions to the success of E706 whose name will not appear on the lists of authors for our papers. These include: Domingo Andreuzzi, Frank Bally, Ed Barsotti, Ernie Buchanan, Lou Dalmonte, Joan Collins, Greg Deuerling, Cheng Chang Dong, Bud Dickerson, Ethel Heflin, Tom Haelen, Kevin Jenkins, Dinesh Kaul, Larry Kuntz, Gene Olson, Mindy Pickett, Del Venture, Merle Watson, and many others. To these individuals I give my hearty thanks and appreciation.

To Chris Lirakis, John Mansour, Eric Prebys, George Ginther, and George Alverson, go heartfelt thanks for their friendship and advice throughout the many days when the end seemed SO far away. With them, the drudgery was bearable and the excitement enhanced, without them, life would not have been so pleasant.

Finally, and most importantly, I'd like to acknowledge my wife Nancy for her love, support and attention. My daughter Emily helped to brighten up the gray tiring days. And you, Allison Kendra, receive the dedication of this thesis.

Abstract

Production of high transverse momentum (p_T) η (eta) mesons by hadron beams with incident momentum of 530 GeV/c ($\sqrt{s} = 31.6$ GeV) has been measured using the E706 spectrometer at FNAL. The $\gamma\gamma$ decay mode was studied using data from the highly segmented liquid argon calorimeter in E706. Results are presented for inclusive η production for π^- and p beams on a beryllium target, and compared to inclusive π° production. Data cover the range of transverse momentum of $3.5 < p_T < 10$ GeV/c and rapidity $|y| < 0.7$. The integrated ratio of inclusive η production for incident K^- and π^- at 530 GeV/c ($K^- Be \rightarrow \eta X / \pi^- Be \rightarrow \eta X$) was found to be 1.32 ± 0.32 measured for the range $3.5 < 6.0$ GeV/c with rapidity $|y| < 1.0$.

Table of Contents

FIGURE CAPTIONS

TABLE CAPTIONS

1. Introduction

This thesis presents results from data taken during the 1987–8 data run of

Fermi National Accelerator Laboratory (FNAL) Experiment 706 (E706) "A

Study of Direct Photons." This was the shakedown run of the E706 spectrometer

and the Meson West (MW) beamline at FNAL. While the subject of this thesis

is the production of η mesons, the design and operation of E706 were driven by

the desire to study direct photons. The following paragraphs will discuss the

physics motivation of E706 – direct photons.

1.1 EXPERIMENTAL MOTIVATION

The present understanding of elementary particle physics is that hadrons

(*e.g.* protons, neutrons, pions, ...) are composed of pointlike particles called

quarks and gluons. These particles interact with each other via the strong force

by exchanging a gluon; gluons are the gauge boson for the strong color force as

described by Quantum ChromoDynamics (QCD). Quarks and gluons are also

referred to collectively as *partons*.[★] Testing QCD therefore involves the study of

parton interactions which can be represented by Feynman diagrams. Figure 1

shows two such diagrams. Figure 1(a) depicts a reaction where a quark and

antiquark annihilate to radiate two gluons. Figure 1(b) shows a quark–gluon

scattering interaction with the emission of a quark and a photon. This last

diagram shows what is known as a *direct* photon process in that the photon is

---

★ Isolated quarks have never been observed. It is postulated that quarks (and gluons) carry
a *color* charge and that only color neutral states are allowed for free particles. "Color" is
the strong interaction equivalent of electromagnetic charge and comes in six varieties: red,
blue, and green and their anti-colors. Quarks are thought to carry one of the colors and
gluons a combination of a color and anti-color. A color neutral particle is "white" in the
sense of additive color mixing.
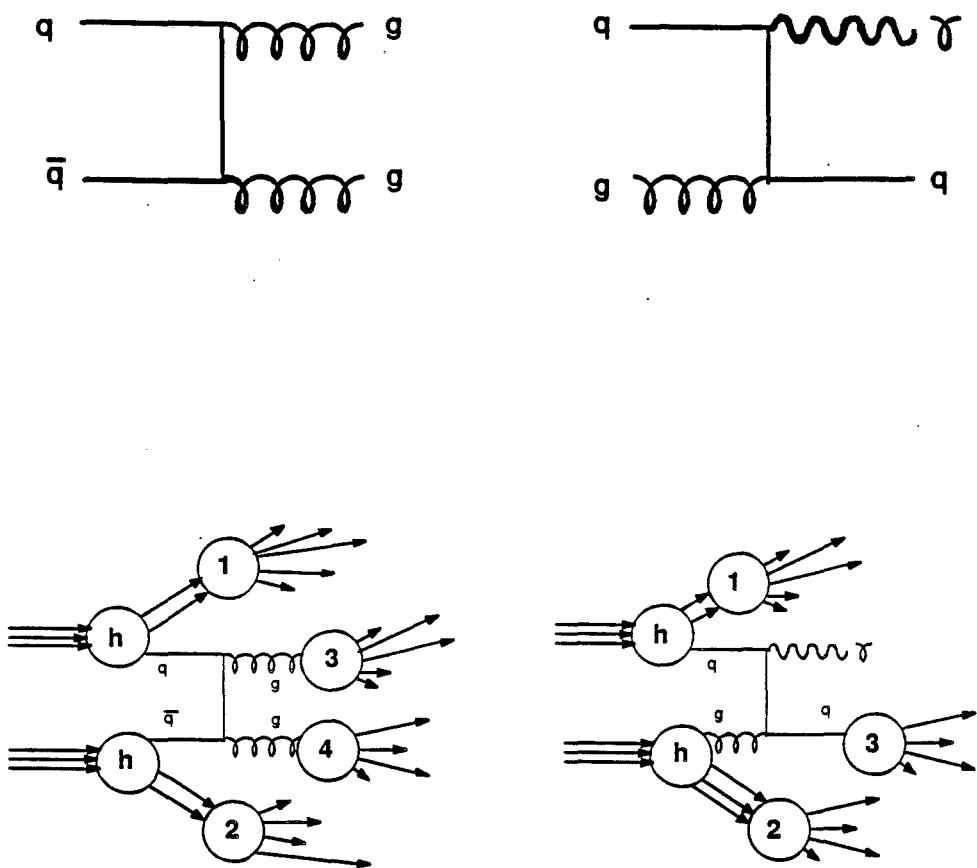
Figure 1   Feynman Diagrams With and Without Hadronic Structure

produced directly at the parton–parton scattering vertex. The primary focus of E706 is to study the production of such direct photons.

In studying QCD processes, one wants to extract information about the interaction between partons from the particles observed in the lab. Such a study is complicated by the fact that hadrons in the beam and target are composite objects consisting of several quarks and gluons and that scattered partons undergo a process called *fragmentation* before becoming directly observable. Fragmentation refers to the process by which the partons evolve into hadrons.[1] This situation is depicted in Figures 1(c) and 1(d). The two hadrons, labelled h entering the reaction are composite particles consisting of, in this case, three quarks each. The two scattering interactions are the same as in Figure 1(a) and 1(b) but here their relation to observable particles is shown explicitly. If each hadron supplies a quark to the scattering interaction, the resulting two quark system is unstable and fragments into hadrons (denoted by circles 1 and 2). The gluons emitted also fragment into hadrons (denoted by circles 3 and 4). Since what is measured in the laboratory is information about the reacting hadrons and the fragmentation products, extracting information about the hard scattering process of the partons is difficult.

At this point, one of the main advantages of using direct photon processes to study parton – parton interactions becomes apparent. Interactions like the one in Figure 1(d) have the advantage that the final state photon does not undergo fragmentation; it can be detected directly. This simplifies both the analysis of the physics process and the search for an experimental signature.

Another advantage is the fact that, to first order, there are only two processes

Compton Diagrams
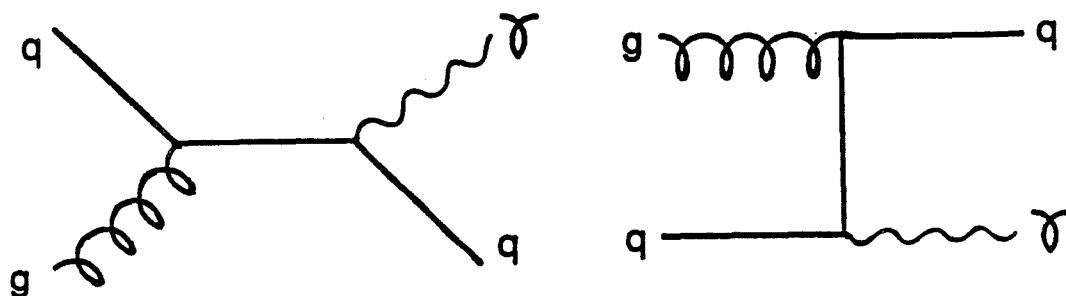
Annihilation Diagrams
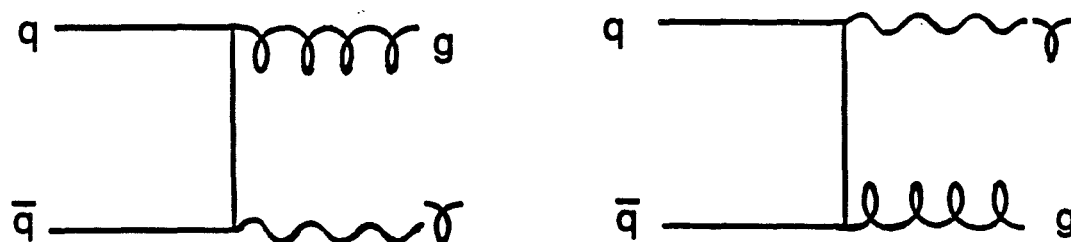
Figure 2   Feynman Diagrams of Leading Direct Photon Processes

(18 diagrams for 3 quark species) that contribute to the production of direct photons. These diagrams are shown in Figure 2. Figure 2(a) portrays the QCD *Compton* process, an interaction in which a gluon replaces the photon in the conventional QED Compton process. Figure 2(b) represents the *annihilation* process named for the annihilation of the quark and anti-quark. In contrast to Figure 2, there are 127 diagrams (for 3 quark species) that contribute to $jet-jet^*$ production.[2] Extracting information about particular subsets of those diagrams can be very difficult.

1.2 CROSS SECTION CALCULATIONS

Cross sections for QCD processes are not presently exactly calculable but are approximated by expansions in the coupling constant. The coupling constant for strong interactions is, to leading log,[2]

$$\alpha_s(Q^2) = \frac{4\pi}{(11 - \frac{2}{3}n_f)log(Q^2/\Lambda^2)} \qquad (1.1)$$

where Q^2 is a measure of the momentum transfer in the collision, Λ is a scale parameter required by the expansion, and n_f is the number of quark flavors available at the energy of the collision. Equation (1.1) shows that as Q^2 increases $\alpha_s(Q^2)$ decreases. This fact leads to increasing confidence in perturbative expansion calculations for high momentum transfer reactions and is the motivation for studying high p_T production.

★ The fragmentation products of partons form a spray of particles which at higher energies are collimated into a *jet.*

The invariant inclusive cross section for direct photon production, $A + B \rightarrow \gamma + X$, can be written in terms of leading order in α_s as follows:

$$E\frac{d^3\sigma}{dp^3} = \sum_{ab} \int dx_a dx_b G_{a/A}(x_a, Q^2)G_{b/B}(x_b, Q^2) \times$$
$$\frac{\hat{s}}{\pi}\frac{d\sigma}{d\hat{t}}(ab \rightarrow \gamma d)\delta(\hat{s} + \hat{t} + \hat{u}) \qquad (1.2)$$

where $\hat{s}$, $\hat{t}$ and $\hat{u}$ are the Mandelstam variables for the pointlike scattering, given by $\hat{s} = (p_a + p_b)^2$, $\hat{t} = (p_a - p_\gamma)^2$, and $\hat{u} = (p_a - p_d)^2$; p representing the four momenta of the parton or photon. $G_{i/I}$ is the number distribution for parton i in hadron I, with a momentum fraction between x and $x + dx$. $G = \frac{1}{x}F$, where F is the hadronic structure function.

Equation (1.2) shows that the hadron cross section is related to the parton distribution functions, convoluted with the parton-parton point-like cross sections. For the processes shown in Figure 2, these elementary cross sections are[3]

$$\frac{d\sigma}{d\hat{t}}(qg \rightarrow q\gamma) = -\frac{\pi\alpha\alpha_s}{2\hat{s}^2}e_q^2\frac{\hat{u}^2 + \hat{s}^2}{\hat{s}\hat{u}} \qquad (1.3)$$

$$\frac{d\sigma}{d\hat{t}}(\bar{q}q \rightarrow g\gamma) = \frac{8\pi\alpha\alpha_s}{9\hat{s}^2}e_q^2\frac{\hat{u}^2 + \hat{t}^2}{\hat{t}\hat{u}}. \qquad (1.4)$$

The cross section for inclusive hadron production, expressed to leading log, is given by[2]

$$E\frac{d^3\sigma}{dp^3} = \sum_{abcd} \int dx_a dx_b dz_c G_{a/A}(x_a, Q^2)G_{b/B}(x_b, Q^2)D_{C/c}(z_c, Q^2) \times$$
$$\frac{\hat{s}}{z_c^2\pi}\frac{d\sigma}{d\hat{t}}(ab \rightarrow cd)\delta(\hat{s} + \hat{t} + \hat{u}) \qquad (1.5)$$

where $D_{C/c}$ is the fragmentation function, giving the probability density of find-

ing hadron C with a momentum fraction between z and $z + dz$ from the frag-

mentation of parton c.

1.3 MOTIVATION FOR THE STUDY OF NEUTRAL MESONS

While the study of direct photons yields information about the intrinsic

QCD processes at large momentum transfer, high p_T meson production yields

information on the fragmentation function, $D_{C/c}$, for partons. One can see from

equation (1.6) that the production of a meson at a given p_T can only come from

a quark or parton jet of higher p_T (note $z \leq 1$). Since the cross section is a

steeply falling function of p_T , at any given p_T one tends to be looking at a

fragmentation where most of the parton momentum is taken by that leading

particle.

By looking at the ratio of production of π°/η one can study the relative

importance of gluons and valence and sea quarks in the production of high p_T

neutral mesons. The η and π° quark structure[4] can be written, approximately,

as:[★]

$$\eta = \frac{1}{\sqrt{6}}(u\bar{u} + d\bar{d} - 2s\bar{s}), \qquad (1.7)$$

$$\pi^\circ = \frac{1}{\sqrt{2}}(u\bar{u} + d\bar{d}). \qquad (1.8)$$

where u, d, and s refer to up, down and strange quarks respectively. Since the

η has a strange quark component and there are no strange valence quarks in

pions, protons, or neutrons (the target and beam hadrons), dominance of valence

---

★ The η is more precisely a linear combination of the SU(3) octet and singlet $I = 0$ states:
$\eta = \eta_0 sin\theta_{08} + \eta_8 cos\theta_{08}$, where the mixing angle $\theta_{08} \approx 11°$, η_8 is used above, and $\eta_0 = \frac{1}{\sqrt{3}}(u\bar{u} + d\bar{d} + s\bar{s})$.

quark fragmentation in neutral meson production would predict suppressed η production relative to π° .

The other two possibilities for the source of the fragmenting parton are quarks from pair creation by a gluon (*sea* quarks) or gluons themselves. Although there are slight differences between the mass of the up, down and strange quarks, one expects in this energy range that the population of u, d, and s sea quarks is the same. Similarly one expects no preference for gluon fragmentation into one of these species over another. The ratio of η/π° production is given by the ratio of the squares of equation (1.7) to equation (1.8). For the extreme case of no sea quark or gluon contribution one predicts a ratio of 0.33; for the opposite extreme of no valence quark contribution one expects a ratio of unity. Therefore the actual value should lie in the range between $0.33 - 1.0$, depending on relative importance of various parton fragmentation functions. Since the structure function of the interacting hadrons are functions of momentum fraction, x, one might also expect a dependence on p_T for a given beam energy since greater p_T implies greater x of the scattering parton. The results of this thesis will be compared to these expectations in a later chapter.

From the point of view of the direct photon study goals of the experiment, neutral mesons where, for some reason, one of the decay photons was lost represent a significant background. To correct for this background the production of these neutral mesons needs to be well understood.

1.4 PREVIOUS EXPERIMENTS

Over the past decade, several experiments have studied the production of
η mesons at high p_T. This section will briefly describe some of these experiments. Their previous measurements are used in the final chapter of this thesis
to compare with the results of our analysis.

ISR   The study of direct photons was started at the ISR (Intersecting Storage
Ring) at CERN (European Organization for Nuclear Research). Three groups
that published data on production of η mesons were AFS, CCRS, and R806.

The AFS (Axial Field Spectrometer) collaboration[5] studied the production
of direct photons, π° and η mesons at $\sqrt{s} = 53\,\text{GeV}$. Their data cover the range
of transverse momentum $2 \leq p_T \leq 6\,\text{GeV/c}$, for the rapidity range $\mid y \mid \leq 0.4$.
Their apparatus consisted of a central drift chamber with walls of sodium iodide
detectors covering $1.2\,\text{sr}$ or solid angle. The NaI crystals were 5.3 radiation
lengths thick. Surrounding this was a uranium – scintillator calorimeter with a
six radiation length electromagnetic section and a 3.6 absorption length hadronic
section.

The CCRS (CERN Columbia Rockefeller Saclay) collaboration[6] measured
the production of π° and η mesons at 90° for $\sqrt{s}$ between 23.5 and 62.4 GeV
using two spectrometers facing the interaction region. Each arm of the apparatus
covered 0.59 steradian in the lab. One arm used a shower spark chamber, backed
with a set of five lead/scintillator sandwich counters for electromagnetic shower
detection. The other arm used lead glass detectors. The first had a depth of
15.5 radiation lengths and the second 14.8.

R806[7] measured the production of π° and η mesons at $\sqrt{s}$ of 52.7 and 62.4 GeV in the central rapidity region. Their results show data for the range $3 \le p_T \le 8$ GeV/c and were obtained using liquid argon calorimeters.

FNAL Two experiments at Fermilab which have published measurements of high p_T production of η mesons are E111 and E629.

E111[8] was run in the M2 beamline using a hydrogen target and a variety of beam particles and momenta. They presented results for $\pi^\pm$, K, and p beams at 100, 200 and 300 GeV/c incident momenta. The range of transverse momenta covered was $1.5 \le p_T \le 4.0$ GeV/c. Their detector consisted of 19 radiation lengths of lead interleaved with narrow scintillator rods. The detector was positioned to cover the center of mass angles between 50° and 110° and centered on 30° and 60° for portions of their data taking.

E629[9] studied the production of π° and η mesons on beryllium, carbon, and aluminum targets. They used a liquid argon calorimeter for detection of electromagnetic showers covering the region around 90° in the center of mass. Results were presented for 200 GeV/c π^+ and p beams with rapidity range $-0.5 \le y \le 0.1$. Data span the transverse momentum range of $2.0 \le p_T \le 5.0$ GeV/c.

Recent CERN Within the past few years several CERN experiments have published results on neutral meson production. Typical of these are WA70 and UA6.

WA70[10] used π^-, π^+, and p beams at 280 GeV/c on a hydrogen target to study the production of π° and η mesons, and direct photons, in the rapidity in-

terval $|y| < 1$ and the p_T range $3 - 7\,\text{GeV/c}$. They used a lead, liquid-scintillator detector of 24 radiation length in depth for photon detection, and the Omega spectrometer for charged particle tracking.

UA6[11] used a hydrogen jet crossing the SPS ring as their target to study the production of π° and η mesons at $\sqrt{s} = 24.3\,\text{GeV}$. By rearranging their detector in the SPS tunnel on either side of the interaction region, they were able to study both pp and p$\overline{\text{p}}$ reactions. Their electromagnetic particle detection was performed using two lead proportional-tube detectors. Their data extended over the range $2.5 \leq p_T \leq 5.0\,\text{GeV/c}$.

As mentioned before, all above results will be presented later in this thesis.

2. Experimental Apparatus

During the 1987–8 running period, Experimental Hall MW9 was occupied by two experiments, E706 and E672 ("Hadronic States Produced in Association with High Mass Di-muons"), with E706 occupying the upstream section of the hall and E672 the downstream section, as shown in Figure 3. Although the two experiments coordinated their data acquisition system to use a common trigger, this thesis uses no information from the muon spectrometer and so does not include a description of its apparatus.

Due to the size of the tasks involved in constructing and operating all the equipment used by E706, responsibility for individual sections of the spectrometer was allocated to specific institutions within the collaboration. This chapter contains a brief description of the elements of the beamline and of the E706 spectrometer, along with an acknowledgement of the institution with primary responsibility for each element. The sections describing the liquid argon calorimetry are expanded since the author's institution had primary responsibility for that apparatus.

	Positive Particles			Negative Particles		
Particle	p	π^+	K^+	π^-	K^-	$\bar{p}$
Production	1×10^8	1×10^7	3×10^6	2×10^7	6×10^5	$\leq 6 \times 10^4$

Table 1   MW Secondary Beam for 1×10^{12} Primary Protons

Figure 3   Layout of Apparattus in MW9

GAS

PIT

LATCHES

LATCHES

AIL

E-706

1-Hadron Shield
2-Veto Wall
3-Target/SSD
4-Analysis Magnet
5-PWCs
6-EMLAC
7-HALAC
8-FCAL

LN2

LIQUID ARGON STORAGE

E-672

9-PWCs
10-Toroid
11-Muon
    Chambers

13
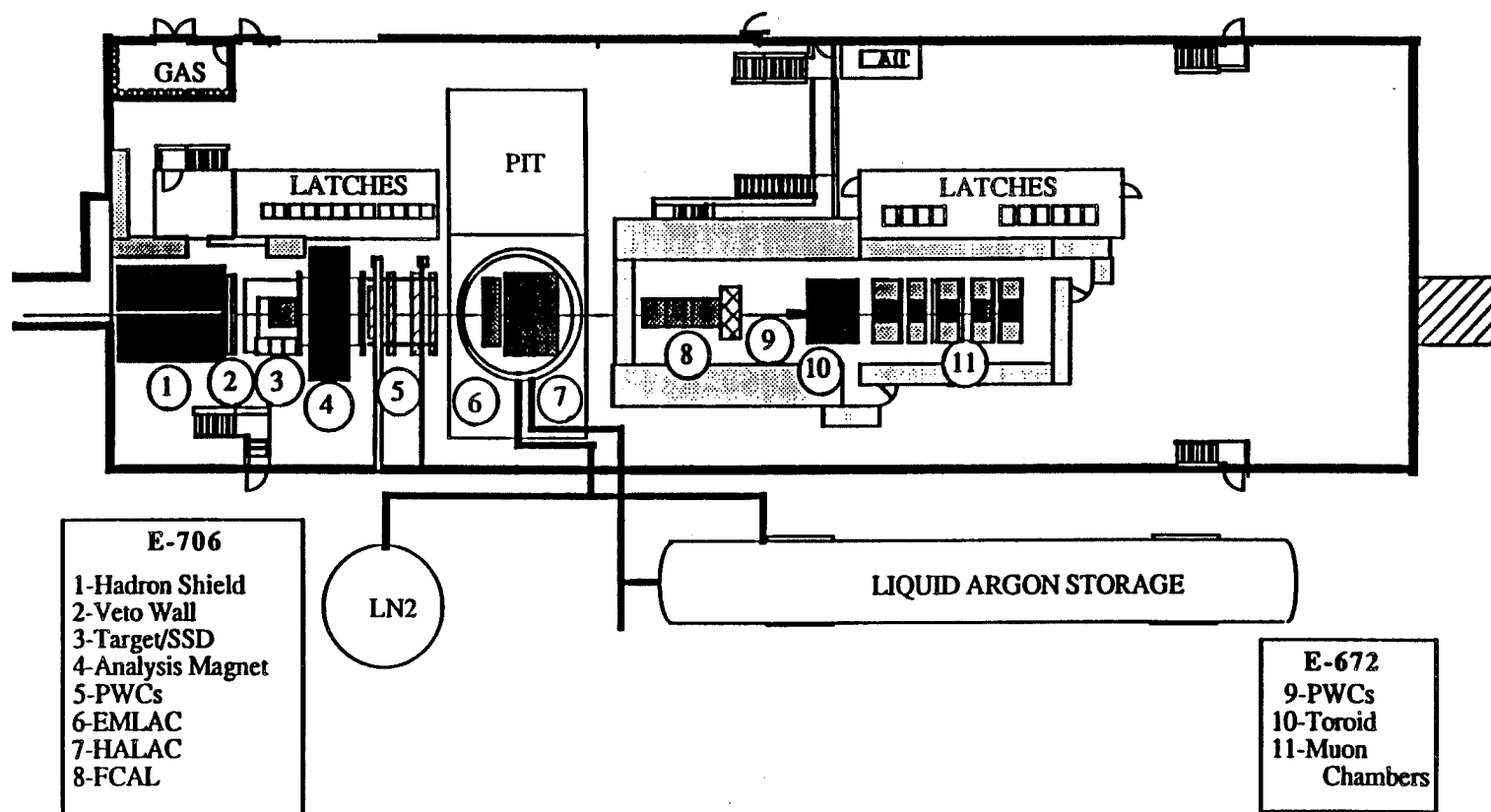
2.1 MW BEAMLINE

E706 is located in the new Meson West beamline at FNAL. This beamline extends from the old Meson Hall north to the MW9 experimental hall. The beamline was constructed, along with the MW9 experimental hall, for the MW spectrometer and can transport positive and negatively charged particles with a maximum momentum of 800 GeV/c.

To produce beam in the experimental areas, the Tevatron provided a beam of 800 GeV/c protons into the main "switchyard." Here the beam was split and directed into three main beamlines: Proton, Meson, and Neutrino. The Meson beamline had another switchyard to divide beam among the various experiments in the Meson area and route the particles into the Meson Hall. Inside the Meson Hall was E706's primary target: a $3/4$ interaction length aluminum block in which the secondary particles constituting the MW beam were produced. Beam intensity on the primary target was typically $2-3 \times 10^{12}$ protons per spill for a negative secondary beam and 1×10^{12} for a positive secondary beam. Table 1 shows the content of the secondary beam assuming 1×10^{12} 800 GeV/c primary protons and a secondary momentum of 530 GeV/c. The three most populous particles are listed for each polarity of the secondary beam. The greater population of π^- over π^+ reflects the production angle of 1.4 mr for positive beam. This angle was required for radiation safety considerations to prevent accidental transmission of primary beam. The negative beam was produced at 0 mr.[12]

The beam had a 19.9 ns *bucket* structure from the radio frequency (RF) acceleration within the Tevatron. The buckets were grouped into 23 second

spills. Spills were separated by a 37 second accelerator recharge period during which time no beam was delivered to the experimental areas.

The secondary particles from the primary target were transported into the momentum selecting region of the MW beamline . There, five *spoiler* magnets, labelled MW7S-[1–5] in Figure 4, bent out charged particles travelling parallel to the beam. As mentioned in Section 1.4, stray muons paralleling the beam are a principal part of the background to direct photon physics. Muon contamination of the beam was measured by counting beam particles with the beam collimators closed. This meant that the hadron beam had to traverse 3 m of steel and effectively left only the muons produced with the beam. The contamination was found to be 0.4% for positive beam and 0.5% for negative beam.[13]

The beamline parameters were tuned for a 530 GeV/c secondary beam. A choice substantially less than the primary momentum of 800 GeV/c achieved a reasonable intensity of negative secondary beam without demanding an overly large fraction of the protons in the accelerator. This specific choice was also significant in that the average momentum of valence quarks is the same in mesons of 530 GeV/c and protons of 800 GeV/c momentum. This would allow for greater ease in comparison of data from the pion and primary proton data. For radiation safety reasons, during the 1987–8 fixed target run, primary protons could not be transmitted into the experimental hall.

<u>Cherenkov Detector.</u> Separated from the primary target region by a series of focusing magnets was a long parallel section for the beam. This was a region where the angular divergence of the beam particles was minimized. Such a section makes possible the use of a Cherenkov detector in the beamline.
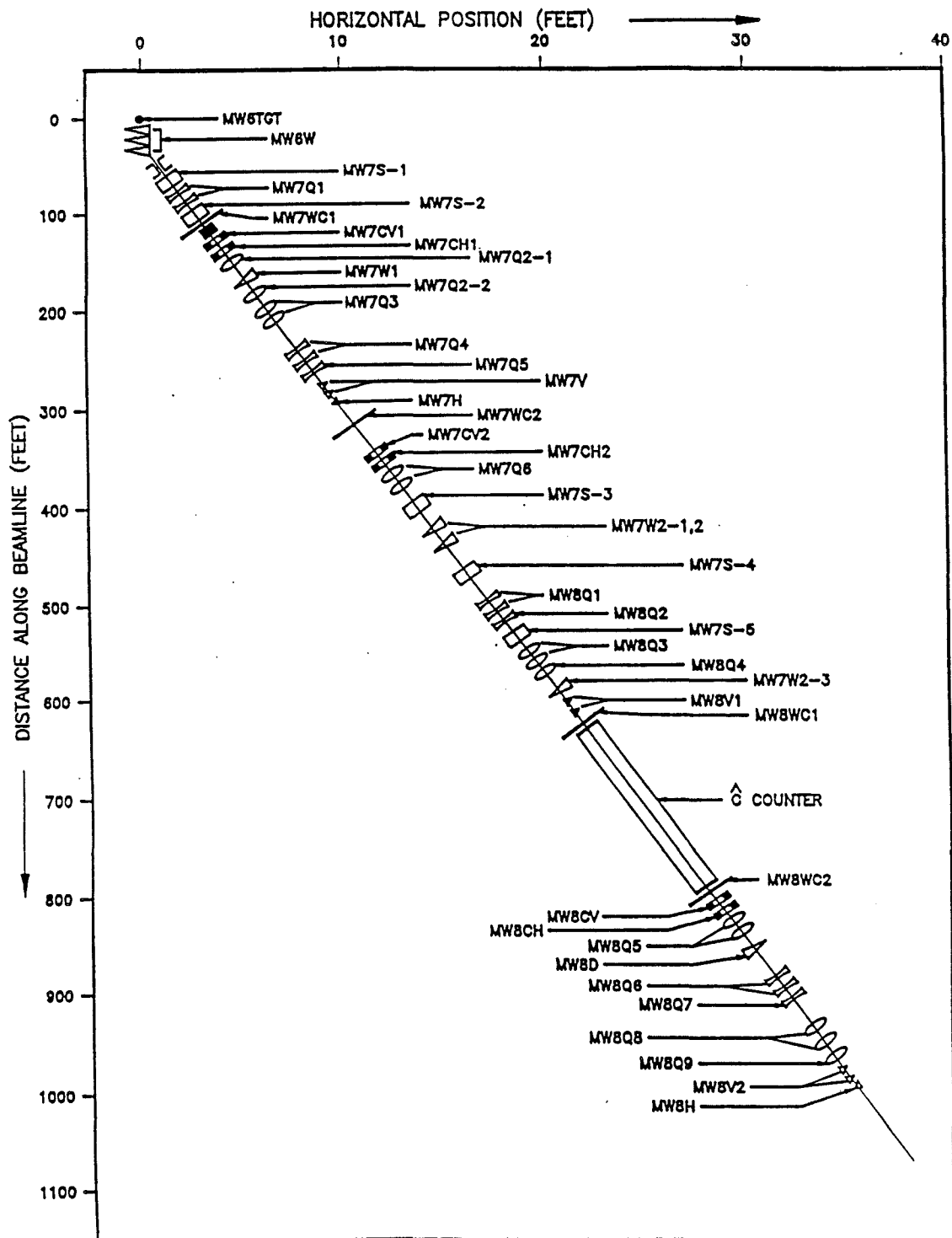
Figure 4   MW Beamline Layout

Cherenkov Detector
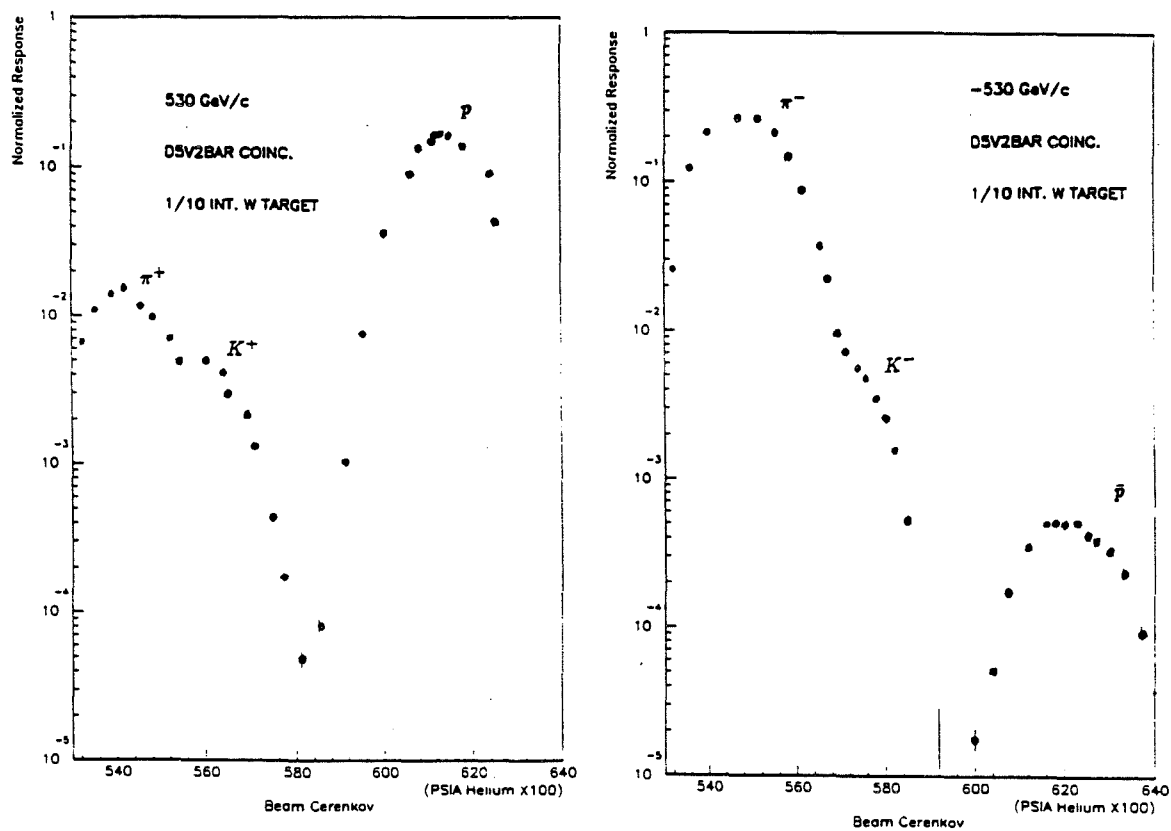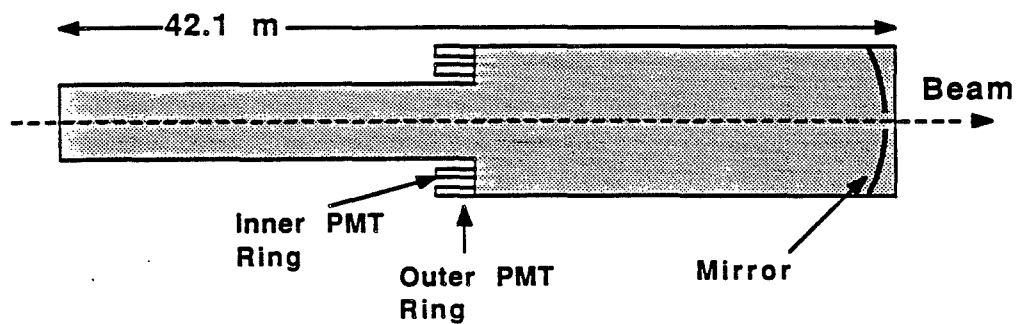
Figure 5   Cherenkov Detector Construction and Pressure Curves

E706's Fermilab collaborators supplied a differential Cherenkov counter to discriminate and tag minority particles in the secondary beam. Figure 5 shows the ability of the Cherenkov detector to distinguish particle types in the two beam polarities. By changing the pressure of the radiator gas one could select the velocity of the particle tagged. Since the momentum was fixed by the beamline optics, this was equivalent to selecting a mass. The Cherenkov detector was set to tag K^- in a negative beam and π^+ in a positive beam. As shown in Table 1, these particles were the second most populous variety for their respective beam polarities.

The detector, as shown in Figure 5, was 42.1 m long and had a radius of 24.4 cm. It used helium gas, at pressures of $4 - 7$ psia, as its radiator and had a Θ_c of 5 mr. It had one coincidence and one anticoincidence ring of phototubes, consisting of six phototubes each, to detect the radiated photons.[13]

Calibration Magnet   The MW beamline contained a dipole magnet to deflect the beam vertically. This magnet was used during the calibration of the spectrometer and was normally off during data acquisition.[14] The final quadrupole section which was downstream of the calibration magnet could be swung out of the way during calibration. The calibration dipole was 3 m long with an aperture of 7.6×15.2 m. It was 13.7 m upstream of the secondary target and is marked MW8D on Figure 4.

Hadron Shield and Beam Counters   At the end of the beamline was a hadron shield, 4.3 m wide, 4.7 m long, and 3.7 m high, made from scrap battleship armor plate. The purpose of this mound of iron was to absorb the associated beam *halo* (particles traveling parallel with the beam). The shield had a 30.5 cm
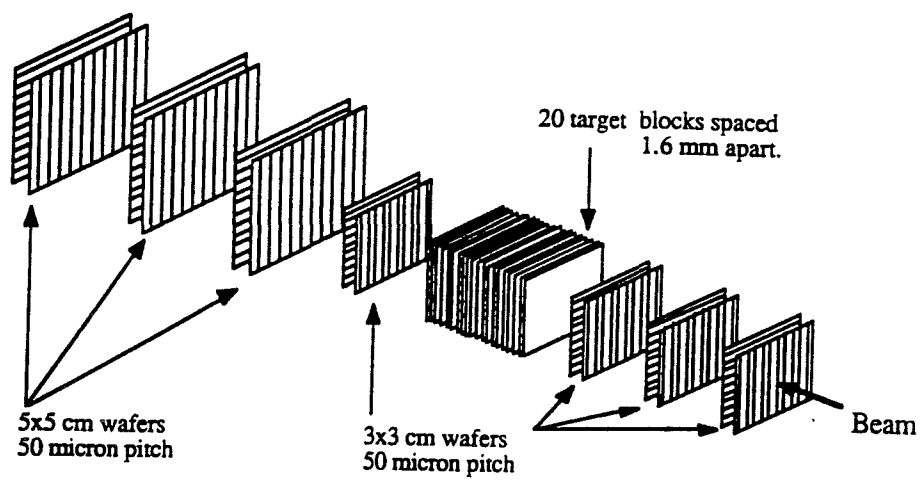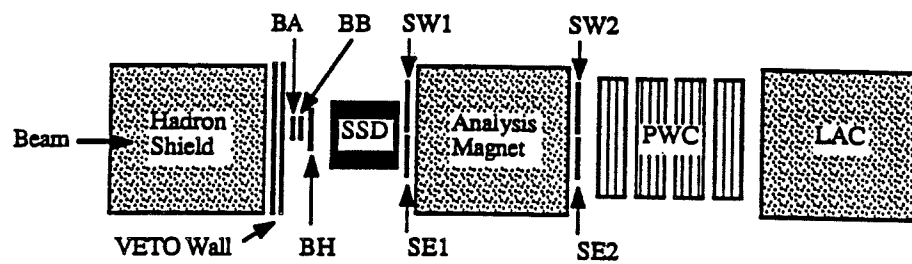
Figure 6   Layout of Target Region

wide vertical slot along the beamline filled by three iron slabs. These slabs were removable allowing the beam to be scanned in the vertical direction during calibration. The evacuated beam pipe extended through the slot in the hadron shield and terminated in a 76 micron titanium window.

There were several counters used in the experiment to note the passage of a charged particle (e.g. a beam particle). These were made of acrylic scintillator with phototubes attached. The outputs from these counters were sent to discriminator modules in the forward latch house marked in Figure 3. Figure 6 shows the counters positions and the next few paragraphs describe their function.

On the downstream end of the hadron shield were two *veto walls* of counters as shown in Figure 6. These walls were made of four 213×160 cm modules arranged to have a 10×10 cm hole centered on the beamline. These veto walls were used to tag events containing charged particles which traversed the hadron shield. These particles were typically muons that were not swept clear of the region by the upstream spoiler magnets.

The two walls had cracks between the four modules, shown in Figure 7, staggered to minimize leakage of muons through both walls. Each module contained eight scintillator counters. The experiment was disabled when there were signals in the same quadrant of both walls. This technique was a powerful tool to suppress background triggers due to halo particles.

The beam was defined by three scintillator counters shown in Figure 6. Two of them, BA and BB, were 2.5×2.5 cm and 0.15 cm thick. The third, BH, was 12.7×12.7 cm and 0.7 cm thick with a 1 cm hole in its center. Counters SE1
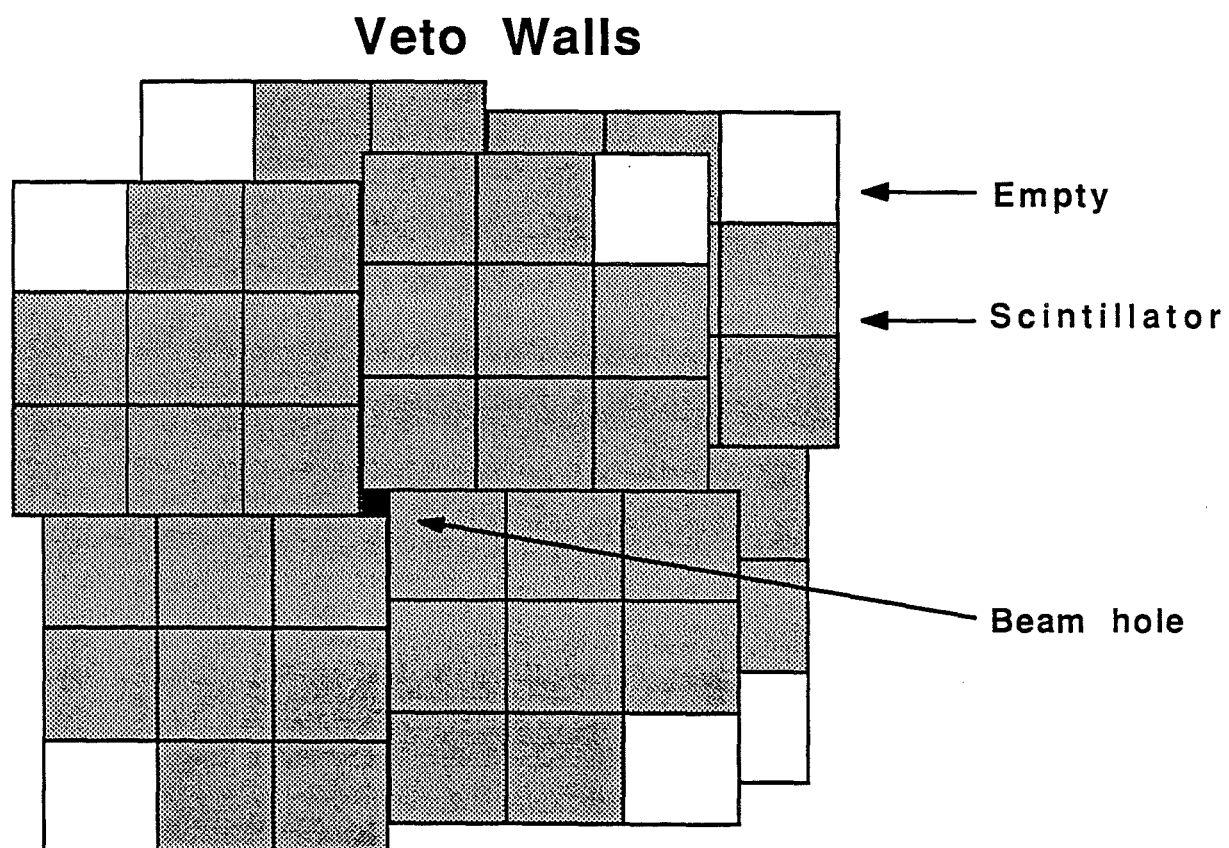
Veto Walls

Figure 7   Arrangement of Veto Wall Modules

and SW1 mated to form a 10 cm square counter with a 2 cm hole centered on the beam axis. These covered the angles 27 to 142 mr. SE2 and SW2 mated to form a pair of counters 20 cm square with a 3.8 cm hole in the center, covering the angles 4.5 − 24 mr.

2.2 TRACKING SYSTEM

The tracking system consisted of Silicon Strip Detectors (SSDs), provided by the University of Pittsburgh, for upstream tracking, an analyzing dipole magnet, and a set of Proportional Wire Chambers (PWCs), provided by Michigan State University and Penn State University, for downstream tracking.

<u>Silicon Strip Detectors</u> The design of the upstream tracking system had several experimental constraints. It had to be compact along the beam axis so that the analysis magnet would not shadow the LAC from wide angle secondaries produced in the target. At the same time, the angular resolution had to be such that ambiguities in the track reconstruction of the PWCs could be resolved and secondary interactions located.[15,16]

Figure 6 shows the target region layout, including the SSD system. The target for E706, originally, was a set of 20 plates spaced 1.6 mm apart. Each plate was 10×10 cm in area and $\frac{1}{200}$ of an interaction length thick. Data was taken using beryllium (Be) and carbon (C) targets, but most of the data used in this analysis was taken with the 20 plate Be target with two copper (Cu) 0.8 mm foils mounted 3.2 mm upstream. The two Cu foils were separated by 1.6 mm. Upstream of the target there were six silicon wafers, three with strips aligned vertically and three horizontally. Downstream of the target four more pairs of

wafers brought the total to 14. The three pairs upstream of the target and the first pair after the target were 3×3 cm. The three sets furthest downstream were 5×5 cm. All of the wafers had a thickness of 200μm and a 50μm pitch between strips.

There were a total of ≈ 8800 channels for the SSD system, of which ≈ 6600 were instrumented. The uninstrumented channels corresponded to the periphery of the upstream wafers and, in the downstream wafers, to strips outside the angular coverage of the last downstream wafer. The wafers were mounted to a series of three "fanout" boards. These boards dispersed the traces connected to the silicon strips so that there was physically room to mount the preamplifier for each channel.

Analysis Magnet   The momentum analyzing magnet used in this experiment was a dipole with a maximum field of 15.2 kG, centered 2 m downstream of the target. The magnet was set to deliver a 450 MeV/c kick to charged particles passing through its aperture. The magnet aperture expanded from 35.6×25.4 cm at the upstream face to 137.2×124.5 cm at the downstream face – a distance along the beamline of 390 cm. It had two mirror plates, one upstream and one downstream, to reduce the fringe field outside the volume of the magnet. This reduced the interference of the magnet on the performance of the phototubes for the interaction counters as well as simplified the job of track reconstruction.

Multi–Wire Proportional Chambers   There were 16 planes of multi-wire proportional chambers with a rate capability in excess of 1 MHz. The 16 planes were distributed in four modules. Each of these modules contained four planes with wires in the X, Y, U($+37°$), and V($-53°$) orientation. The sense wires of

each plane had a pitch of 0.25 cm. The cathodes were constructed of graphite coated mylar. The graphite coating was segmented into pads so that regions near the beam could be selectively adjusted to lower voltages. This prevented the channels nearest the beam from being overloaded by too many hits.[17]

The electronics for both the SSDs and the PWCs was identical, with the exception of the addition of preamplifiers used with the SSDs. The signals from the detectors were processed using a readout system from Nunamaker Electronics, Inc. All of these modules were housed in CAMAC crates.* These crates were then read out on a serial CAMAC highway by a PDP 11/34.

Chamber	Aperture	
	(m × m)	(mr × mr)
1	1.22 × 1.63	174 × 229
2	2.03 × 2.03	220 × 220
3	2.03 × 2.03	178 × 178
4	2.44 × 2.44	180 × 180

Table 2   PWC Apertures

2.3 CALORIMETRY

The E706 spectrometer contained three specialized calorimeters. The ElectroMagnetic Liquid Argon Calorimeter (EMLAC) and the HAdronic Liquid Argon Calorimeter (HALAC), collectively referred to as the "LAC", were sam-

---

* CAMAC is an acronym for Computer Automated Measurement And Control. It is an industry standard computer bus and hardware specification widely used in high energy physics. See Ref. 18 for a collection of papers describing the system.

pling calorimeters[†] with liquid argon as the active medium and lead and steel, respectively, for their absorbers. The forward calorimeter was a steel and plastic scintillator sampling calorimeter.

The LAC subtended a large portion of the center of mass solid angle of an event and was constructed to be roughly symmetric in rapidity[‡] covering ± 1 unit centered at 0. The forward calorimeter was used to measure the energy in a forward cone missed by the LAC. A general discussion of the use of calorimetry in high energy physics can be found in Fabjan[19] (1985). Descriptions of the E706 LAC have been published in Gutierrez[20] (1986) and Lobkowicz[21] (1985) and a detailed discussion is available in Ref. 14.

LAC Physical Setup   Both the EMLAC and the HALAC were hung from a mobile support structure – the gantry – shown in Figure 8. The gantry was a steel I–beam frame which contained the cap for the cryostat enclosing the calorimeters. Attached to the cap of the cryostat was the cryogenic piping used to supply the liquid nitrogen to the cooling coils. These coils were hung from the cap, just above the calorimeters, to recondense argon that boiled off from the pool containing the calorimeters. To reduce heat loss and prevent the cold vapors

---

† The term "sampling calorimeter" denotes calorimeters where most of the energy lost by the incident particles is not detected. It is lost in the "absorber" material. The detector is made of interleaved layers of absorber material and active medium. The shower energy is then sampled in the active material layers. The energy lost per unit length is typically much lower and the cost much higher for the active medium than the absorbing medium. This makes sampling calorimeters economically attractive solutions, although their resolution is degraded with respect to total absorption calorimeters.

‡ Rapidity, y, is defined as

$$y = \frac{1}{2} ln(\frac{E + p_{||}}{E - p_{||}})$$

where E is lab energy and p is momentum parallel to beam axis.
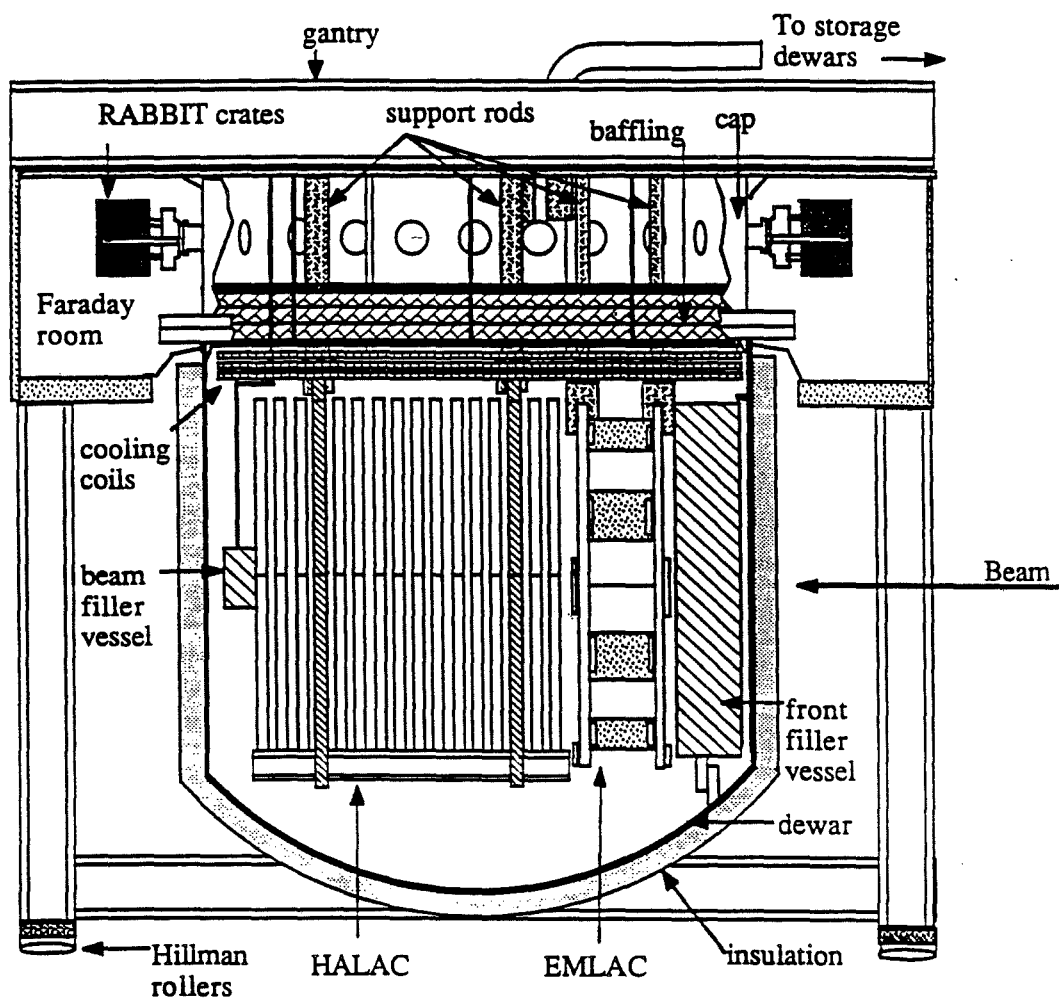
Figure 8   Support Structure for the Liquid Argon Calorimeters

from embrittling the carbon steel cap, an insulating layer of plastic baffling was placed above the cooling coils.

The cap also featured 30 access ports distributed around its circumference to allow connections to the calorimeters for the signal cables as well as high voltage cables. Since a LAC has no inherent charge gain, the signals were very low level. The LAC amplifiers are thus very sensitive to electromagnetic interference.

To reduce interference the top of the gantry, as shown in Figure 8, was constructed as a Faraday room. The walls of the room were lined with galvanized sheet metal, with electrical contact to the gantry made along the circumference of the cap. All power for the Faraday room was filtered using isolation transformers. All signal cables were isolated at the Faraday room wall using optical couplers built by the University of Rochester or using transformers. All electrical penetrations as well as doors were restricted to a section of downstream wall of the Faraday room. With all these precautions, the limiting noise signal in the LAC electronics was traced to a 4 kHz commutation spike from the rectifying diodes used in the 400 Hz power supplies inside the Faraday room.

The gantry moved transverse to the beam on a set of Hillman rollers powered by a pair of power screws embedded in the floor. This feature was necessary for the assembly of the cryostat because the detectors, being suspended from the gantry, could not be lowered into the dewar. Instead, a pit large of enough to contain the dewar was built into the building's foundation next to the beamline. The gantry moved over the pit and, once there, the dewar was raised around the calorimeters by a set of four power screws attached to the top of the gantry. Once the cryostat was assembled and in position, the horizontal motion of the

gantry in combination with vertical deflection of the beam from the calibration magnet allowed the entire face of the detectors to be swept by the beam. This meant that all of the detector channels could, at least in principle, be calibrated by beam.

The dewar which enclosed the calorimeters was made of 1.6 cm rolled stainless steel plate and was 5.2 m in diameter. Insulation was provided, as shown in Figure 8, by a covering of cryogenic insulation for two reasons. First, in order to satisfy safety requirements for an outer pressure vessel, the wall of a vacuum jacket would need to be nearly as thick as the dewar wall, putting a large amount of material between the detectors and the target. Secondly, a vacuum jacket was prohibitively expensive to implement.

The dewar wall had a 5.1 cm diameter port made of 3.2 mm for the beam. This reduced the amount of material in the path of the beam, and consequently beam scattering, particularly in the forward calorimeter. To further reduce unwanted interactions, there were two low density volumes used to displace liquid argon inside the dewar. One was a truncated cylindrical section mounted in front of the EMLAC referred to as the *front filler vessel*. The other was a tapered cylindrical volume inserted into the beam holes of both calorimeters known as the *beam filler vessel*. Both of these vessels are marked in Figure 8.

The front filler vessel was constructed of a cryogenic closed cell foam covered with a layer of epoxy/fiberglass and enclosed in a $1/16$ in stainless steel skin. Besides limiting the number of beam interactions in the cryostat, the front filler vessel helped reduce energy smearing of incoming particles due to interaction with material between the target and the calorimeters.

The beam filler vessel was a hollow conical shell made of 1.6 mm stainless steel sheet. Since the vessel was hollow and of thin steel construction, it required pressurization when immersed in liquid argon to prevent hydrostatic pressure from crushing it. To minimize material, helium was used as the pressurizing gas.

Electromagnetic Calorimeter The most upstream of the calorimeters was the electromagnetic calorimeter (EMLAC). This sampling calorimeter was built of 66 cells with 22 cells in the "front" section and 44 in the "back." A cell consisted of an anode board, a lead sheet, an anode board, and the two liquid argon gaps between them.[*] The calorimeter had a cylindrical geometry with a radius of 1.5 m and depth of 71 cm. There was a hole in the center of the cylinder, of radius 20 cm, through which the beam and very forward particles should pass. This hole allowed the detector to be used in the high rate environment expected for E706.

The calorimeter was composed of structurally independent quadrants to allow the detector to be assembled in modules. Each quadrant was conceptually identical, with minor structural differences due to differences in mechanical stresses when assembled. Figure 9 shows a cut–away view of one of these quadrants. As shown, the lead absorber plates were interleaved with copper clad G–10[†] anode plates. The anode planes were attached to the instrumentation amplifiers. The lead plates were maintained at negative high voltage, with respect to the anode plates, to provide the electric field for the calorimeter cell. Charged particles (from electron or photon showers or other charged particles)

---

[*] This longitudinal separation had several functions as will be described later.

[†] G–10 is the industrial designation of a glass epoxy material similar to the one used for printed circuit boards. It however, does not have the usual fire retardant additives. We found these additives contaminated the liquid argon.

Vertical Tapered
Plate Sections

Phi-Board

Lead Plate

R-Board

Spacers

Front plate

Capacitor Bank

Slotted Spring
plate

Support Ring
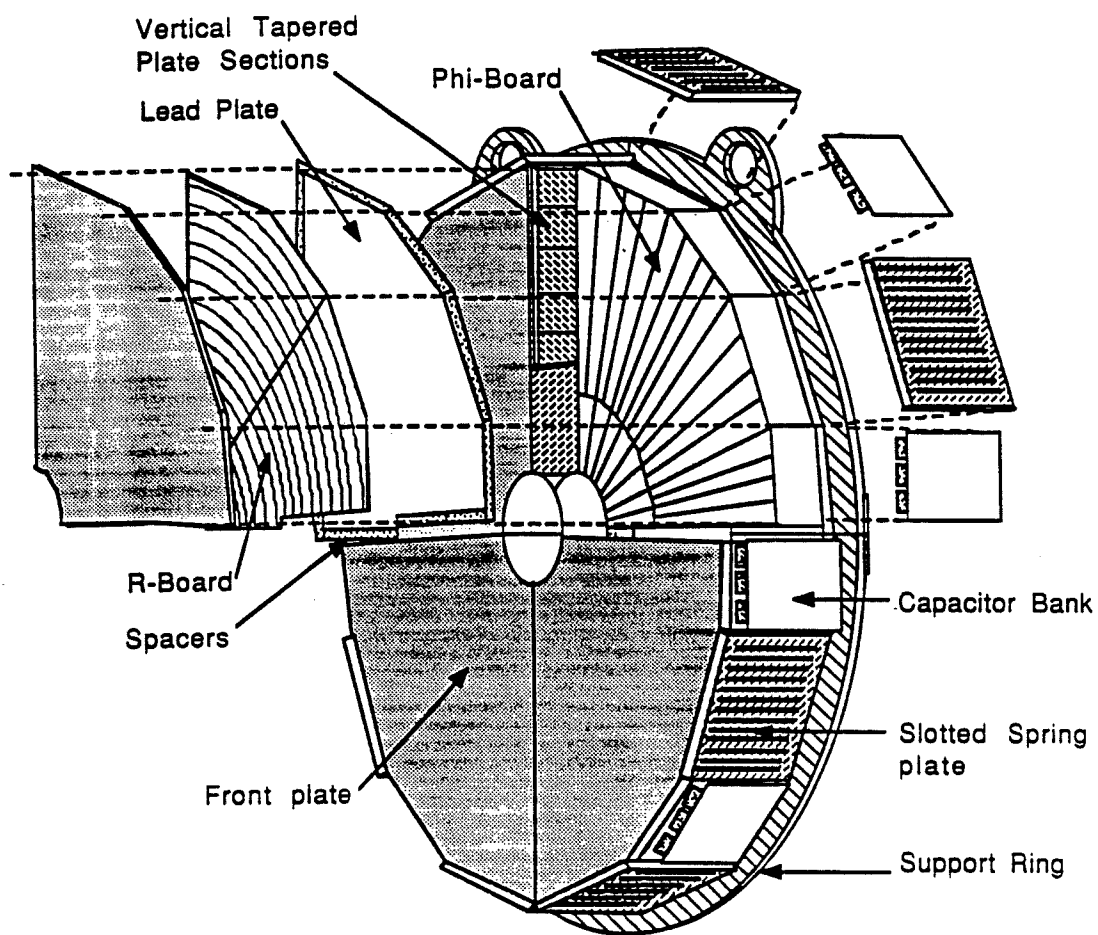
Figure 9   EMLAC Quadrant Construction

passing through the calorimeter ionized the argon atoms. The electric field caused the electrons to drift onto the anode strips (and the much slower argon ions to the cathode).

Because of the fine granularity required to resolve the two photons from an energetic π°, the EMLAC was built using *strip* readout rather than *pad* readout to reduce the electronics requirements in the readout. A strip readout system has two separate readout views with the detector element in each view finely segmented in one dimension and rather coarse in the other. This can be seen in Figure 9. A pad system has elements that are segmented in both dimension and is exemplified by the hadronic calorimeter discussed later. As the spatial resolution becomes more fine, the number of pads grows as n^2 but the number of strips grows as $2n$.

For the cylindrical geometry of the EMLAC an R/ϕ readout system was natural. This also simplified the p_T trigger that will be discussed in the following chapter. Figure 9 shows that the two different types of readout boards were interleaved. The stacking order of the EMLAC layers was: absorber, R anode, absorber, ϕ anode, absorber ...

The anode boards were machined, on both sides, on a computer controlled milling table built at the University of Rochester. The boards were milled rather than etched because the R strips were focused on the target region with each strip covering the same solid angle. This meant that each R board had strips of slightly different size at slightly different positions. This would require a separate etching mask for each board, leading to an exorbitant expense. Once the apparatus existed for making the R boards, it was a simple matter to adapt

it to produce the ϕ boards.

As mentioned earlier, the EMLAC was divided along the beam axis into two sections. Strips covering the same solid angle in each section were ganged together with connector strings and read out by the same amplifier. These strips formed what was known as a *tower*. In the front section, 11 R strips were connected together to make a tower.[14,22]

Hadronic Calorimeter   Immediately downstream of the EMLAC was the hadronic calorimeter (HALAC). This also was a sampling calorimeter with liquid argon as the active material, but used stainless steel as the absorber. Since showers produced by hadrons are typically much broader than electromagnetic showers, the granularity required of this detector was much less fine. In this case, a pad geometry was selected. The HALAC comprised 9.6 absorption lengths of material.

The HALAC consisted of 53 1 inch thick stainless steel plates interleaved with sampling units known as "cookies." The detector cells were distributed with 14 cells in the front section and 39 in the back. These cookies consisted of seven layers of copper clad G–10 glued together into an octagonal unit of 4 m diameter. The cookie contained the high voltage planes, argon drift gaps, and detector pads. A cut-away drawing of one of these cookies is shown in Figure 10.

The triangular pads of the HALAC were arranged in rows of two pad strips. The strips were separated by regions of equal height containing the readout strips connecting the pads with the periphery. The readout strips were covered with G–10 slats to provide structural rigidity for the cookies and to prevent the readout strips from themselves collecting charge.
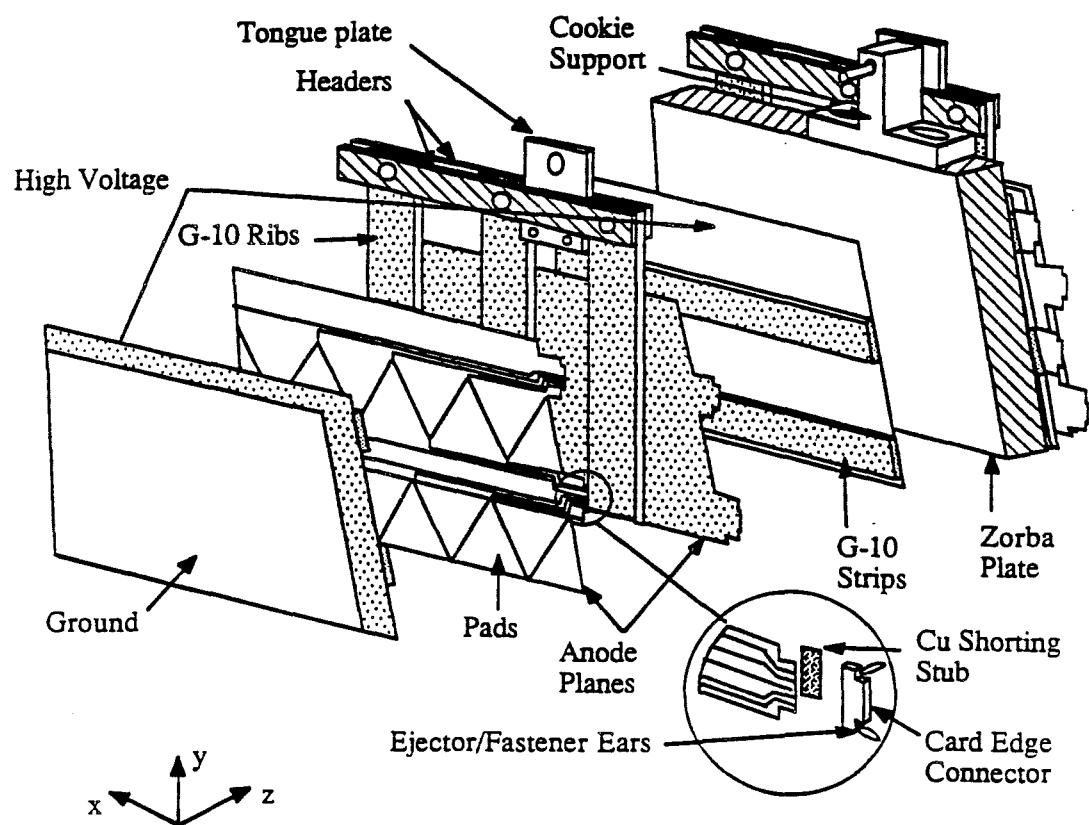
Figure 10   HALAC Detector Element ("Cookie")

The pads in a cookie were milled into copper clad sheets of G–10 using a Gerber Instruments routing table at FNAL. This method of construction was preferred for the same reasons as discussed for the EMLAC.

Forward Calorimeter   Since the LAC was built with a hole in each of the two calorimeters, a significant percentage of energy from any given interaction could escape down the hole. Most of this energy was contained in the fragmentation of the noninteracting partons of the beam particle and the fragments from the breakup of the target nucleus. To measure this energy, the University of Minnesota supplied a calorimeter downstream of the LAC to measure particles in this forward region.

The forward calorimeter, as shown in Figure 11, was a sampling calorimeter constructed of 1.9 cm thick steel absorber plates and 4.6 mm thick sheets of acrylic scintillator. It was 114 cm in diameter and had three modules that contained 28 steel plates, spaced 6.3 mm apart, and 29 scintillator sheets each. Into both the steel plates and the scintillator sheets, a set of 76 holes were drilled on a 11.5 cm grid. Inserted into these holes were 1.0 cm diameter wave shifter rods with phototubes attached at one end. The wave shifter rods were made from BBQ doped acrylic.[*] These rods were also doped to absorb UV light. This reduced anomalous signals produced by particles passing down the BBQ bars themselves.

The signal from each wave shifter was digitized by custom CAMAC modules developed by the University of Minnesota. When the experimental trigger was

---

[*]   BBQ is an organic dye that shifts the blue light created by the passage of charged particles through the scintillator sheets to green light which could be detected by the phototubes.

Steel Absorber

Scintillator

BBQ Wave
Shifter Bars
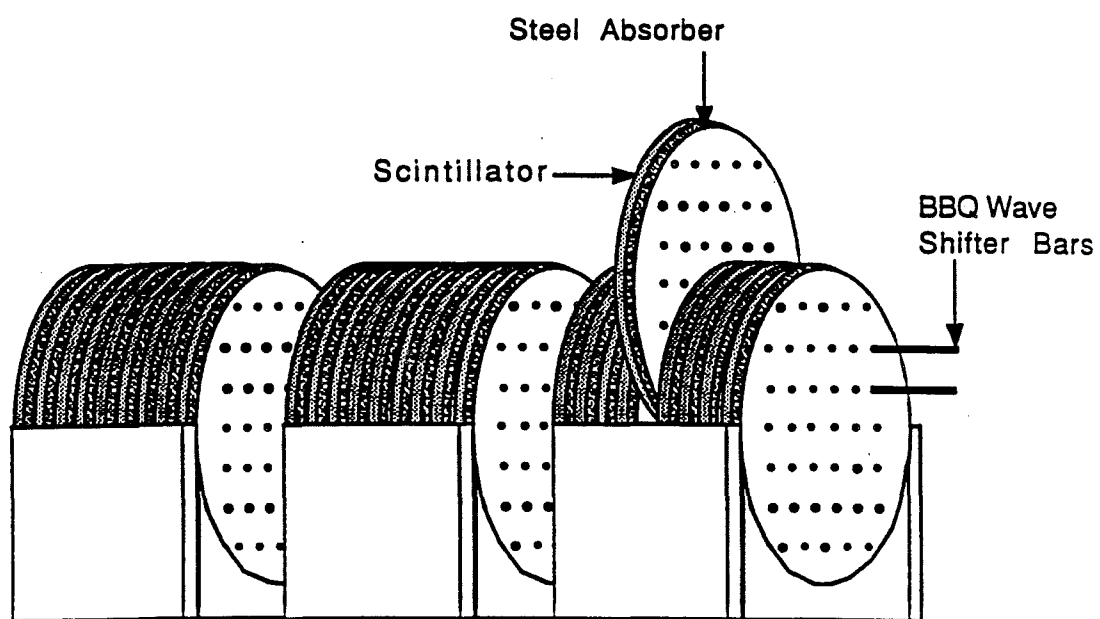
Figure 11   Forward Calorimeter Construction

received, an voltage "history" of the preceeding 2.56μs was available for each phototube.[23]

3. Data Acquisition

This chapter discusses the data acquisition system used by E706. Experiments in high energy physics have grown to require many thousands of data channels. Data acquisition is performed by several layers of computers, software, and front end electronics. The system used to handle the flow of information from the spectrometer is discussed below. This includes the instrumentation electronics as well as the computers and software necessary to record the extracted data. Since the author spent most of his time developing the LAC instrumentation, special attention will be paid to details of the LAC readout system.

3.1 OVERVIEW

<u>Central Control</u> The central unit of the data acquisition system was a Digital Equipment Corporation (DEC) Microvax II computer (μVAX). This machine controlled the data-taking and monitoring tasks, and wrote data to tape. From this central hub, tasks were assigned to several subsidiary systems. Figure 12 shows a block diagram of the data acquisition environment at MW during the data run.

The *VAXONLINE* software package was used on the μVAX as the master control program. *VAXONLINE* was a set of programs developed by FNAL for use in High Energy Physics data-taking environments. It addressed several standard requirements of any data taking system (*e.g.* writing data to tape, buffer management, interprocessor communication) and allowed for rather simple modification to meet individual needs.

37
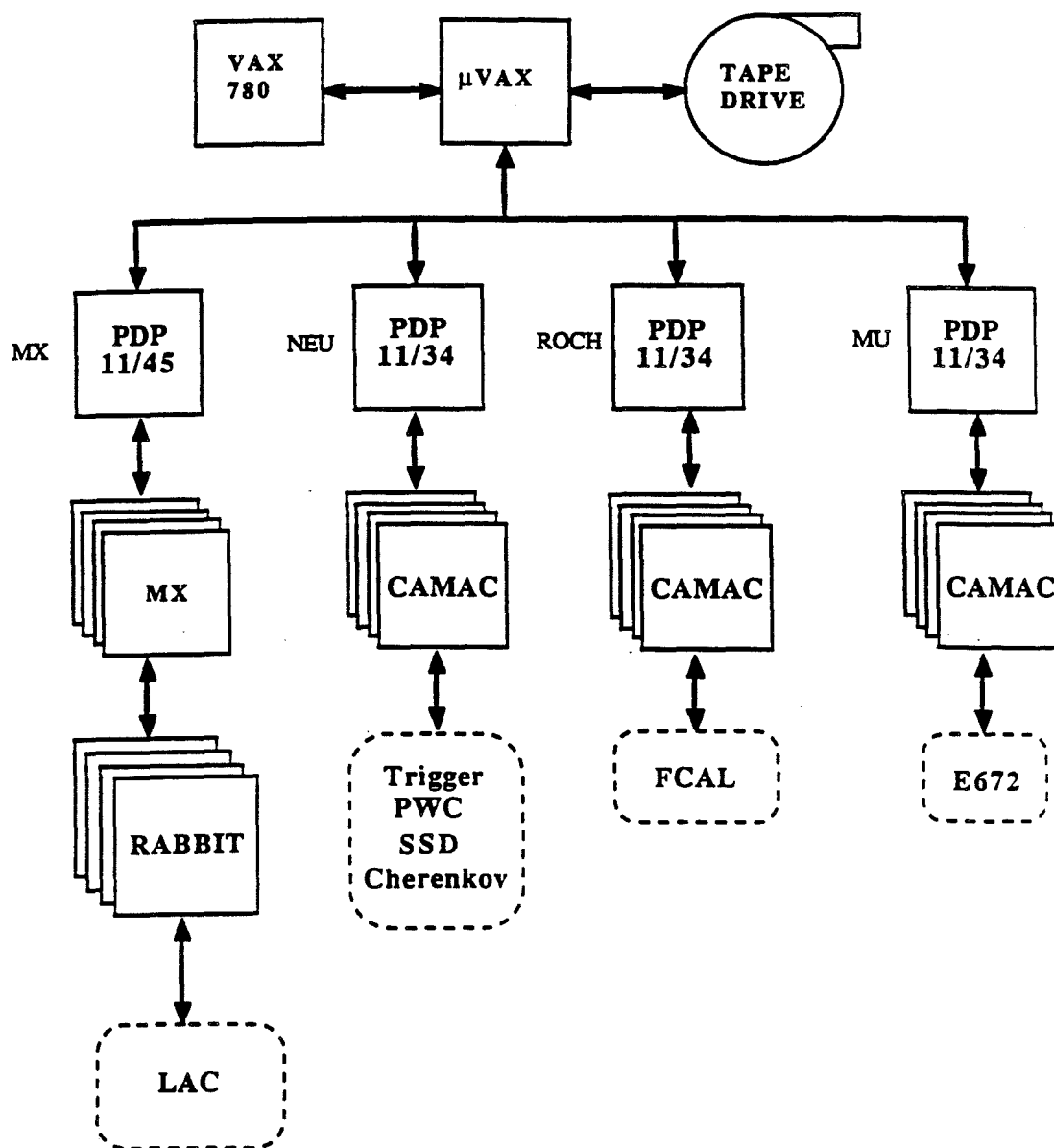
Figure 12   Block Diagram of the Data Acquisition System

VAXONLINE consisted of four major processes. The first process, *GLOBAL_MENU*, was the user interface for the other three processes. The second, *OUTPUT*, managed the output of data to storage devices. *RUN_CONTROL* was the user interface to the data acquisition system and the process from which user instructions were issued. The fourth process, *EVENT_BUILDER*, took the data from the subsystems, concatenated it and made it available to other processes.

A subset of the data from *EVENT_BUILDER* was sent to a DEC VAX 780 computer for online data analysis. Several programs monitoring event quality were run with one of the most useful being a graphical display of signals from the various pieces of the spectrometer. These monitors were very useful in noting malfunctions in the various pieces of apparatus and debugging problems.

Below the μVAX in the acquisition chain were four DEC PDP 11 series minicomputers. Each of these controlled a separate section of the MW spectrometer. One controlled the Cherenkov, SSD, and PWC readout as well as the trigger logic and scalers.* A second PDP controlled the LAC readout, another the forward calorimeter. The fourth PDP controlled the readout of E672's muon system. All of these subsystems, with the exception of the LAC, used CAMAC electronics for their instrumentation and were read out using standard parallel and serial links. Data acquisition for the LAC used the RABBIT system which will be discussed in detail in a following section.

Data Taking   Data collection was segmented by the experimenters into periods known as *runs*. The term "run" was used to refer to a collection of data during

---

★ The trigger logic will be described later and the scalers were used to count various quantities (*e.g.* number of spills, beam particles).

which the conditions of the experiment could be expected to be uniform. This was a useful subdivision for data analysis and imposed a certain structure on the data acquisition. A run had an upper limit of one 6250 bpi magnetic tape filled with data. When everything was operating smoothly, this translated into ≈ 30 minutes of elapsed time.

When taking data, the operator would select options within *RUN_CON-TROL* to initiate different data acquisition tasks. At the beginning of a run, various system parameters were recorded into a database and initialization routines were started on the separate subsystems. Every few runs a *cold start* routine was initiated on the subsystems. This routine completely reset the subsystems and recorded more detailed information about the system into databases (*e.g.* pedestal values and gains of the electronics modules). Once these initialization routines were completed, the operator would enable the experimental trigger and start the run. When the run was completed, summary information was recorded and the operator could enable another run or stop taking data. Given the speed with which the experiment could fill a data tape, the ability to do this from one console and have the computer handle much of the synchronization of the subsystems was invaluable.

3.2 TRIGGER

Collecting and recording the data from all the subsections of the experiment took a much longer time than the average time between beam particles; a trigger was needed to select interesting events. In general, this is a difficult task and one worries about introducing unwanted biases in event selection.[24]

E706 had six different experimental triggers: *Beam, Interaction, Single Local, Two Gamma, Local• Global Low,* and *Local• Global High.* The discussion that follows defines these triggers. All of these triggers required that the computers be ready and that there be at least one particle in the RF bucket from the accelerator. The former was determined within the trigger control logic from signals from each of the data acquisition computers. The latter required the combination of a signal in beam counters BA and BB without one in BH, $(BA \cdot BB \cdot \overline{BH})$, in coincidence with a BEAM_GATE signal.[†] These were the only requirements for the *Beam* trigger.

All the other triggers required that there be an interaction and that there be no beam particle within three beam buckets before or after the interaction bucket. An interaction in the experiment was defined by a signal in any one of four scintillators (SE1, SW1, SE2, and SW2) in coincidence with a beam signal.

The last four triggers required information from the LAC and took a relatively long time to generate. To prevent the loss of information from this long delay, a PRETRIGGER signal was generated that caused the experiment to latch all data. This pretrigger was generated whenever the interaction trigger was satisfied and there was more than $1.7\,\text{GeV}/c$ of p_T deposited in any octant of the LAC. The p_T in the calorimeter was determined using

$$p_T = \sum_{strip=i} E_i sin\theta_i \tag{3.1}$$

where the summation was done over the radial strips in the LAC (see discussion in Section 2.3) and θ_i was the angle from the beamline to the ith strip in the

---

[†] BEAM_GATE was a signal provided by the accelerator to indicate the possibility of live beam in the beam line.

LAC. Since the LAC signal risetime was $\approx 300\,\text{ns}$, the PRETRIGGER was rejected when there was a substantial amount of p_T deposited within the preceeding $300\,\text{ns}$. This avoided situations where two low p_T depositions overlapped in time and could fake a high p_T event. The amount of "early p_T" was limited to $< 1.5\,\text{GeV/c}$. After the pretrigger was issued, the conditions for the last four triggers were evaluated and if not satisfied the electronics was reset and the experiment readied for another trigger.

Trigger	Threshold	Settings		
Threshold	Run ≥ 1811	≥ 2293	≥ 2311	≥ 2905
Local p_T Low	1.2 GeV/c			
Local p_T High	4.2 GeV/c	3.6 GeV/c		3.0 GeV/c
Global p_T Low	2.5 GeV/c			
Global p_T High	4.0 GeV/c		3.6 GeV/c	

Table 3   Trigger Threshold Settings

As will be discussed in Section 3.4, there was a provision for a "fast" signal from the LAC to provide information for the experimental trigger. There were modules that summed the weighted outputs of the LAC channels. These last four triggers all used some combination of these summed signals as part of their definition. Basically, sums sensitive to local and global deposition of p_T were used. The local signals were determined by measuring the p_T deposited in a small (8 cm in R by 1 octant in ϕ) section of the EMLAC. This region contained most of the energy of a single electromagnetic shower. The sums for these regions were each compared to a high and low discriminator level. LCLPTHI and LCLPTLO were the logical OR of these comparisons. The p_T deposited in an octant was tested against a high and low level to produce the global trigger signals GLPTHI and GLPTLO. The settings for these thresholds are listed in Table 3.

These definitions of LAC energy meant that each octant of the LAC could be run as a separate experiment. In fact, all the trigger quantities (*e.g.* PRETRIG-GERs, trigger counts) were determined individually for each octant. The resulting values were compared against each other as a check on trigger consistency.

The Single Local and Two Gamma Triggers   These triggers were simple combinations of LCLPTLO and LCLPTHI. The Single Local trigger was satisfied by the coincidence of PRETRIGGER and LCLPTHI within an octant. This trigger was most effective in triggering on direct photons and $\pi°$s where the p_T from the triggering particle was contained in one local element. The Two Gamma trigger was satisfied by a coincidence of LCLPTLO and PRETRIGGER in both an octant and any one of: the opposite octant or either of its two neighbors.

The Local • Global Triggers   The two Local • Global triggers, Local•Global High and Local•Global Low, were generated by requiring LCLPTLO in coincidence with GLPTHI and GLPTLO respectively. These triggers were designed to select direct photons and $\pi°$s, as above, but also to trigger on low energy, symmetric $\pi°$, η, ω, ...mesons that might not satisfy the Single Local trigger.

Trigger	Trigger Fraction	Prescale Factor
Local • Global High	25–30%	1
Local • Global Low	10–15%	10
Single Local	45–50%	1
Two Gamma	3–5%	1
Interaction	4–5%	2.25×10^5
Beam	2–3%	2.25×10^6
Di-Muon (E672)	30–50%	1

Table 4   Trigger Fraction by Trigger Type

<u>Scalers</u> The Local • Global High trigger was the main trigger for the experi-
ment[†] but it was by no means the most common trigger. In order not to be
swamped by the more frequent triggers, Beam, Interaction and Local • Global
Low triggers were prescaled as shown in Table 4. Each of the trigger quantities
was counted in a CAMAC scaler read out once per spill. This was done to
monitor trigger performance and for use in cross section normalizations.

3.3 THE RABBIT SYSTEM

Data acquisition and trigger signal processing for the LAC portion of E706
was performed using the RABBIT (Redundant Analog Bus Based Information
Transfer) system developed by the Particle Instrumentation Group (PIG) at
FNAL.[25] The RABBIT system was developed in response to the increasingly
large size of experiments' electronic readout systems.

The unique feature of RABBIT was the analog nature of its bus. The RAB-
BIT backplane had two largely redundant busses (called Top and Bottom) with
a pair of lines isolated from the digital signals. The concept was to provide an
electronic environment where analog information from individual channels could
be multiplexed, at acceptable speed and precision, into a single ADC. This in-
volved careful construction of the backplane and signal terminations as well as
strict control over backplane signal timing. While an ADC was digitizing in
RABBIT, there was no need for any logic signals to change state on the back-

---

† Although the experiment was designed to use this trigger as the main trigger, it was
  discovered that this trigger never achieved 100% efficiency. Its maximum efficiency was
  about 65%. This problem in coincidence with the greater effect of image charge problems
  caused the author to use the single local trigger for this analysis. While the acceptance for
  η is reduced with this trigger, the trigger is better understood and results more reliably
  converted to cross-sections.

plane. Since the ADC was typically the most expensive component in a readout system, multiplexing many signals onto a single ADC had the virtue of saving money. Also, effects due to ADC calibration and drifts could be minimized.

The other main feature of the RABBIT system was its redundancy. As mentioned above, the two busses on the backplane were nearly 100% redundant. The only exceptions were a few lines used for timing and calibration purposes. Every channel in the system could be addressed via either or both of these two busses. Therefore single channel failures were less likely to block the readout of an entire crate of electronics. This was vital for collider environments where access to the electronics was only possible on a limited basis. Even in environments such as E706's, where access to the electronics was possible while taking beam, it was preferable to defer minor repairs to some accelerator down time rather than lose valuable beam.

Figure 13 shows a block diagram of the data acquisition for the LAC. Data from the RABBIT system was buffered in a DEC PDP 11/45 and made available to the concatenating μVAX. The PDP collected sub-events from each of nine list driven sequencers known as "MX"s. Each MX in turn communicated with up to eight crate controllers, digitizing and buffering the data for up to three events.

There were three types of modules used in the system: Front End Electronic Devices (FEED), crate control modules and the data acquisition sequencer (MX). E706 developed a module, called the LACAMP (for Liquid Argon Calorimeter AMPlifier) with 16 channels of integrating amplifiers and eight channels of time to voltage converters as its FEED. The same module was used for
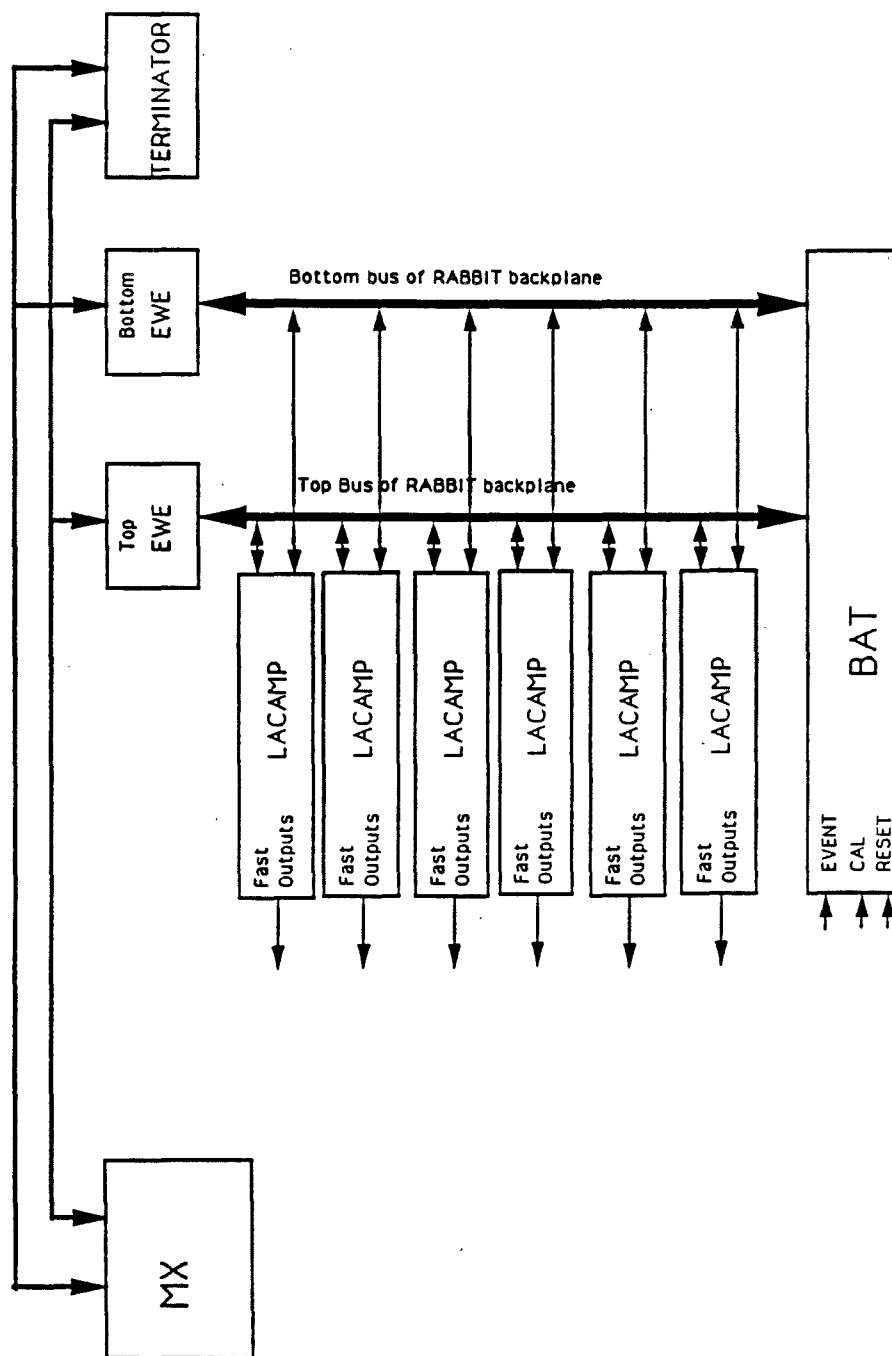
Figure 13   Block diagram of LAC Data Acquisition

both the hadronic and electromagnetic sections of the LAC. EWE–II (known as "EWE"s) modules, developed for the Collider Detector Facility (CDF), were used as crate controllers. The BAT (Before After Timer) was another control module developed for E706. It generated the timing signals required by RABBIT based on information from the trigger system.

The following few paragraphs give a quick overview of how data was acquired from the LAC. Individual elements of the readout system will be described in detail in their own sections.

Figure 14 shows a timeline of signals at various stages of the front end electronics. Figure 14(a) shows the triangular current pulses from charge deposited in the LAC. The output from the LAC amplifiers are shown in Figure 14(b). These amplifiers produced a voltage signal proportional to the amount of charge deposited on their respective strips in the calorimeter. This signal was then sent to trigger, timing, and delaying circuitry. The outputs of these circuits are shown in Figure 14(c–e). If the trigger signal satisfied trigger requirements, BEFORE and AFTER signals were sent which stopped the timing clocks and sampled the delayed output of all the amplifiers.

After all the samples, V_{BEFORE} and V_{AFTER}, had been taken and stored on capacitors, the voltage differences $V_{AFTER} - V_{BEFORE}$, for each LAC amplifier, were digitized by the ADC on the EWE and the results stored in buffers on an MX. The voltages V_{time} were also digitized to give pulse timing information. As shown in Figure 13, the MXs were then read out by a PDP 11. At this point, all the pieces from the LAC for a given event were available.

PDP 11   A PDP 11/45 was used as the system controller for the LAC DA. The
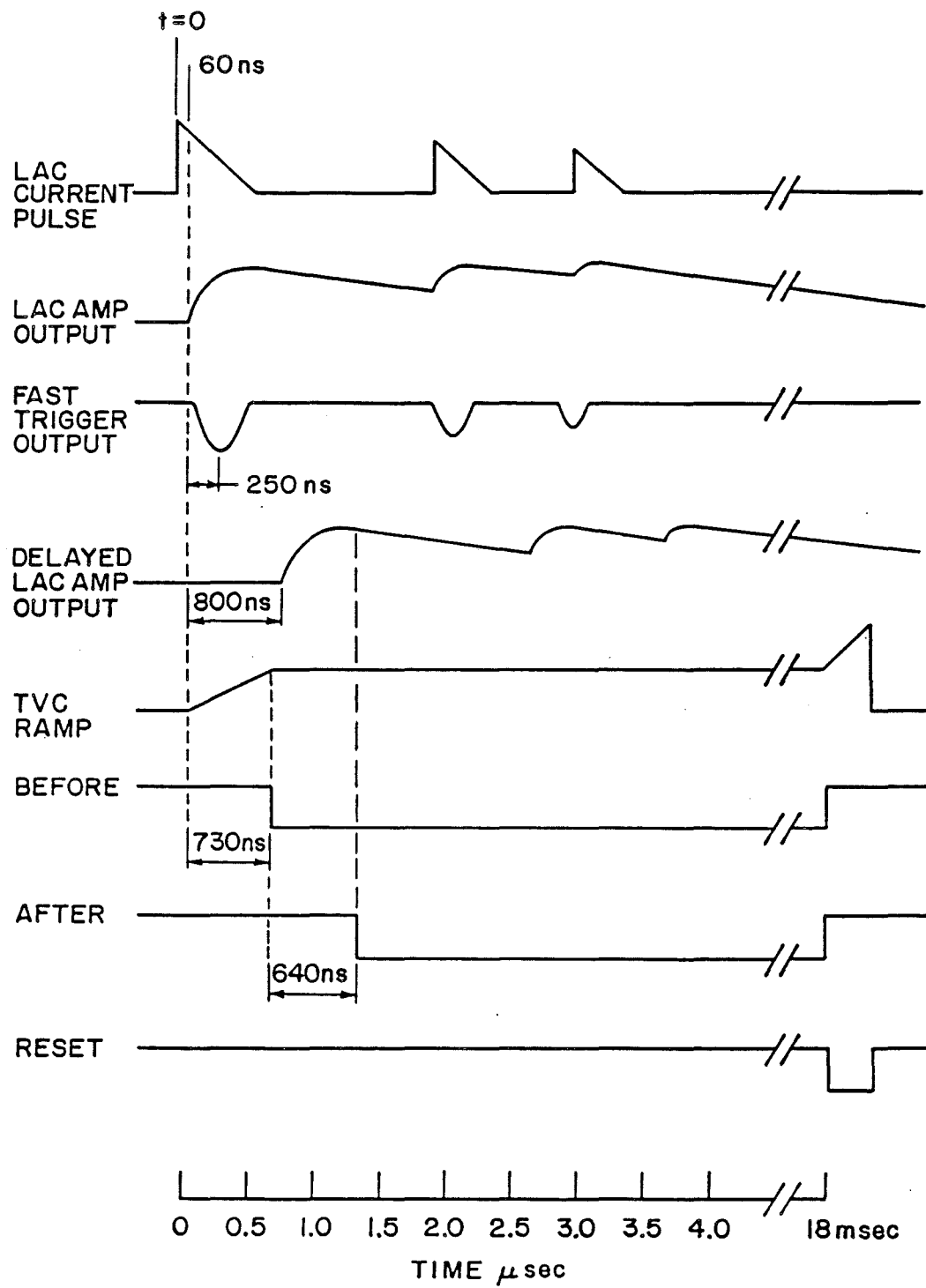
Figure 14   Signal Timing in LAC Data Acquisition System

PDP's function in data taking mode was to coordinate MX tasks, concatenate subevents from the separate MXs, and send events to the μVAX. It also served as an event buffer for short bursts where the μVAX was unable to keep up with the trigger.

Communications with the μVAX took place over high speed DR–11W data links using the *CDPACK* protocol developed at FNAL.[26] Communications with the MX used UNIBUS* modules, called UNIBOXs, developed by PIG. The UNI-BOX was a memory mapped interface module which performed the conversion of 32 bit MX data into the 16 bit words used by the PDP. It also performed the address translations to select the MX memory to be read or written.

<u>MX</u> † The MXs performed many of the same functions, at their level, as the PDP on the higher level. An MX controlled up to four crates of RABBIT electronics. It handled the instruction list for the EWEs and performed some manipulations on the results. There was also memory to buffer a few (usually three – dependent on the buffer size used) events' data to smooth out the load on the PDP. The readout of the RABBIT crates was performed by 11 MXs – nine to read out the LAC amplifiers and two for the RABBIT trigger modules.

An MX consisted of six distinct memories: the UM (EWE memory) which held the list of instructions for the crate controllers, EM (Event Memory) which buffered the output of up to three events for the PDP 11, IM (Instruction Memory) which held the instruction list for the readout program, and A, B, and C

★ UNIBUS is an open architecture bus standard for DEC PDP computers.

† A bit of trivia for the curious: The militaristic title of the MX is at odds with the bucolic titles of other pieces of the RABBIT system. It stands for M8, in octal roman numerals, the successor of the M7 (Magnificent Multi Muon Mass and Momentum Measuring Machine) designed by the same group.

memories whose purpose was user definable. The MX was optimized, however, to perform calculations of the form $A + B \times C$, so the B memory was intended to hold raw data and A and C the correction coefficients. Since this was the initial run, no corrections to the data were performed inside the MX.

The assembler used to generate the contents of the IM was produced by PIG and allowed for structured programming. It was produced primarily by Walter Stuermer and Susan Littleton of PIG.

The readout program contained three separate tasks that were used during data taking. One was the standard readout task. The other two were calibration tasks: one to gather pedestals for all the channels and the other to determine gains. For the readout task, a loop over EWEs was performed consisting of the following steps. The EWEs were setup for their first channels and the ADC started. After all the ADCs were started, the MW would poll each EWE in turn to determine if its ADC conversion was finished. If the EWE was done, the data was read out, the EWE setup for the next channel in its list, and the next conversion started. Otherwise, the next EWE in the loop was tested. The polling was necessary because of a *zero suppression* feature used on the EWEs. This was a method by which the signal presented to the ADC was compared against a minimum value and only converted if above that minimum. Since the testing against the threshold was much faster than the ADC conversion[‡] one could not be sure which ADC would finish its cycle first.

The MX could service multiple EWEs because the data bus connecting MX and EWE allowed for device IDs. Up to four EWEs could be daisy–chained

---

[‡] The test over threshold (TOT) decision took 3 μs and the digitization took 18 μs.

on one data bus. This was done for economic reasons to reduce the number of MXs required ($\approx$ \$20,000 each) and the number of cables between the counting house and Faraday room. The price paid was in readout speed. It was found that with three EWEs per data bus (six EWEs per MX) the polling loop took longer to complete than the ADC digitization so the zero suppression advantage was defeated[§]. This was largely due to signal propagation delays and settling time in changing signal direction on the data bus.

<u>Optical Couplers and Data Cables</u> A EWE and an MX were connected with a two cable, bi-directional, data bus. This consisted of one 26 and one 40 conductor Spectra–Strip cable with a maximum length of 225 feet. The length was broken at the Faraday room wall by an optical coupler device built by the University of Rochester. This was done to minimize noise propagation into the Faraday room and to act as a signal booster in these long cable runs. The cable length between the optical couplers and MX was fixed for all MXs at 150 feet.

Mounting the cables between the optical couplers and the MX was not trivial because the gantry supporting the LAC (and the optical couplers) had to be able to move laterally to the beam with the data cables installed. At least six feet of travel in either direction was necessary for calibration purposes. The gantry also had to be moveable to the west wall of the experimental hall for maintenance. This was accomplished with a cabling system designed at FNAL, called the festoons, to manage the excess cable. From the base of the festoon to the counting room the cable was routed in armored cable trays across the

---

§ Although the advantage in readout speed within the MX was defeated, there was less data to transfer to the PDP and μVAX and write to tape. This <u>did</u> help maximize the data acquisition speed though the full system.

floor of the experimental hall and through steel pipes into the counting house.[¶]
Cables inside the Faraday room were distributed via vinyl cable ducts mounted
on the room walls and ceiling.

EWE As mentioned earlier, the EWE module was the RABBIT crate controller
and digitizer. There were, in fact, two EWEs in each crate – one to control
each of the two (Top and Bottom) busses on the backplane. The two EWEs
were identical; only the position in the crate determined which bus a EWE
controlled.[*] Consider just one EWE for the moment, with the understanding
that both EWEs performed similar tasks on their respective busses.

Figure 15 shows a block diagram of a EWE. The functions can be eas-
ily divided into a digital and analog section. The digital section consisted of
eight registers for communications with the MX. The analog section consisted
of an analog multiplexer to select the input polarity, a 16-bit DAC to provide
a pedestal subtraction for each channel, Test-Over-Threshold (TOT) circuitry
to provide hardware zero suppression, and a 16-bit ADC section with software
selectable gain and offset.

The eight registers were known by the following names: Control, Status,
Channel Address, Pedestal, Threshold/Control, ADC, Read Data, Write
Data. The contents of the Control register determined what action the EWE
would take on receipt of an XQT signal from the MX. The XCONV bit enabled

---

¶ This level of precaution was taken to prevent the data cables from being cut by accident
during the run. Even these precautions were not sufficient in the end. The experiment
was shut down one day for several hours because a mouse chewed through several of the
data cables.

* Slot 24 in a RABBIT crate has connections for the Top bus signals but only power
connections to the Bottom bus. Slot 23 has Bottom bus signal connections but none for
the Top.
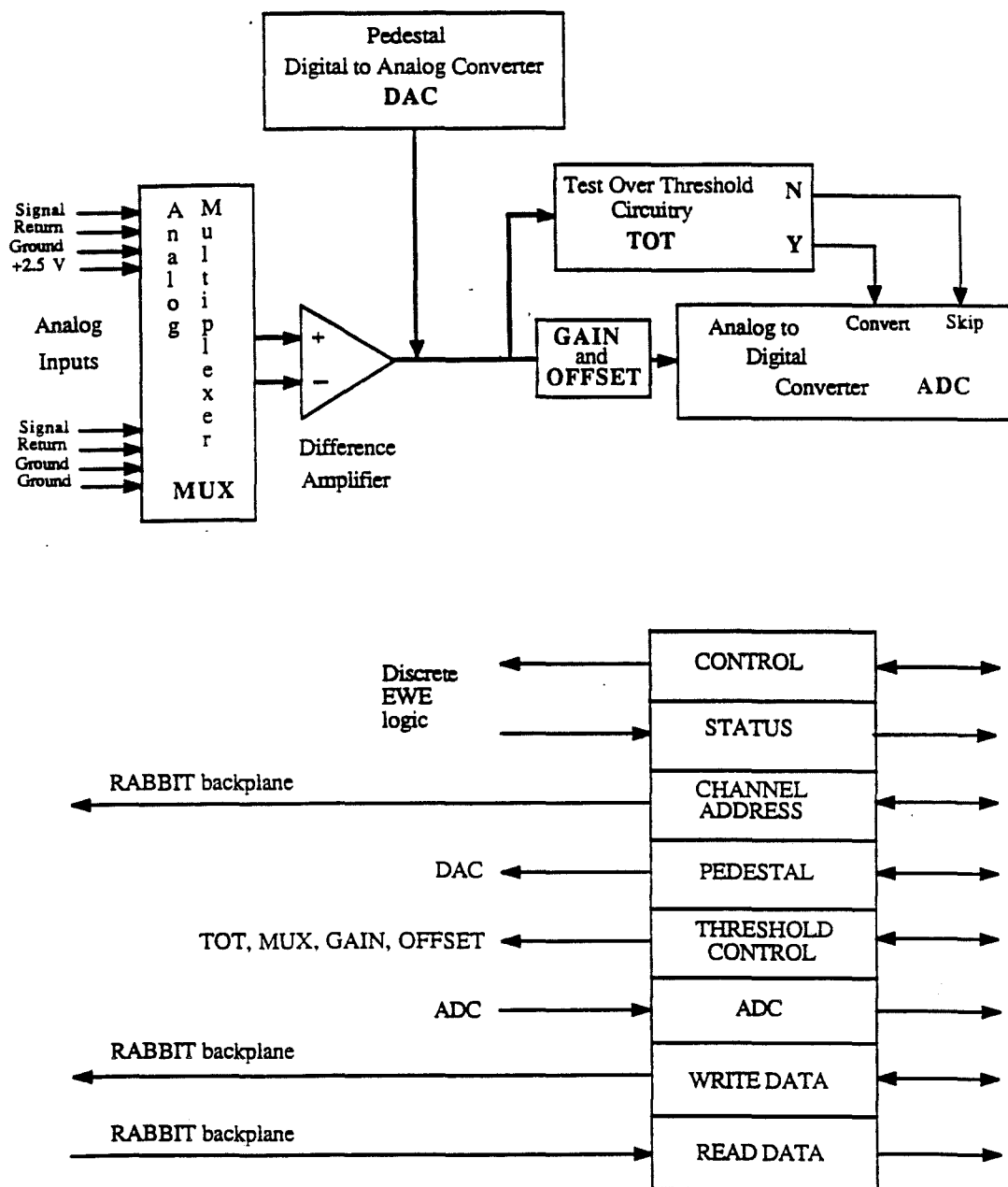
Figure 15   Block Diagram of RABBIT Crate Controller (EWE II)

	EWE		Register		Bit		Assignments	
Bit	Command	Status	Channel Address	Pedestal	Threshold Control	ADC	Write Data	Read Data
0	XCONV	TOP	SA(0)	0	THRESHOLD(0)	0	0	0
1	TOT	SKIP	1	1	1	1	1	1
2	RABLOP	–	2	2	2	2	2	2
3	SKIPEN	–	3	3	3	3	3	3
4	MXCS	–	4	4	4	4	4	4
5	MXCLR	–	5	5	5	5	5	5
6	DIGOP	DATA	MA(0)	6	6	6	6	6
7	IDIR	DONE	1	7	7	7	7	7
8	–	PARERR	2	8	ASEL(0)	8	–	–
9	–	DSTRB	3	9	1	9	–	–
10	–	–	4	10	2	10	–	–
11	–	–	5	11	GAIN(0)	11	–	–
12	–	–	–	12	1	12	–	–
13	–	–	–	13	OFFSET(0)	13	–	–
14	–	–	–	14	1	14	–	–
15	–	ERROR	–	15	2'S COMP	15	–	–

Table 5   EWE Register Assignments

the ADC for digitization. The TOT bit made the ADC conversion conditional on the results of the threshold test. RABLOP enabled a hardware readback loop for testing purposes. MXCS and MXCLR started timing cycles on the BAT. DIGOP enabled a byte wide digital transfer across the backplane. IDIR determined if the byte was sent to or read from the backplane.

The Status register consisted of 16 different bit flags for information about transaction status, seven of which were implemented in this design. TOP signified whether the EWE controlled the Top bus of a backplane. SKIP signified a channel to be skipped. This feature was not used. DATA and DONE flagged the status of the last operation. DONE was asserted after the command completed and DATA signified the presence of new, valid data in the ADC register. ERROR

indicated an error condition – either PARERR or DSTRB. PARERR denoted detection of a parity error on the last data transferred from the MX. DSTRB was used to signify an inhibit on data strobes to that EWE (data bus arbitration had not been completed).

The contents of the Channel Address register determined which module and subaddress in the crate was addressed. Six bits of module address determined the slot and six bits of subaddress were used to select a function within the module.

The Pedestal register stored the setting for the pedestal DAC.

Address	ASEL	GAIN	OFFSET
0	Signal - Return	×1	90%
1	Ground - Return	×2	10%
2	Return - Ground	×4	0
3	Ground - Ground	×8	0
4	Return - Signal	–	–
5	Ground - Signal	–	–
6	Signal - Ground	–	–
7	+2.5V - Ground	–	–

Table 6   Settings in the Threshold/Control Register

The Threshold/Control register stored the settings for the TOT threshold DAC, the analog multiplexer, ADC gain and offset. The TOT DAC setting determined the TOT threshold. The results of possible settings for ASEL, GAIN, and OFFSET are shown in Table 6.

The ADC register contained the results of the last ADC digitization performed. The Read Data register contained the last byte read from the backplane and the Write Data register contained the byte to be written to the backplane.

The typical cycle for digitizing a LACAMP channel was: load the `Channel Address` register with the module and subaddress of the channel of interest, load the `Pedestal` register with the pedestal value for that channel, load the `Threshold/Control` register with its proper settings, set the `Control` register to `TOT` and `XCONV` and then issue the `XQT` signal. This instruction order was found to be important to allow the analog lines to settle. For making accurate decisions near threshold, one needed to insert a software delay between filling the registers and executing a TOT. 500 ns was deemed to be sufficient for an accuracy of ≤ 20 ADC counts.

The function of the EWE can be described most easily by referencing Figure 15 and following an analog signal through the digitization process. The analog levels (`Signal` and `Return`) from the backplane were each inputs to two analog multiplexers at the first stage of the EWE. `Ground` and a $+2.5\,V$ reference were the other inputs to the multiplexers. One could choose from several combinations of these analog levels: `Signal − Return`, `Return − Signal`, ... The combinations are listed in Table 6.

The difference between these two levels was shifted by the output of the pedestal DAC. This was done to remove pedestal differences for individual channels. This level was then multiplied by the selected `GAIN` and presented to the ADC for digitization. The voltage level before the programmable gain stage was also sent to the TOT section of the EWE. This section had a fixed gain stage of 65 at the input followed by a programmable attenuation (`THRESH/255`). The resultant level was compared against a fixed window of $\pm 50\,$mV. If the command register had `XCONV` set without `TOT` then the ADC digitized the level regardless

of TOT section results. If, however, TOT was selected, then the results of the TOT section determined whether or not a digitization was performed. If the scaled voltage level in the TOT section was outside the window, then the ADC digitized the level. Otherwise, the ADC did nothing and the status register was set to show that the value did not exceed the minimal level in the TOT section (DONE but not DATA).

BAT   On the other end of the RABBIT backplane from the EWE was a module known as the BAT (Before After Timer). This module, as shown in Figure 16, had three primary responsibilities: it terminated the signals generated from the EWE, it generated the timing signals needed by the LACAMP modules, and it monitored crate parameters.

There were two separate cycles of timing signals available from the BAT. These were the EVENT and CALIBRATION cycles shown in Figure 17. For an EVENT cycle, the BAT immediately issued a BEFORE signal to the backplane. After a programmable delay, it then issued an AFTER signal. These two signals regulated the signal sampling in the LACAMP module. In a CALIBRATION cycle, the BAT issued a prompt TCAL1 signal and, if desired, a delayed TCAL2 signal. Again, this second signal had a programmable delay. It also issued the BEFORE/AFTER pair from the EVENT cycle. The only difference was that the BEFORE was delayed from the TCAL1 signal. The AFTER delay remained relative to the BEFORE signal to help keep the interval between the two constant during both EVENT and CALIBRATE cycles.

The BAT was also responsible for monitoring the crate environment. It contained several analog multiplexers so that the (prescaled) power supply voltages

BAT Module
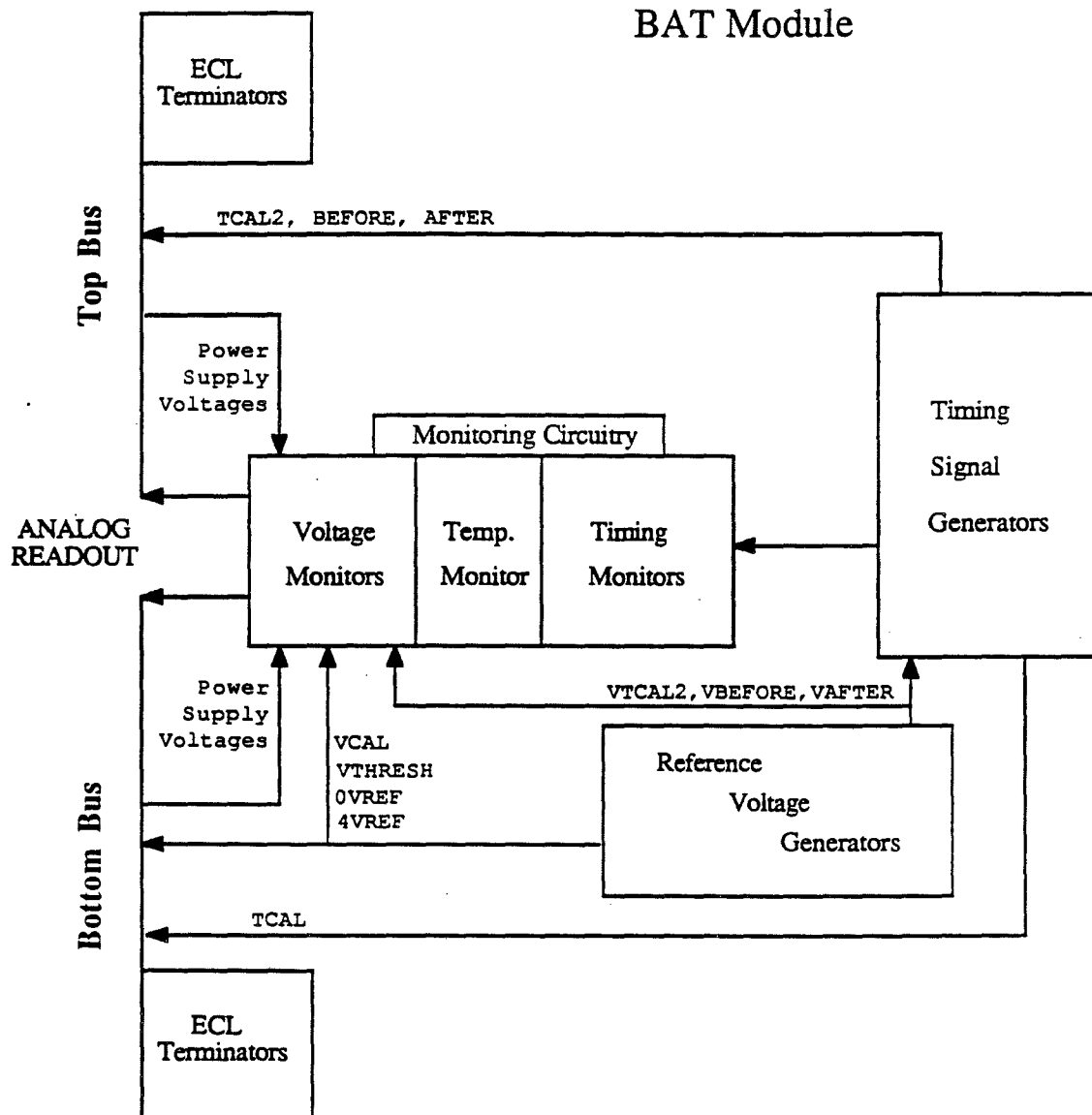
Figure 16   Block Diagram of the BAT

BAT Timing Diagram

EVENT Cycle

EVENT

BEFORE

AFTER

0.1-1.5 us

RESET

CALIBRATE Cycle

CAL

TCAL1

TCAL2

0-3 us

BEFORE

0.1-3 us

AFTER

0.1-1.5 us

RESET
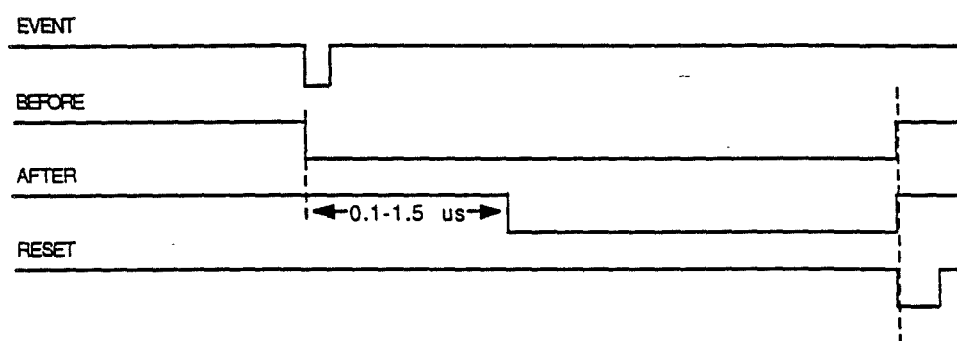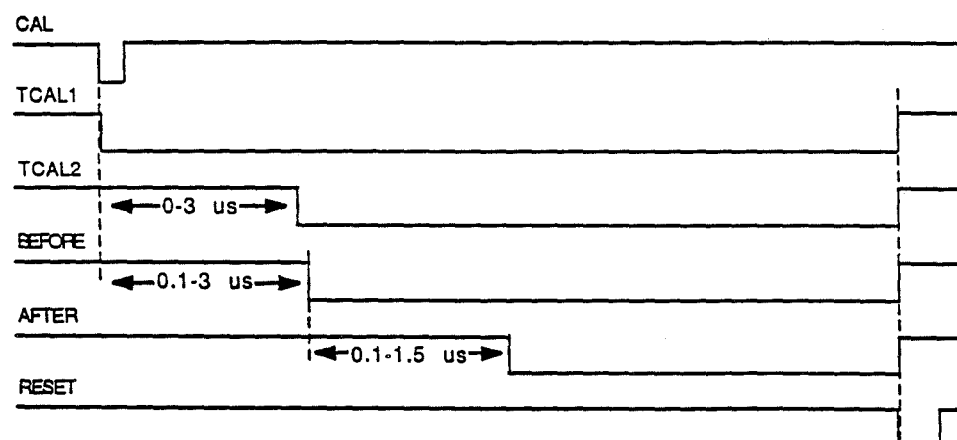
Figure 17   Timing Diagram of BAT Cycles

BAT	SubAddress	Assignments			
SubAddress	Register	Analog Level	SubAddress	Register	Analog Level
0	–	TTCAL2	15	–	–15 B
1	–	TAFTER	16	–	VTHRESH
2	–	TBEFORE	17	–	VBEFORE
3	–	Ground	18	–	VAFTER
4	–	+5 Top	19	–	VTCAL2
5	–	+5 Bottom	20	–	VCAL
6	–	–5 T	21	–	TEMP
7	–	–5 B	22	–	Ground
8	–	+7.5 T	23	–	Ground
9	–	+7.5 B	32	VCAL	–
10	–	–7.5 T	33	BFOR	–
11	–	–7.5 B	34	AFTR	–
12	–	+15 T	35	TCAL2	–
13	–	+15 B	36	THRESH	–
14	–	–15 T	37	RESET	–

Table 7   BAT Subaddress Assignments

from both busses could be monitored. The DAC outputs for the THRESH and VCAL levels could be digitized as well as the levels regulating the TCAL2, BEFORE and AFTER signal delays. There were also Time to Voltage Converters (TVCs) on the BAT to monitor the relative timing of the TCAL2, BEFORE and AFTER signals. Finally, there was a temperature sensor on the BAT to monitor the crate temperature. Any of these monitoring levels were available via either bus to permit remote system debugging. The list of BAT subaddresses is shown in Table 7.

Cabling   An area that is often underemphasized in detector design and development is the use of suitable cable and connectors. The electromagnetic and hadronic calorimeters were connected to the readout electronics by a shielded flat cable manufactured for this experiment by W. L. Gore Co. of Phoenix, Ari-

zona. Since these cables were connected at one end to the calorimeters in liquid argon and at the other end to feedthru ports at room temperature, the thermal and chemical properties of these cables were studied carefully. The cables were tested at the University of Rochester for argon contaminants and found to be no hazard to the argon purity. They were also dipped into liquid nitrogen and flexed repeatedly with no observed cracks, bubbles or other deformations occurring.

Two lots of cable were purchased with impedances of 6.5 and 13 Ω respectively.[*] Due to the size of the LAC calorimeters these cables were $\approx$ 10 m in length with a signal propagation time of 60 ns. This implied that cable termination would be important as there would only be time for a couple reflections before sampling the pulse. $1/8$ watt Allen-Bradley carbon 7.5 ohm resistors were placed in series with the signal conductors as a back-termination resistance. On the other end the amplifiers were designed to act as a resistive load of 13 Ω for frequencies between 0.02 and 50 MHz.

Around the top of the dewar were 30 access ports for connections with the outside world. 28 of these were used for LAC signal cable feedthrus, one was used for the high voltage power supplies and the last for a pulser connected to selected high voltage plates.[†] The feedthrus were constructed of short ($\approx$ 7 cm) printed circuit cards mounted in an epoxy well carved out of a G–10 panel. Figure 18

---

[*] The characteristics of the set of cables made for the EM calorimeter were miscalculated by a factor of two. These cables were found to have twice the expected capacitance. When ordering the cables for the Hadron calorimeter a sample was made reducing the width of the central conductors by two and increasing the overall gap between the conductor and the shield relative to the cables for the electromagnetic calorimeter.

[†] This last was useful in testing large sections of the calorimeter simultaneously and was hoped to be used for calibration purposes. The latter use was never successful.

Figure 18 LAC Signal Feedthru Diagram

8-channel Cable
(Gore MFF5433)
5.0 in. length

Outer Cable
Connector Board

Ground

Feed-thru

17-pin Clinch
Connectors

Low (8-9 Ω) Impedance
18-channel Cable
(Gore MFF5405)
32 ft. lengths

Viking 3VH10/1JN3

Berg 65863-063

65801-037

Berg 65801-46

(Note: Soldered
Connection between
Cable and Board)

8-pin Clinch Connectors

Inner Cable
Connector Board

Feed-thru
Mount

16 Carbon Resistors
(9±.5 Ω-at 70K)

Viking 3VH20/1JN3

Read-out Board

8 signal
lines

8 signal
lines

gnd

gnd

gnd

shows the construction of these feedthrus. Physical restraint was provided by the G–10 plate in two dimensions with the epoxy joint providing the restraint in the direction perpendicular to the plate. One of the things learned about the system was that this epoxy joint was easily damaged in the process of connecting cables. A mechanical restraint in this third dimension is recommended for future use.

On the argon atmosphere side of the feedthru, connections were made using card edge connectors with retaining ears (Viking connectors). On the other side, the connectors were 16 pin double row Berg connectors. At this point it would be possible to connect directly to the back of the RABBIT crate but short ($\approx 10\,\text{cm}$) connecting cables were used for ease in mounting and to provide access to the back of the RABBIT crates. The short cables were eight conductor cables similar in construction to those used inside the dewar. The RABBIT backplane provided two 34 pin headers per slot for input signals to the front end devices (*e.g.* LACAMPs). The LACAMP used the eight pairs of pins closest to the data busses on the top and bottom headers for passing signals from the LAC.

3.4 LACAMP MODULE

The LACAMP module contained integrating amplifiers with on-board TVCs, a calibrator, and fast trigger outputs. Figure 19 shows a functional diagram of the LACAMP module. The heart of the module was 16 charge sensitive amplifiers connected to LAC strips. The output of each amplifier was routed to three separate areas: the fast outputs, the TVC, and the Sample and Hold circuitry.

The focus of the experiment on direct photons and design of the LAC dic-
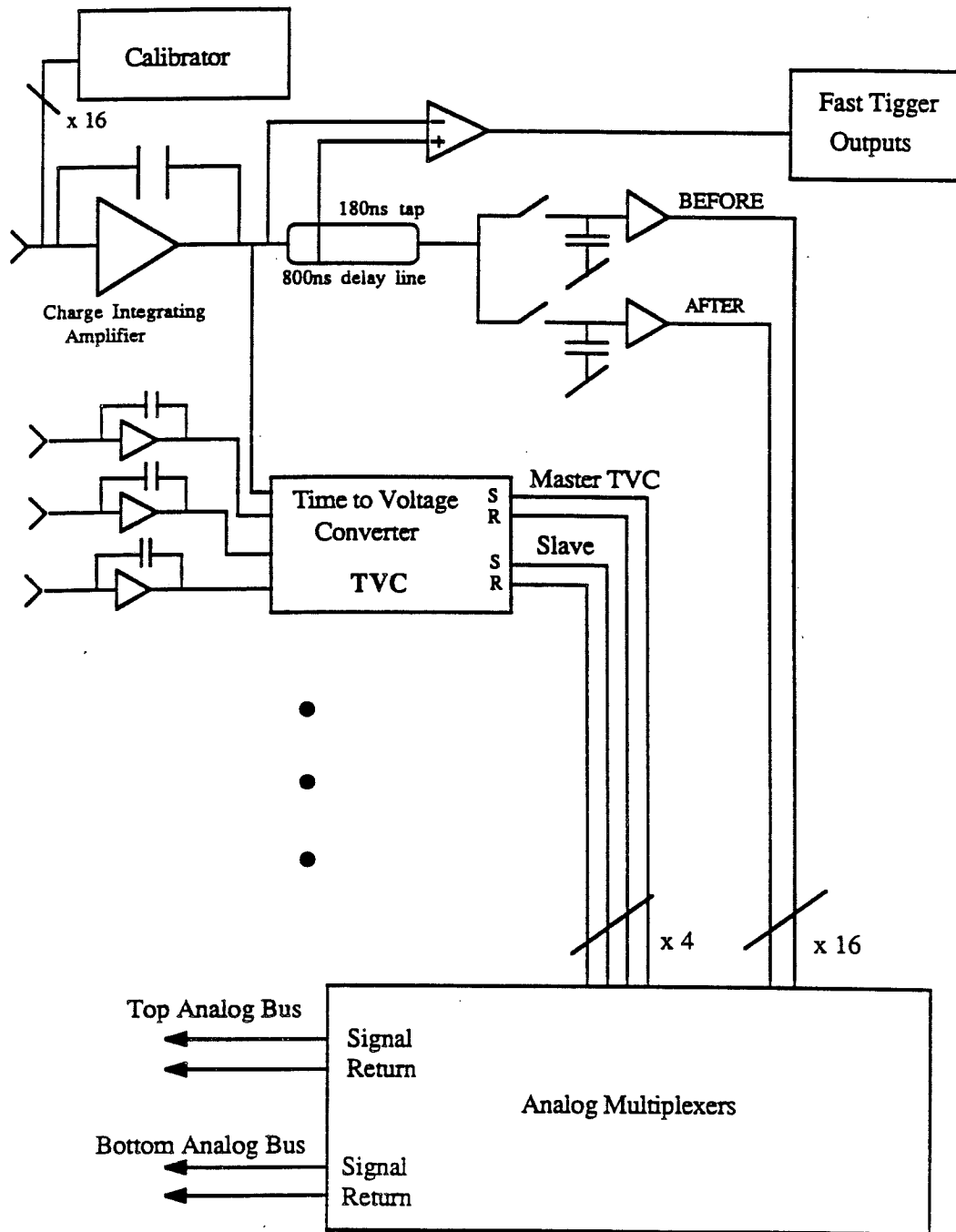
Figure 19   Block Diagram of the LACAMP

tated several requirements for this device:

- Low input impedance
- Low noise
- Remote calibration
- Fast output for trigger

- High gain
- Stability
- Low cost
- Timing information

Input Impedance The need for a low input impedance was dictated by the large

capacitance of a LAC channel. Typical capacitances in the EMLAC varied from

1 to 5 nF per channel. In the HALAC they ranged from 3 to 7 nF. Charge

collected on these capacitances discharged into the amplifier as

$$Q = Q_0(1 - e^{-\frac{t}{RC}}),\tag{3.2}$$

where t was the time after charge deposition in the LAC and R was the readout

impedance. In order to get most ($\geq$ 90%) of the pulse height in a few hundred

nanoseconds, it was necessary to have an input impedance of 10–20 Ω. Since the

LAC cables were 10 meters long with a transmission time of 60 ns, more than

two reflections would distort the digitized pulse. This implied that the amplifier

impedance must closely match that of the cable.[27]

In order to properly terminate the cable the amplifier should have a resistive

impedance at all frequencies contained in the LAC signal. Figure 20 shows a

graph of the open–loop gain* of the amplifier as a function of frequency. The gain

marked with G_0 is referred to as the zero frequency gain and f_t is the frequency

---

★ The open–loop gain of an amplifier is its gain with no feedback. The feedback capacitor
serves as a source of negative feedback and is removed for this measurement.
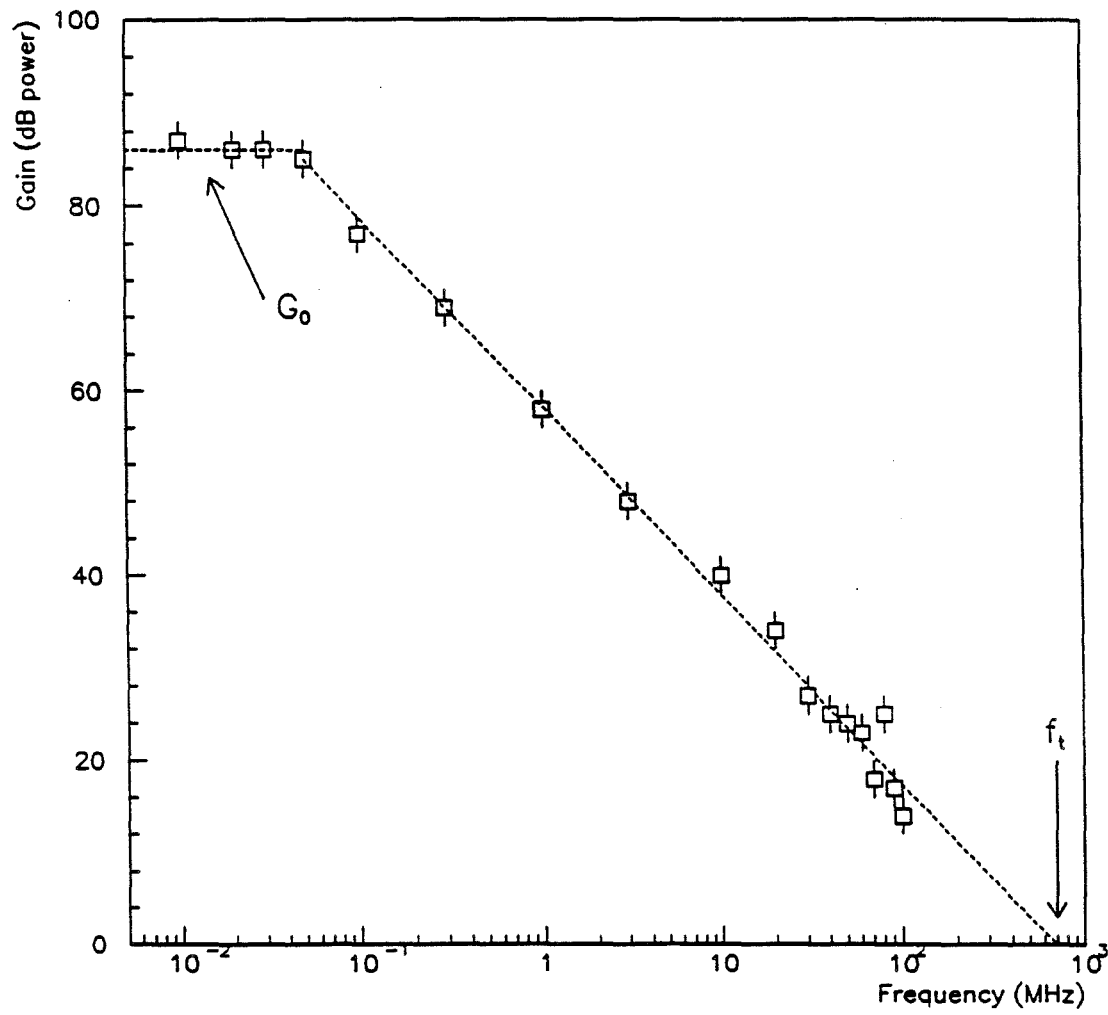
Figure 20   Frequency Performance of LACAMP Amplifier

at which the gain of the amplifier crosses unity – the gain bandwidth product. For frequencies $f_t/G_0 \ll f \ll f_t$ an integrating amplifier can be regarded as a resistor of value

$$R = \frac{1}{2\pi f_t C_{feedback}}.$$ (3.3)

This can be shown if we assume that the gain of the amplifier can be written as

$$G(\omega) = \frac{-G_0}{(1 + i(\frac{\omega}{\omega_t})G_0)},$$ (3.4)

where G_0 is the zero frequency gain, $\omega = 2\pi f$, and $\omega_t = 2\pi f_t$. Then,

$$V_{IN} - V_{OUT} = I_{IN} Z_{feedback}$$

$$V_{OUT} = G(\omega) V_{IN}$$ (3.5)

where $Z_{feedback} = 1/(i\omega C_{feedback})$. The input impedance is then,

$$\frac{V_{IN}}{I_{IN}} = Z_{IN} = \frac{Z_{feedback}}{(1 - G(\omega))}.$$ (3.6)

Assuming $(G_0\omega \gg \omega_t)$ and $\omega_t/\omega \gg 1$ then,

$$Z_{IN} = \frac{1}{\omega_t C_{feedback}} = R_{IN}.$$ (3.7)

This analysis implies a trade off between charge gain and input impedance.

<u>Gain</u>   The ADC in the EWE was used to digitize signals with a full scale of 2.5 Volts. To gain the full advantage of its 16-bit resolution, the amplifier charge gain should be set to have a full scale output of 2.5 Volts. Using 8 pC (the charge

collected in the peak channel for a 300 GeV/c photon) as full scale, then

$$C_{feedback} = \frac{8 \times 10^{-12}\,C}{2.5V} = 4\text{ pF}. \tag{3.8}$$

This value, in conjunction with the previously mentioned constraint on input impedance, implies a gain bandwidth product of $\approx 4\,GHz$. These values were not feasible since high gain bandwidth amplifiers tend to have more noise and problems with oscillation as well as higher cost. Also, low values of the feedback capacitor are difficult to regulate due to component variations and printed circuit board restrictions. A gain bandwidth of 700 MHz and $C_{feedback}$ of 20 pF was chosen as a workable compromise.

The other important gain was the low frequency, open–loop gain (G_0). Charge collected by the calorimeter was shared between the capacitance of the apparatus and the amplifier (an effective capacitance of $G_0 \times C_{feedback}$). After settling, the charge collected on the feedback capacitor was

$$\frac{G_0 \times C_{feedback}}{G_0 \times C_{feedback} + C_{source}.} \tag{3.9}$$

Since the detector capacitance was several nanofarads and the cable capacitance as much as 10 nF, G_0 had to be $\approx 80\,dB$ to collect 90% of the charge.

Noise   Clearly, low noise is a desirable feature for readout electronics since noise directly affects resolution at low energies. Unfortunately, the noise in the output voltage grows with the square root of both detector capacitance and gain bandwidth. For the case where the amplifier feedback capacitor is much smaller than the detector capacitance (as is usually the case on large detectors), the
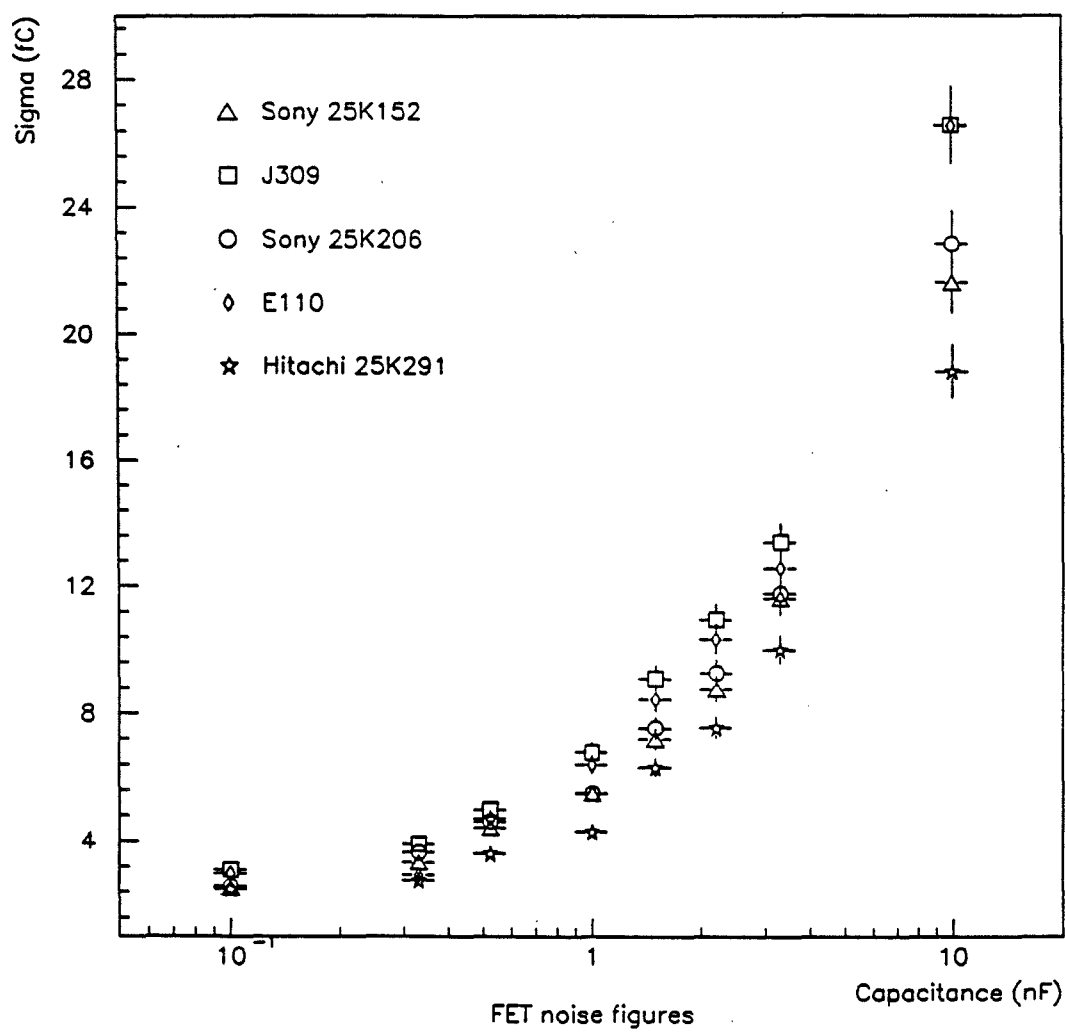
Figure 21   FET Noise Performance

noise voltage from the amplifiers is:[28]

$$V_{rms} = \frac{v_n}{2}\sqrt{\omega_t \frac{C_s + C_f}{C_f}} \qquad (3.10)$$

where,

v_n is the noise figure for the FET (typically $1\,\mathrm{nV}/\sqrt{\mathrm{Hz}}$);

ω_t is the unity gain frequency of the amplifier;

C_s is the source capacitance seen by the FET (This includes detector capacitance, cable capacitance, and gate capacitance of the FET itself.);

C_f is the feedback capacitance of the amplifier.

As shown in the schematic diagram in Appendix A, the primary gain device in the amplifiers was a Field Effect Transistor (FET). Some time during the design stage was spent investigating the performance of several FETs then available.* Figure 21 shows the relative performance of the devices tested. Although there were several FETs available from Japanese vendors that had better noise characteristics, the Siliconix J110 was selected for price and availability reasons.†

Not only was low noise important for reconstruction of low energy electromagnetic showers, it was also important for the spectrometer trigger. The experiment triggered on p_T deposition in the LAC. Analog outputs from as many as 512 channels were summed together.‡ If the amplifier noise was incoherent

---

★ Recently we've found a device from InterFET of Garland, Texas that seems to be a promising replacement for our FET (the NJ3600 and more recently the NJ1600D). Work is in progress by InterFET in collaboration with Manfretti, et al. (Ref. 30) on the development of very long gate FETs for use in High Energy Physics detector applications.

† At the time, trade relations between the U.S. and Japan were strained. Delivery and pricing schedules for electronic components were highly uncertain.

‡ See Section 3.4 for further information about trigger formation.

then the noise on the sum would be $\sqrt{512} \times \sigma_{channel}$. On the other hand, any noise that was coherent amongst the channels added linearly. This could have been disastrous. Experience gained from experiments E629 and E272 showed the value of considering the top of the LAC gantry a Faraday room – shrouding the room with a conductive shell and limiting electrical penetrations to one point.

All data cables entered the enclosure at one point and were either optically or transformer coupled. Power was fed in through isolation transformers at a nearby point. Great care was taken to prevent ground loops and to provide for local current return in all signal paths. In the end, the limiting noise source was a coherent one introduced by the electronics itself. The 400 Hz RABBIT power supplies produced a 2.4 KHz commutation spike from their rectifier diodes. This was picked up, at a very low level, by the amplifiers and fed into the trigger. The trigger was disabled for $30\mu s$ around these spikes introducing a 10% deadtime.

The single channel noise equivalent was 20 fC per channel with detector capacitance and cable attached. This was a full scale signal to noise of 1500:1 (64 dB). The coherent noise mentioned above was approximately three times the statistical one expected in the trigger sum.

Calibration With 15,000 channels of electronics stability and reliability were items of concern. Design of the amplifiers purposefully took advantage of the redundant nature of the RABBIT system. Readout of all channels was possible through both Top and Bottom busses. Each bus had its own independent power supplies and each board could draw power from either bus. The number of components was limited as much as possible to improve both cost and reli-

ability. Within a card, amplifiers were isolated into groups of four amplifiers, with biasing voltages regenerated for each group. This was a natural division arising from the TVCs which will be described later.

Because of readout speed requirements, this redundancy was not fully utilized and the failure of a single EWE disabled the data acquisition system. That the experiment was able to run in this mode speaks well for the reliability of the system. However, frequent repairs were necessary. During the next running period, higher beam intensities are expected requiring limited access to the experimental hall. The redundancy feature should be better used in the future.

Because of the restricted access to the LACAMP modules and the sheer number of channels, an on-board calibrator was provided for remote calibration and testing purposes. The calibrator monitored signals on the backplane from the BAT and was capable of firing one or two current pulses, of equal but programmable amplitude, into one of the 16 amplifiers. The amplifier was selected using the module address and subaddress lines on the Bottom bus. This meant that only one amplifier per crate could be pulsed at a given time. This helped eliminate interference but limited speed and versatility.

A diagram of the calibrator circuitry is shown in Figure 22 and the schematic diagrams can be found in Appendix A. The calibrator charged up a capacitor, C_{inj},[*] to a programmable voltage VCAL. On receipt of the TCAL signal, the switch discharged the capacitor. This induced a current pulse, in the amplifier, of magnitude VCAL $\times$ C_{inj}. Measurements of the amplifier gains over periods of several days were performed and found to be stable to $\approx 0.1\%$.

---

[*] We used a calibration capacitor of the same type and size as the feedback capacitors to duplicate any temperature or dielectric adsorption effects.
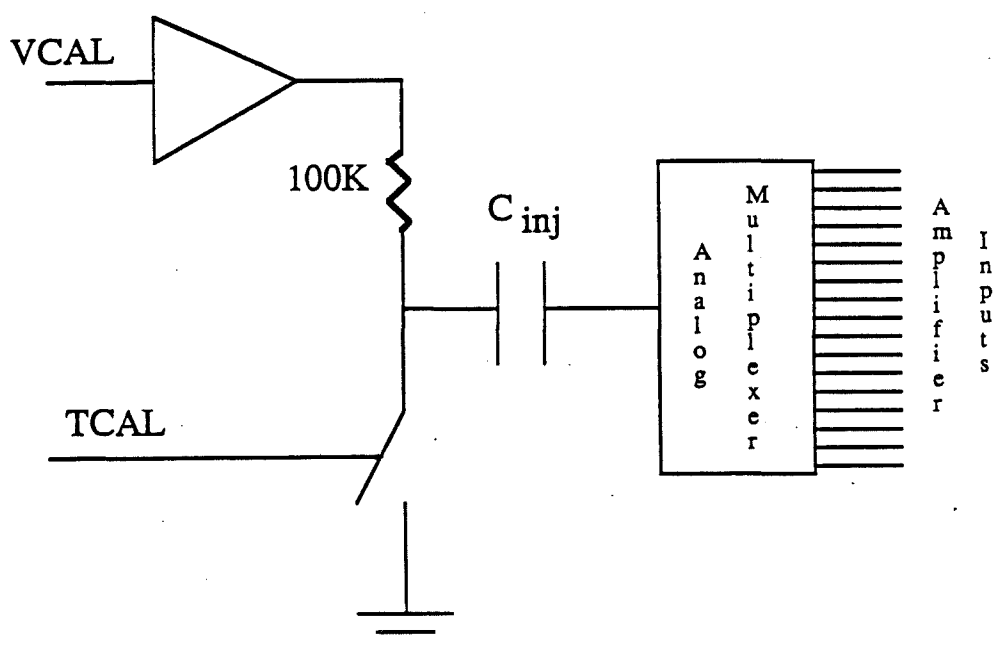
Figure 22   LACAMP Calibrator Functional Diagram

Figure 22 is a simplification in that there were actually two injection capacitors that could be discharged independently. Timing between the two pulses was programmable as shown in Figure 17. By adjusting the timing between these two pulses and the BEFORE pulse, one could calibrate both master and slave TVCs, as will be discussed in section 3.4.6.

<u>Fast Outputs and Trigger Response</u> The 800 ns delay line, shown in Figure 19, allowed time for the trigger logic to determine if a trigger had been satisfied. If so, the BAT was sent a front panel EVENT signal, instructing it to generate BEFORE and AFTER signals on the RABBIT backplane. The sample and hold section of the LACAMP, shown in Figure 19, opened a switch to a separate 1 nF capacitor on receipt of BEFORE and AFTER. Normally these switches were closed and the voltage on the two capacitors tracked the delayed amplifier output shown in Figure 14(c). When the switch was opened, the delayed output voltage was sampled, and stored on the capacitor – hence the name "sample and hold".

The delays in the BAT and trigger logic were set so that the BEFORE signal arrived at the switch about 80 ns before the LAC signal. The AFTER arrived 640 ns after BEFORE. Sampling the amplifier output at two close times minimized the sensitivity to slow variations of amplifier output (e.g. 60 Hz & 400 Hz oscillations from power supplies). Another advantage to this method can be seen in Figure 14. The amplifier output for the second LAC current pulse rides on top of the first since the decay time of the amplifier pulse is quite long (60 μs RC). Thus the baseline for the second pulse is not the same as the first. A dual sampling method minimizes this problem by measuring the baseline value for each pulse.

As shown in Figure 19, the fast trigger output was derived from the difference of the amplifier output and a delayed copy from the tap (180 ns delay) of the delay line. This procedure is known as *delay line differentiation*. The result was a unipolar pulse of ≈ 200 ns risetime and 500 ns duration as shown in Figure 14. Attenuation at the tap of the delay line was measure to be $\approx 1\%$ and was uncompensated.

The fast outputs routed the delay line differentiated signals to a single multipin connector on the front panel of the LACAMP module. These were connected to the LAC trigger electronics with a shielded ribbon cable.

Timing   Timing information was provided through on-board TVCs. Their function was to produce a voltage, V_{time}, proportional to the time between the beginning of a LAC pulse and the BEFORE pulse.[*]

Figure 23 shows a block diagram of the TVC circuitry. The outputs of four amplifier channels, differentiated and amplified, were sent differentially, to reduce the effect of pickup noise, across the board to a discriminator which compared the signal to a threshold level. This comparison is shown as the first stage of Figure 23. The threshold level was programmable and set by the BAT. When the signal crossed threshold the discriminator clocked a flip–flop into the SET state. This blocked the current flow into the gate, causing charge to build up on the 1 nF capacitor. If a trigger occurred before the voltage on the capacitor reached a level sufficient to reset the flip–flop, the current was diverted from the capacitor into the BEFORE generator and the voltage stored on the capacitor was

---

[*] The logic works because the sum of signals used for the TVCs was produced directly from the outputs of the four amplifiers. They did not traverse the delay line before making the sum.

Figure 23   Functional Diagram of Time to Voltage Converters

proportional to the time between when the signal crossed threshold and arrival of BEFORE.[†] This is the situation shown in Figure 14(e). Otherwise, as shown in Figure 23, the flip–flop was reset, draining the charge off the capacitor.

The full scale time of the TVC was determined by fixing the value of the capacitor and the current flowing into it. A $1.5\,\mu$s ramp was selected to accommodate the 800 ns delay line and time pulses arriving before or after the pulse of interest. This ramp was long enough so that there was a fair probability[*] that a second pulse would arrive during the time the capacitor was ramping up. To avoid that dead time, a *master/slave*, two-hit capability was incorporated. As shown in Figure 23, a second ramping circuit was tied to the first and enabled when the first was set. Losing timing information due to TVC deadtime,[†] therefore, required three pulses within the cycle time of a ramp (1.7μs).

Table 8 lists the subaddress assignments for the LACAMP module. The redundancy in the TVC addressing is an artifact of hardware simplifications in the address decoding scheme. Please refer to the LACAMP schematics in Appendix A for details.

Construction   The LACAMP module was designed by Tom Droege and Charlie Nelson of PIG and Eric Prebys and the author from the University of Rochester. The modules were assembled by Paraplegics, Inc. of Bensenville, Illinois and debugged by a team of five temporary technicians under the author's supervision. Test stations for checking the functionality and debugging problems with the

---

[†] Since the risetime of the pulse out of the LAC is ≈ 350 ns (10–90%), the timing information needs to be corrected for pulse slewing.

[*] For an interaction rate of 1×10^6 Hz the probability is $\approx 14\%$ for the inner region of the LAC. For regions at greater R the probability decreases.

[†] This has $\leq 2\%$ probability for the above conditions.

LACAMP Subaddress Assignment	
Subaddress	Output
SA 0 – 15	Amplifier 0 – 15
SA 16 or SA 20	TVC 0–3 master
SA 17 or SA 21	TVC 0–3 slave
SA 18 or SA 22	TVC 4–7 master
SA 19 or SA 23	TVC 4–7 slave
SA 24 or SA 28	TVC 8–11 master
SA 25 or SA 29	TVC 8–11 slave
SA 26 or SA 30	TVC 12–15 master
SA 27 or SA 31	TVC 12–15 slave

Table 8   LACAMP Subaddress Assignments

modules were built using IBM PCs as controlling computers. Diagnostic software was written to exercise all the functions of the modules and to aid in diagnosing faulty boards. The configuration that proved most effective was for two technicians to provide visual inspection and DC power measurements at key positions on the board, with the other three technicians performing tests on the active performance of the module's components. On average, 10 boards a day could be processed in this fashion.

Once the modules were installed in the Faraday room, there was a rather high level of failure soon after installation (10%). This "infant mortality" problem was found to be greatly reduced by leaving the modules powered on overnight, at an elevated temperature (60° C), after the first stage checkout mentioned above. This procedure is highly recommended for future use.

3.5 LAC Trigger Electronics

The RABBIT system was also used for the trigger modules that generated the trigger p_T signals described in Section 3.3. These modules took the fast output signals from the LACAMP modules and performed an analog sum. The signals were weighted by the sine of the angle their corresponding strips made with the beam axis. These p_T sums were then compared against local and global thresholds to generate the trigger signals.

To generate the sums, the LACAMP fast output signals were sent to a module known as the "p_T adder" via six foot lengths of shielded 34 conductor ribbon cable. This adder module had 32 input channels and produced "sum-of-8" and "sum-of-32" outputs. At the inputs, neighboring two channels were immediately added then sent to an "attenuator" device. This attenuator was really an AD7528 DAC. The sum was connected to the VOUT pin of the DAC and a level equal to $\alpha(\frac{x}{255})V_{sum}$ was available at the VREF pin of the DAC. The attenuation factor $\alpha(\frac{x}{255})$ had two parts: x was the value programmed into the DAC and could be varied from 0 to 255. α was a flat attenuation of $1/100$ due to the internal resistor of the DAC.

This attenuation stage was immediately followed by a gain stage using a 733 video amplifier. Its gain was set to $1/\alpha$, so that the overall gain of the system was unity. After this, two levels of summing by fours were performed to produce the sum-of-8 and sum-of-32 outputs.

After this point, the path for the global and local sums diverged. The local sum was generated from the sum-of-8 signals by the "discriminator" module. This was a double width RABBIT module, also produced by the University of

Rochester, whose function was to use the sum-of-8 signals from the p_T adder to produce overlapping sum-of-16[*] and discriminate the result against a computer controllable threshold. Since two different thresholds for local p_T trigger signals were desired, the inputs of this discriminator module were made high impedant so that more than one module could be daisy-chained on the same cable. The logical "OR" of all discriminated sum-of-16s was used to generate the LCLPTHI and LCLPTLO signals.

The global trigger signals were to be generated by feeding the sum-of-32 outputs from the first level p_T adder into a second adder module. This module produced the global sum that was sent to the trigger system. During the run this method was found not to work due to the large amount of "wrong sign" signal due to image charge in the detector. The problem of image charge was due to construction details of the EMLAC. When charge was deposited in the LAC and began to drift to a particular readout strip, an image pulse was induced on the lead plate. There were ballast capacitors attached to each high voltage plate to act as local power supplies and provide current for this pulse to the plate. Unfortunately, the capacitive coupling to all the other amplifiers provided a lower impedant path and current was drawn out of the other strips' amplifiers. This caused signals, of opposite sign from normal LAC signals, to be produced by the amplifiers. This effect was temporary, lasting a couple hundred nanoseconds until the ballast capacitors were able to provide the charge to the plates, and was a small effect on any individual channel. However, for fast trigger signals, especially the global sum where such coherent effects were magnified, it was a

---

[*] The overlapping sums of 16 were necessary to avoid situations were the p_T of a shower could be split between two different groups of 16 strips.

serious problem.[24]

This wrong sign signal was reduced by feeding the sum-of-32 signals into high speed NIM photomultiplier amplifiers with a gain of 10 and using a modified p_T adder to perform the final sum. This adder was modified to use a diode to cutoff the positive going or "wrong-sign" pulses at the input stage. This was fairly successful in eliminating image charge contributions from sections of the calorimeter in which there was no p_T deposition but could not eliminate the problem entirely. Even with this solution applied, the outermost 16 strips of the EMLAC were removed from the trigger. Since these radial strips were at the largest radius, they had the largest area and hence best coupling to the lead plate.

3.6 COLD START TASKS

At the beginning of each run, the operator had the option of performing *cold start*, or initialization, routines, as discussed in the opening section of this chapter. This section discusses the various tasks performed in the LAC cold start sequences.

<u>MX initialization</u> The first task, performed at every cold start, was to reload the MX instruction memory with a fresh copy of the data acquisition program. The results of this download were checked against a copy of the program kept on the PDP to insure accurate transmission and the program was written to an archival database for future reference.

<u>Pedestals</u> The other task performed at every cold start was the collection of pedestal values for each amplifier. These values were also stored in a database

for use in the reconstruction program. The discussion of pedestals can be rather confusing as there were two pedestals in the system – one for use in the zero suppression scheme discussed in Section 3.3.5 and the other for use in the re-construction program.

The cold start procedure determined the value of both pedestals using the following procedure. First, the center of the TOT threshold window was found. This was done by selecting Ground – Ground on the analog multiplexer of the EWE with a nominally zero offset in the pedestal DAC. A TOT was performed and the pedestal DAC setting was raised and lowered to find the limits of the TOT threshold.[*] Once the limits of the window were determined, the pedestal DAC was set to the middle of the TOT window. 32 measurements of the ADC were then made. The mean of these readings was declared *GROUND* for that EWE and all further adjustments made with reference to that value.[†]

The next stage of the procedure was to select each channel in turn using the "centered" value of the pedestal DAC found in the previous step. Again, 32 measurements of the ADC were made. From the difference between the resulting value and the *GROUND* value an adjustment to the pedestal setting was made and stored. This adjustment was different for each channel because of different offset voltages in each channel. Once all the channels had been tested, they were again selected in turn and the process repeated. This time, the pedestal DAC setting was the one stored from the first iteration. The number of samples

---

[*] If the starting value satisfied the TOT then the pedestal DAC was adjusted in coarse steps to find a starting point inside the TOT window.

[†] The reason for this procedure was the large amount of gain in the TOT circuit and the variations with time of the offset voltages in the op amps used in this circuit. It was found to be impractical to keep 100 EWEs adjusted so that the same pedestal DAC setting corresponded to the center of the TOT window in each EWE.

of the ADC was much higher (128) for this iteration to minimize the effects of amplifier noise on the calculation of the mean. The results were used to make finer corrections to the pedestal DAC setting.

Once the second iteration was completed, a third loop was performed – again with 128 ADC samples. This time, the mean was recorded in a database for use as the reconstruction pedestal. In principle, this value should be the same for all channels, but was found to vary slightly from channel to channel.[‡]

Gains The preceeding two tasks took $\approx$ 3 minutes to complete for the entire LAC system. A third task was performed every 8 hour shift. This task measured the gain of each amplifier channel and calibrated each TVC channel. This took $\approx$ 10 minutes to perform and so was too slow to perform every cold start.

The gains were measured using the on-board calibrator on each of the LACAMP modules. Appendix A shows the schematic diagram for the calibrator section of the LACAMP. A known charge pulse was produced by charging up a capacitor with a regulated, programmable voltage supply and discharging the capacitor into each of the amplifiers. The resulting curve for amplifier output versus charge injected was used to calculate the gain of individual channels.[§]

The TVCs were calibrated using the on-board calibrator as well. For this purpose, the calibrator was designed to produce two pulses with programmable

---

‡ It has subsequently been found that the pedestal value obtained by this method differs from the value seen in the data. For most channels there is a constant shift of about 6 ADC counts. This is likely to be due to background energy in the LAC. The first channels in a crate differ by as many as 80 ADC counts. As of yet, the cause of this large discrepancy is not understood.

§ The biggest uncertainty in the measurement of amplifier gain is in the value of the charge injection capacitor. In principle, this can be measured for each LACAMP but this was not done during the 1987-8 running period. The method used to minimize the effect of this uncertainty will be described in the following chapter.

separation. The time between the first pulse and the arrival of the BEFORE pulse was proportional to the voltage output from the master TVC. The time between the second pulse and the BEFORE was measured by the "slave" TVC. By varying the arrival time of the BEFORE pulse, the ramp of the TVCs could be calibrated. This method gave a good value for the slope of the TVC ramp, but did not yield an accurate value for the "zero time". The zero time was the time between an interacting event and the BEFORE in the data taking environment. Since the BEFORE was generated by different methods in CALIBRATION and EVENT cycles, the relationship was not easily measured. The data was used to find a zero time for each TVC by plotting the number of events with a given TVC result. The peak determined the zero time.

4. Reconstruction

This chapter discusses the process of reconstructing physics quantities from the data accumulated during the run. Since the analysis programs consisted of some 100,000 lines of FORTRAN code, detailed discussion of the software is restricted to those portions contributed by the author and code relevant to the topic of η production.

4.1 *MAGIC*

The master program for data reconstruction was called *MAGIC*.[*] *MAGIC* managed the data analysis and all formatting necessary to make data available to the individual reconstructors. This included: reading data from tapes and databases, memory management, error reporting and diagnostic information, as well as writing the results to the selected output device. The logical flow of *MAGIC* can be seen in the following outline:

BeginJob – Here the initialization routines were performed: allocate working space in memory, setup the output and input streams, book histograms, ...

BeginRun – Here code that needed to be executed once per run was performed. Typical tasks were: retrieve information from run databases (*e.g.* alignment, pedestals), check for "bad" runs, ...

BeginSpill – An opportunity existed to execute code before processing the first event recorded in a spill. This level of data selection was not used.

★ *MAGIC* was written primarily by George Alverson and Ed Pothier of Northeastern University.

DoEvent – At this level the reconstructors were called, one for each section of the spectrometer: Cherenkov and Trigger, Tracking, EMLAC, HALAC, Forward Calorimeter. This was where the event pattern recognition algorithms were executed. Each reconstructor was independent and was not allowed to use results from other reconstructors.

EndSpill – An opportunity existed to execute code after processing the last event recorded during a spill.

EndRun – Code used to collect information for each run was executed at this level. This opportunity was used to fill diagnostic histograms, etc.

EndJob – This level contained the final tasks of the program: write out any results, release allocated resources, interpret errors, etc.

MAGIC was developed to allow its use on several different types of computers, since it was unclear what type of machines would be available to do the production computing.[†] To date, *MAGIC* has been run successfully on DEC VAX, Fermilab Advanced Computing Project (ACP), and AMDAHL computers. Adherence to strict FORTRAN 77 and code management using *PATCHY* from CERN made the maintenance this code possible.[31]

Code development work was done on VAX computers with the resulting code

---

† At the time *MAGIC* was being structured, the Fermilab Computing Department had made no decision about its computer upgrade. Since E706 was committed to using computing resources centered at Fermilab, code was made a general as possible.

Input Tape

μVAX

Output Tape

node
1

node
2

node
n - 2

node
n - 1

node
n
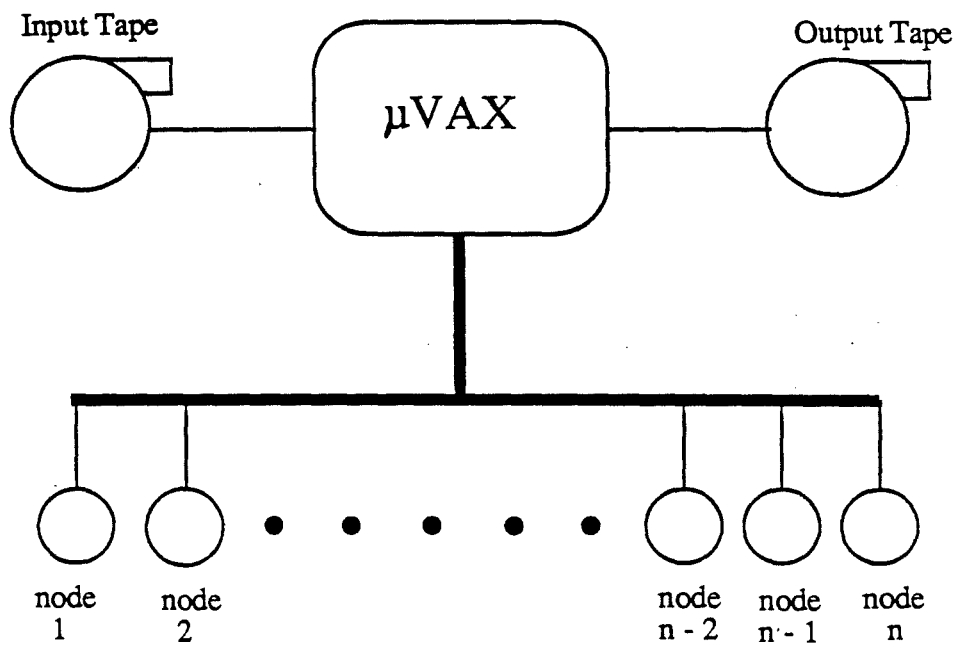
Figure 24   Block Diagram of ACP Computing System

converted to run on the ACP system.[‡] The production run of 500 data tapes used the ACP system. The ACP system was a parallel computing system using a "farm" of microprocessors controlled by a μVAX workstation. The version of the ACP used for the production analysis had a μVAX III as the host and Motorola 68020 microprocessors, with 68882 math coprocessors, on the nodes. A block diagram of the system is shown in Figure 24.

The μVAX read events from an input tape of raw data and distributed them amongst the available ACP nodes, one event per node. Each node was an independent microcomputer with its own local memory and program. Once an event was loaded into a node, the node required no action from the host until the program had completed. Since the same analysis code was run on millions of individual events, this type of parallel computing was particularly well suited to event reconstruction.[32]

This thesis uses results from the trigger, Cherenkov, tracking, and EMLAC reconstructors. The following sections provide a description of each of those reconstructors.

4.2 TRIGGER AND CHERENKOV

Information from the trigger logic and Cherenkov detector was reconstructed using a program called *DLREC* (for Discrete Logic REConstructor). Trigger reconstruction consisted of reading the values of several scalers that were used to count beam particles, interactions, and several other internal stages to the trigger. These could then be tested for consistency, to determine when problems

---

‡   Code for the ACP was developed mostly by Jim Dunlea, Amit Jain, Vijay Kapoor, and Brajesh Choudhary.

occurred with the trigger logic. The hits[*] in the veto wall for seven beam buckets before and after the interaction of interest were stored in latches. These hits were then reconstructed to determine if the area covering the trigger quadrant of the LAC saw the passage of a charged particle. The other crucial quantity from the trigger system was the number of beam particles on which the experiment could have triggered. This quantity, LIVE_TRIGGERABLE_BEAM, was used for cross section normalizations.

Since E706 was in a secondary beamline, the beam consisted of more than one type of particle. The Cherenkov detector was set to tag the second most populous beam particle type. The obvious definition of six hits in the coincidence phototubes and none in the anti-coincidence phototubes was not useful due to low light output and accidental hits in the anti channels. There were several combinations made of signals in the six coincidence phototubes and six anti-coincident phototubes. For example, the combination D4$\overline{V2}$ was set for those events that had 4 or more hits in the coincidence tubes and 2 or fewer in the "anti" tubes. Different logic definitions were used for different purposes, usually trading efficiency for contamination. D5$\overline{V2}$ would be very effective at selecting events with a minority particle but would have rather bad efficiency. D3$\overline{V3}$ would have much better efficiency but a larger contamination from the majority particle. For the negative beam data, D4$\overline{V2}$ was used to tag the K^- and in the positive beam data D3$\overline{V2}$ was used to tag the π^+.

---

[*] The term "hit" is used to describe a signal for which a binary decision has been made — was the signal above a certain threshold or not. A signal above threshold is called a hit.

4.3 Track Reconstruction

Signals from the tracking section of the spectrometer, the PWCs and SSDs, were reconstructed using *PLREC* (for **PL**anes **REC**onstructor). *PLREC* used hits on the wires (strips) of the various planes of PWCs (SSDs) to reconstruct particle trajectories or "tracks" through the detectors. The resulting tracks from each system were projected to the center of the analysis magnet and matched with tracks from the other system. Using the magnetic field and the angle between the track upstream and downstream of the magnet, the momentum and sign of the charged particle were calculated.

The three pairs of silicon detectors upstream of the target were used to track the incoming beam particle. Tracks in these detectors were analyzed to determine the incident angle of the incoming beam particle and the presence of multiple beam tracks. The hits in the detector were sorted to find three-hit tracks.[*] These hits were then removed from the pool and the remainder used to form two-hit tracks. The vertex position, calculated using the downstream silicon detectors, was used to sort out the possible beam tracks.

In the four downstream pairs of silicon detectors, tracks were again formed in the two orthogonal views. Tracking proceeded in each view by making tracks from a hit in the plane furthest upstream with a hit in the most downstream plane and then searching the two inner planes for hits along this path. This method found the four-hit tracks and those three-hit tracks where the missing

---

[*] For detectors having 100% efficiency one would expect to find a hit in every detector traversed. Since real detectors are not 100% efficient, one generally accepts tracks made from fewer hits than the number of available detectors. This leads to thee terminology of "n-hit tracks" where n is the number of hits used in forming the track.

hit was in one of the inner planes. The roles of the inner and outer pairs were then reversed and tracks formed again. This pass found the three-hit tracks where the missing hit was in one of the outer planes.

The tracks formed by this method were projected to the target region and a vertex formed.[†] The tracks were then discarded one at a time, sorting by their *impact parameter* at the nominal vertex, until an acceptable fit was found or only two tracks remained. The impact parameter was the distance from the nominal vertex position to the track projection; in the X view this would be the distance (in X) from the nominal vertex position, to the X position of the track projection. Once a vertex was found in each view, the result was used as a seed for the other view, and the vertex recalculated. The resulting resolution for this system was $600\,\mu$m along the beam direction (Z) and $20\,\mu$m transverse to the beam.[33]

In the PWCs, there were four planes in each of four views. The four views were divided into two pairs of orthogonal views. Tracks were constructed in each of the views by the method described for the downstream silicon detectors. Then the tracks from the X and Y planes were projected onto the U and V planes (and visa versa) to resolve ambiguities. The resulting "space tracks" were projected back to the center of the magnet and matched with projected SSD tracks. For use in this analysis, the results of *PLREC* were used to select events with a vertex in the target volume.

---

† Four-hit tracks were used to form the vertex if there were more than four such tracks, otherwise three-hit tracks were also considered.

4.4 Electromagnetic Reconstruction

EMREC, the reconstructor for the EMLAC, used the ADC values assigned to the various strips in the EMLAC to reconstruct photon energies and positions.

The first step of this process was to subtract pedestals from the ADC data and convert the ADC counts to energy. The pedestals were gathered during the cold start procedures mentioned in Section 3.1. Results from that procedure were retrieved from the run constants database and subtracted from the ADC data. This pedestal subtracted value was converted to energy using gains stored in the same database.

<u>Gains</u> The gains stored were the results of fits to the curve of ADC output versus charge injected by the LACAMP calibrator. These two parameters were related by the following expression:

$$ADC = \underbrace{VCAL \times G_{DAC} \times C_{inj}}_{Q_{inj}} \times G_{amp} \times F_a \times G_{ADC} \tag{4.1}$$

where,

$VCAL$ was the setting of the BAT's VCAL DAC;

G_{DAC} was the conversion of bit to volts for the DAC;

C_{inj} was the value of the charge injection capacitance;

G_{amp} was the charge gain of each amplifier channel;

F_a was the charge fraction collected for each amplifier;

G_{ADC} was the conversion of volts to bits for the ADC.

This compares with the following expression relating ADC value to charge deposited in the LAC:

$$ADC = Q \times G_{amp} \times F_c \times G_{ADC} \qquad (4.2)$$

where,

Q was the amount of charge deposited in the LAC;

G_{amp} was the charge gain of each amplifier channel;

F_c was the charge fraction collected for each amplifier;

G_{ADC} was the conversion of volts to bits for the ADC.

The charge fraction was a function of the sampling time. For short time scales, the two cases need not be the same. The calibrator injected charge, with an exponential current pulse, at the input of the amplifier; the LAC had a linear current pulse, at the far end of the Gore cable. Simulations of the LAC detector and amplifier, using the program *SPICE* from the University of California,[34] indicate that the differences between F_c and F_a for times $\geq 600\,\text{ns}$ were $\leq 1\,\%$. The dominant uncertainty in the calibrator gain was the value of the charge injection capacitor. These capacitors were measured during LACAMP assembly and found to have a Gaussian distribution with 2.5 % sigma.

Using this information, it was decided to normalize the calibration results by the average of the gains within each module. Since the first three terms and the last term of equation (4.1) were constant for a given module they cancelled in the ratio. Also, the charge sharing fractions were nearly constant within a given module. The resulting ratio of amplifier gain to card average of amplifier

gain was equivalent to the ratio of feedback capacitor to card average of feedback capacitor. Since this capacitor was of the same batch used for the charge injection capacitor, the card average should vary by $2.5\%/\sqrt{16}$.

Equation (4.2) was approximated in the reconstruction algorithm by

$$\frac{G_{amp}}{<G_{amp}>_{card}} \times <G_{amp}>_{allcards} \times <G_{ADC}> \times F(C_D, t) \qquad (4.3)$$

where,

$\frac{G_{amp}}{<G_{amp}>_{card}}$ was the ratio determined above;

$<G_{amp}>_{all\ cards}$ was the average gain of a LAC channel;

$<G_{ADC}>$ was average gain of the EWE ADCs;

$F(C_D, t)$ was the function used for the charge fraction collected.

$F(C_D, t)$ was given by

$$F = \left(\frac{G_0 C_F}{G_0 C_F + C_D}\right) \left(1 - exp\left(\frac{-t}{\sqrt{((RC_D)^2 + \tau_{elec}^2}}\right)\right) \qquad (4.4)$$

where,

C_F was the feedback capacitor;

C_D was the detector capacitance;

R was the impedance of the readout system;

τ_{elec} was the risetime of the LACAMPs.

t was the pulse sampling time.
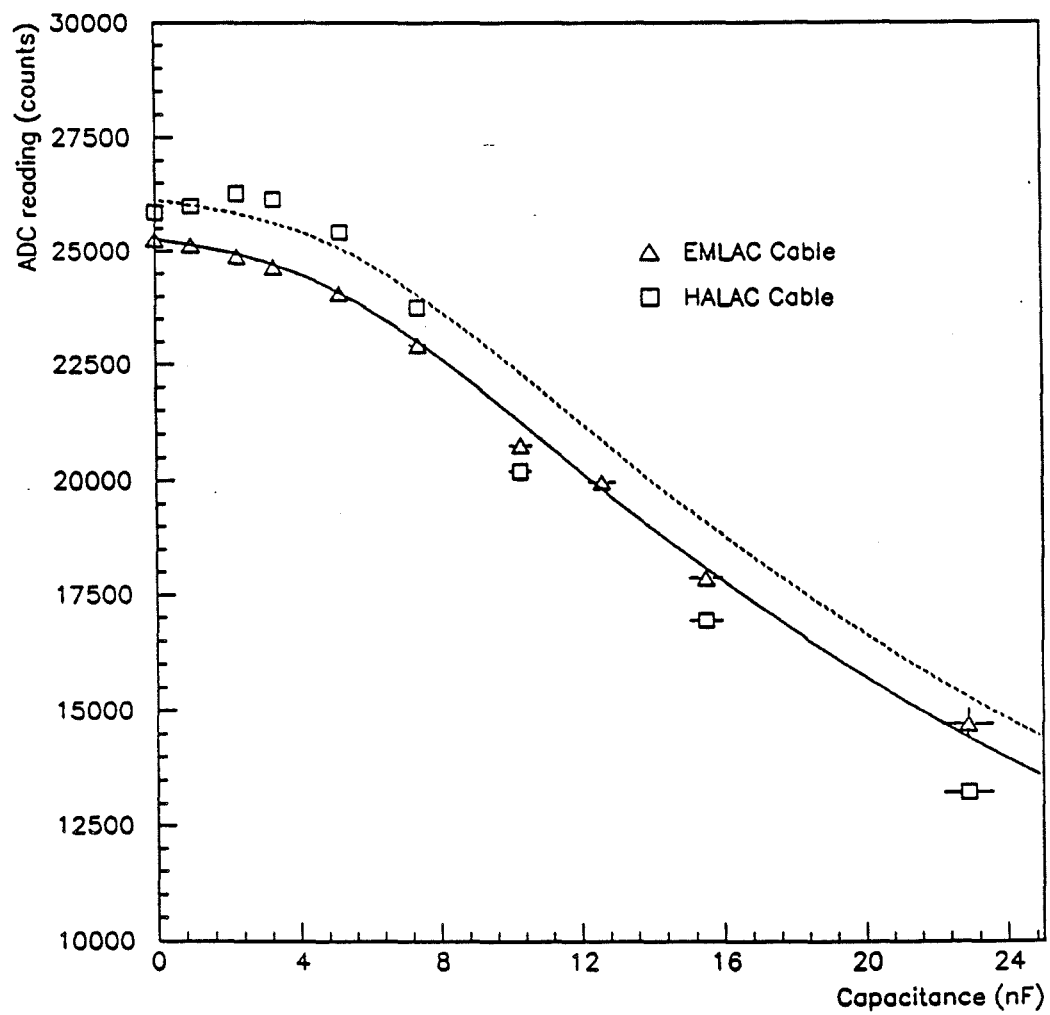
Figure 25   LAC Amplifier Charge vs. Detector Capacitance

This expression accounted for effects due to charge sharing between the detector and amplifier capacitances as well as risetime of the LAC signal. The parameters of this equation were determined by fitting results measured on a test system. In this test, charge was deposited on the "detector" end of a Gore cable and the detector simulated by bulk capacitors of various values. Data from this test are shown in Figure 25. The fit for the EMLAC cable is quite good for all values of detector capacitance. The HALAC cable fit is satisfactory for detector capacitances below 7 nF, but disagrees above that. For use in this analysis, this discrepancy is unimportant because the EMLAC has ≤ 5 nF for all channels using the HALAC cable.

Octant Energy Scales								
Octant	1	2	3	4	5	6	7	8
MeV/count	2.98	2.96	3.09	3.03	2.91	2.91	2.99	2.90

Table 9   Energy Conversion Constants for LAC Octants

Once the charge equivalence was determined, it was converted into energy incident on the LAC by requiring the average π° mass in each octant to be $135 \, \text{MeV}/c^2$. This conversion factor was different for each octant due to differences in construction and operation (*e.g.* different HV levels, different lead thicknesses). The values used are listed in Table 9.

Photon Reconstruction   Once the strip readings had been converted to energy values, there was a correction made for single dead channels. These were channels where there was energy in both neighboring strips but none in the one channel. In this case, the empty strip was assigned the average energy of the

two neighbors. This was done to prevent single dead channels from destroying the pattern recognition algorithms.

Using these strip energies, each view was searched for clusters of energy. *EMREC* divided each quadrant of the EMLAC into four views: left R, right R, inner ϕ, and outer ϕ.[*] The division into left and right R derived from construction details of the EMLAC. Since the EMLAC was constructed in modules of quadrant size that was the relevant unit for the reconstructor because information from both octants could be used to reconstruct photons which landing near the boundary between the two octants in a quadrant. Octant boundaries that coincided with quadrant boundaries were broad enough to preclude using information from both sides.

Each view was searched for clusters of contiguous strips with energies above a threshold of 150 MeV. These "groups" were then subjected to the following selection criteria:

- The total group energy must be above 750 MeV;

- The energy in the most energetic strip must exceed 300 MeV;

- For both R views and inner ϕ, the group must span at least three strips. (The outer ϕ was only required to have two strips since the strips became wider at large radius.)

The surviving groups were searched for peaks and the peaks were assigned to *gammas*.[†] This process was done for both R and ϕ views.

---

[*] The R/ϕ and inner/outer ϕ divisions were natural from the construction of the readout board as described in Chapter 2.

[†] The term *gamma* refers to a single shower in one view.

R View
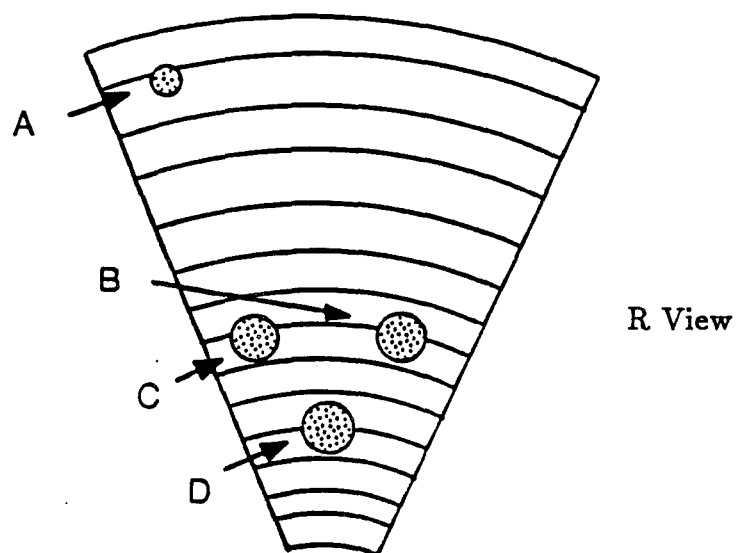
Two photons (B, C) overlap in R

ϕ View
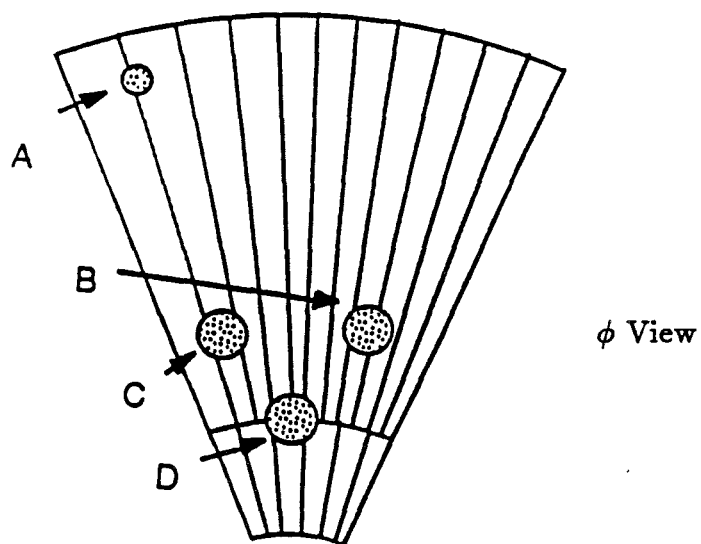
Photons A and C overlap in ϕ. Photon D is split between inner and outer ϕ.

Figure 26   Photon Position and Overlapping Showers.

After the gammas were determined, they needed to be correlated. If there was only one photon in a half-octant, the problem was simple, but with π°, η, and other multi-photon events, the problem was much harder. The latter situation is shown in Figure 26. In Figure 26(a), the R view, two photons overlap: B and C. Figure 26(b) shows the same distribution from the other, ϕ, view. In this view, photons B and C are clearly resolved, but photons A and C overlap. The algorithm now has to untangle information from three photons to correlate B and C correctly.[‡]

The R strips determined radial position, but had no information about ϕ (other than octant). The ϕ strips did give some indication of radial position. This could be extracted by using the width of the shower. Since the ϕ strips were constant angle they widened with increasing radius; showers at large R covered fewer strips, and appeared to be narrower. This method was not terribly accurate, but it gave a starting guess for correlation. From this stage, the correlations were done by using the energies in the two views and the fraction of charge deposited in the front and back sections of the calorimeter.

In some cases, it was not possible for the algorithm to make the correct correlation and this constitutes an inefficiency in the program. Corrections for this effect and other losses will be discussed in the following chapter.

---

‡ The detailed description of the correlation algorithm can be found in Ref. 22.

5. Data Analysis

The results of the data reconstruction, as described in the preceeding chapter, were used to search for π° and η mesons in the $\gamma\gamma$ decay mode. This chapter details the procedures followed during the analysis, as well as the results of that effort.

Set	Beam	Target	Run Number	Date	Triggers
A	Neg	Cu + Be	2852–3036	Feb 9–13	786K
B	Pos	Cu + Be	2588–2670	Jan 30–Feb 1	440K
C	Pos	Cu + Be	2387–2586	Jan 26–30	1,225K
D	Neg	Be	2062–2382	Jan 16–25	1,247K
E	Pos	Be	1728–2007	Jan 4–13	1,508K

Table 10   Data Sets from 1988 Running Period.

5.1 DATA SELECTION

The data collected during the 1987–8 running period was divided into several sets of runs as seen in Table 10. These sets designate major changes in running conditions (*e.g.* changes in beam polarity) and are numbered in reverse chronological order As this was the initial run of E706, the quality of the data increased substantially in the latter runs. Runs earlier than set E have significant experimental differences and difficulties, and have been ignored for this analysis. Two sets of runs, A and D, are used in this analysis for negative beam and sets C and E, are used for positive. Table 10 lists the initial and final run numbers for each set and their associated dates. The last column of Table 10

lists the number of trigger recorded for each set. Set B was not used in this analysis because the tracking system was compromised due to the loss of one PWC chamber.

Effect of Event Cuts	Set A	Set C	Set D	Set E
Number of Triggers	786,000	1,225,000	1,247,000	1,508,000
Events Processed	771,700	1,196,600	1,120,900	928,150
$p_T >$ PTCUT	314,781	196,646	162,554	146,007
Veto Wall Cut	188,632	46,505	57,595	37,611
Vertex Cut	147,230	37,293	46,643	25,847

Table 11   Effects of Event Cuts

Event Selection   Table 11 details the effects of various event selection criterion. The subset of runs used excluded runs with fewer than 500 events[*] and runs with abnormal behavior in one of the major spectrometer elements. The effect of this selection is shown in the second line of Table 11.

Several quantities were monitored to determine the status of subsections of the spectrometer. For example, Figure 27 shows the fraction of events in which a vertex was found in the target volume. These *stability* plots were examined for each set of runs and relevant corrections for each set were determined. Within a set, runs that deviated drastically from the norm were eliminated from the data sample. Table 11 shows that this selection criterion did not eliminate a large fraction of the data for most sets of runs. Set E lost a good fraction of its data

---

[*] These runs were ones that ended abnormally due to a failure somewhere in the system. Typically this was due to loss of beam from the accelerator or a failure to properly start the data acquisition software.
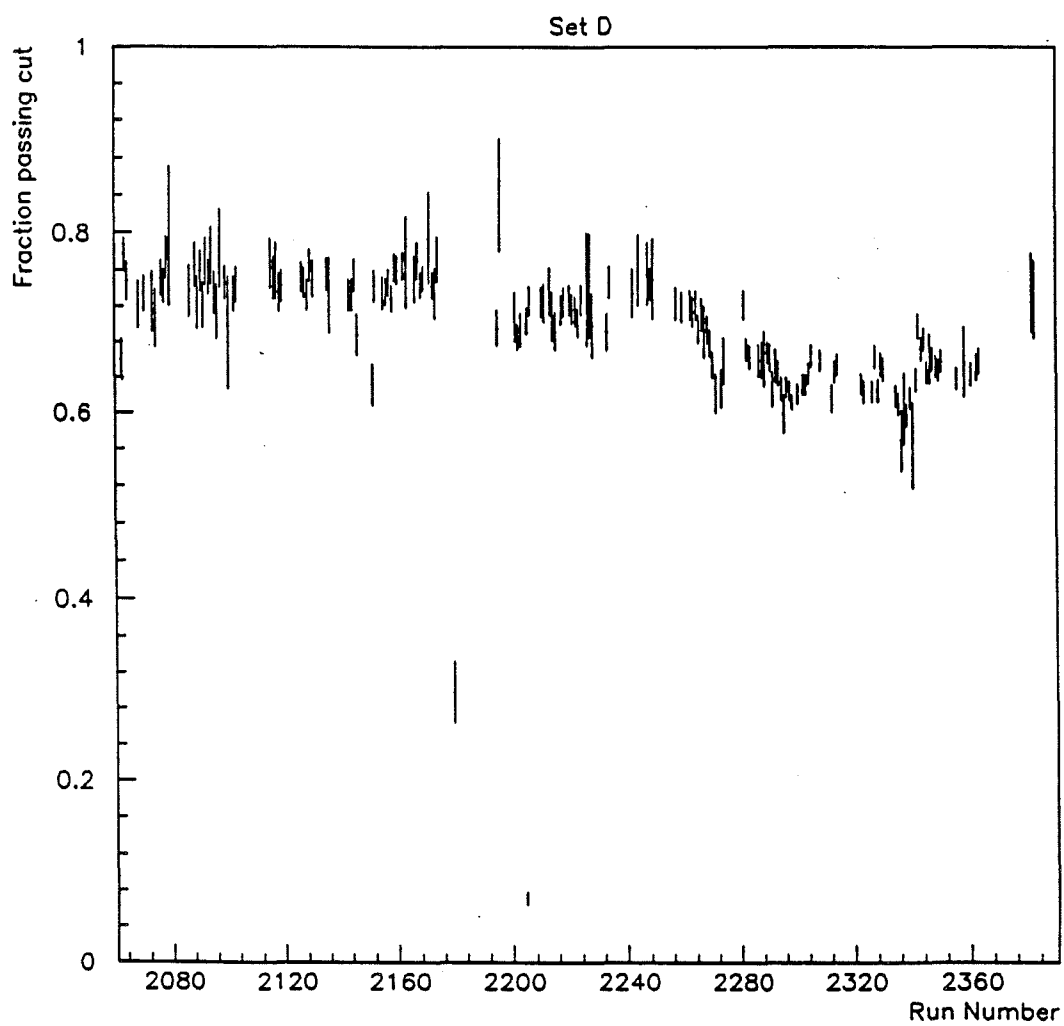
Figure 27   Event Fraction With Vertices Found in Target

due to the fact that the *Single Local* trigger was not implemented until midway through the set.

The second filter shown in Table 11 is the requirement that the event be triggered by one of the four LAC triggers and that there be at least one photon (or a two photon combination) with p_T > PTCUT. For Set A, PTCUT = 3.0 GeV/c. For all others, PTCUT = 4.0 GeV/c. The change is due to changes in the trigger threshold in use when data was collected, allowing a lower threshold for set A.

The fourth line in Table 11 shows the effect of the *veto wall* cut. No signal was allowed in either of the veto walls quadrant(s) covering the LAC trigger octant(s). This cut discriminated against events where a muon, travelling parallel to the beamline, arrived in coincidence with some target interaction. Typically, this interaction would not have satisfied any of the LAC triggers itself. Figure 28(a) shows the position of the photons in the LAC when the veto wall had a signal in the covering quadrant. Figure 28(b) shows the distribution for events where the cut was applied. The surplus of events in the upper part of Figure 28(a) is expected from the greater flux of muons in that region. This is due to effects of the spoiler magnets described in Chapter 2.

The last cut listed in Table 11 is the *vertex* cut. This required that a vertex be found inside the target volume. Events whose interaction took place, for example, in the beam counters were eliminated. It also allowed for the separation of events produced in the Be and Cu targets. The effect of the cut, as shown in Table 11, is consistent with the ratio of target material to other material in the beamline (shown in Table 12).
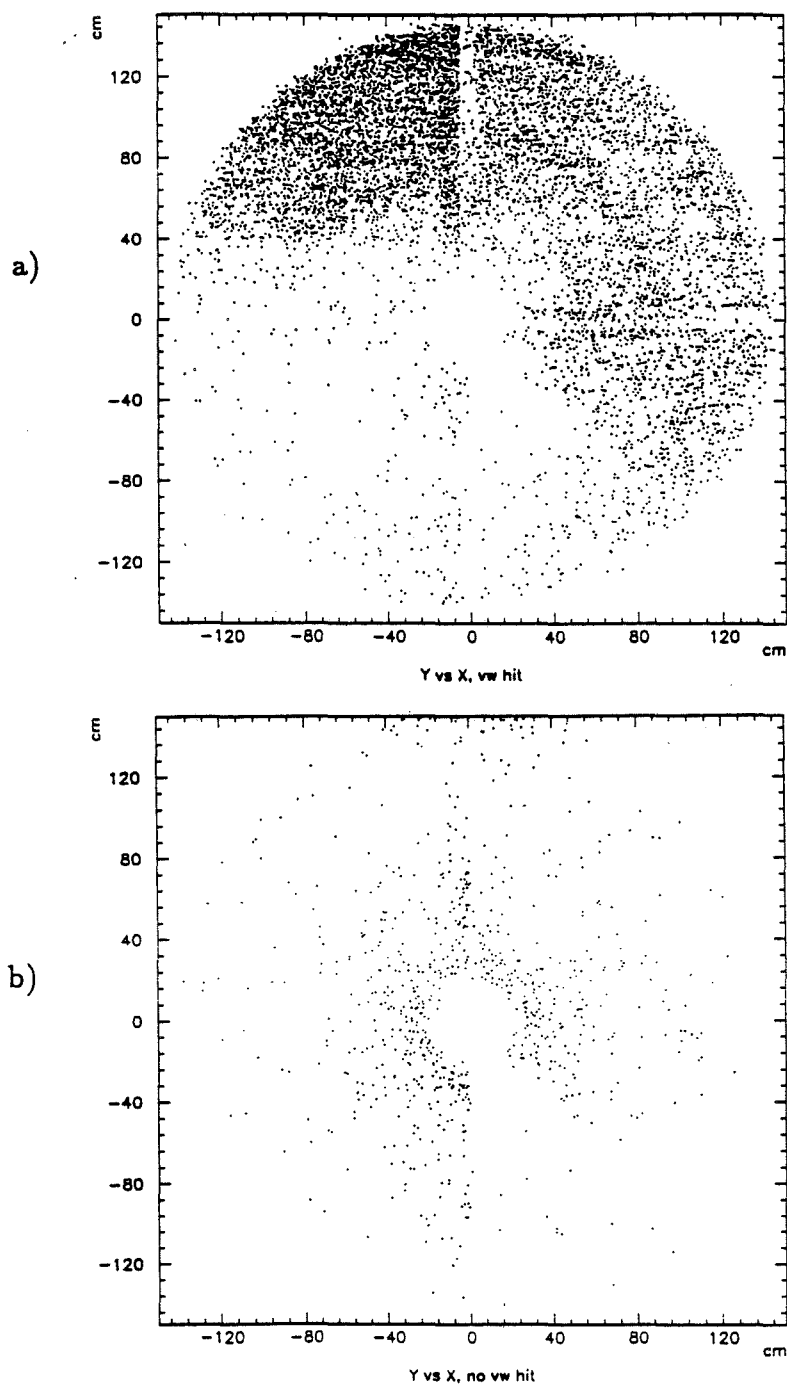
Figure 28   Photon Position for Events a) with Veto Wall Hit
and b) without Veto Wall Hit

Material List Between End of Vacuum Tube and Front of First PWC				
Item	Density (g/cm³)	Thickness (cm)	# Nucleons ($\times 10^{24}$cm^{-2})	Position (cm)
Ti Beam Window	4.5	.0076	.02	-307
Beam Counters	1.0	.5	.30	-227
Air	1.2×10^{-3}	360	.26	–
SSD Box Windows	2.0	.005	.01	-172
Upstream SSDs	1.8	.16	.13	-117 – -2.3
Copper Target	9.0	.16	.84	0 – 0.3
Beryllium Target	1.8	4.0	4.43	0.8 – 7.7
Downstream SSDs	2.3	.22	.39	9.6 – 27
Gas Bag Windows	1.0	.05	.03	51 & 358
Helium	0.12	366	.03	51 – 358
Total	–	–	6.44	–

Table 12   List of Material in Beam Path

It is necessary to correct for the loss of those events whose vertex was not found by the reconstruction algorithm. A study has been made and the efficiency of the vertex reconstructor found to vary between 0.914 and 0.963 depending on interaction position in the target.[35] These efficiencies correspond to the upstream and downstream faces of the target volume. One expects the vertex algorithm to have more success with the downstream vertices because multiple scattering in the target smears the vertex resolution. Since a match to within 3 mm is required in the two orthogonal views, such a position dependence is expected.

Figure 29 graphically displays the effects of the various selection criterion

Figure 29   Two Photon Mass With Various Event Cuts

listed in Table 11. Figure 29(a) is the di-photon invariant mass distribution
for all two photon combinations in events passing the PTCUT criterion. Fig-
ure 29(b) shows the effect of applying the PTCUT to each pair. Figures 29(c)
and 29(d) show the effects of adding, respectively, the veto wall and vertex cuts.
The effect in the η region is not terribly pronounced, whereas the effects at low
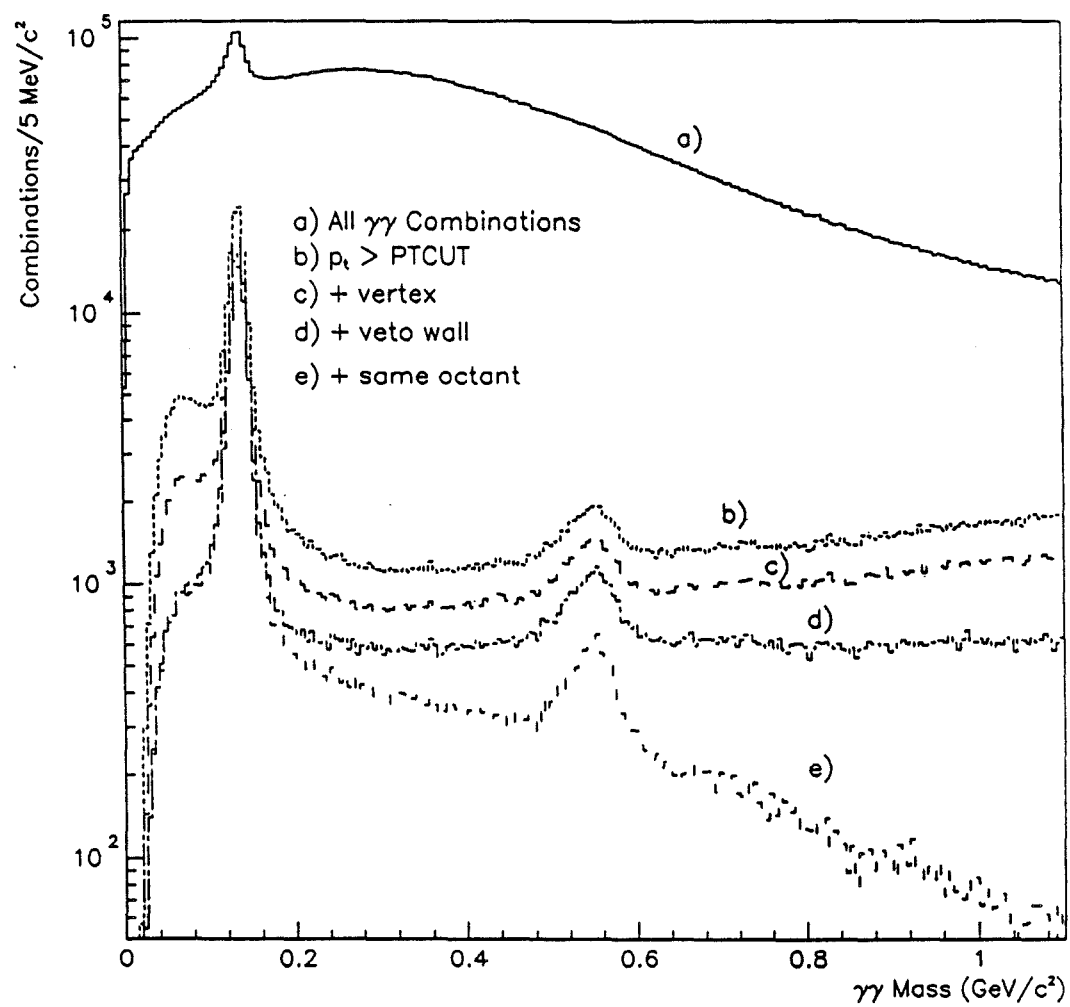mass is quite dramatic. The reason for such large effect at low mass is that the
reconstruction algorithm tends to split the showers of muons and other off-axis
parallel particles into two "photons." These combine to form a low mass pair.
Since the order of the application of vertex and veto wall cuts is reversed for this
plot with respect to Table 11, one can see the interrelated nature of the vertex
and veto wall cuts.[*]

Figure 29(e) shows the effect of requiring that both of the photons from
the pair were in the same octant of the LAC. This cut was motivated by the
trigger construction and has been applied to all following distributions. Since the
experimental trigger was formed on an octant basis this cut makes corrections
for acceptance and trigger efficiency much more tractable.

Photon Pair Selection

Once the event selection cuts have been made, there are a series of cuts that
can be made on the photons or photon pairs. Figure 30 shows the effect of
these cuts. The top curve shows the mass distribution in the η region after the
previously described cuts. The second curve shows the effect of requiring that
the energy asymmetry of the pair be less 0.75.

---

[*] Muons that trigger the experiment tended to be unrelated to interactions in the target.
Most of these "muon events" were caused by muons depositing energy in the LAC in
coincidence with some random interaction signal (*e.g.* low p_T interactions, phototube noise
on the interaction counters). For these events, there usually was no vertex reconstructed.

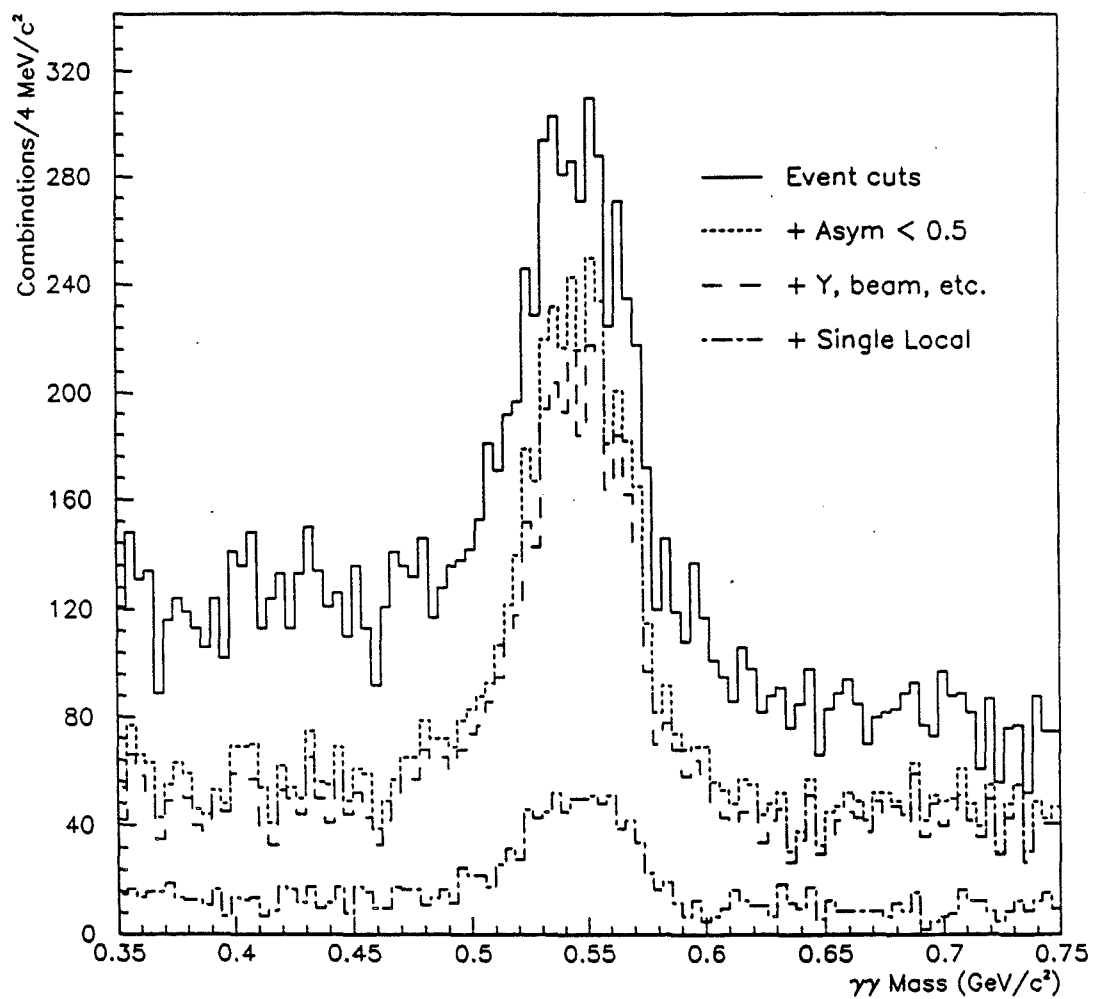Figure 30   Two Photon Mass Distribution in η Region With Cuts

$$\text{Asym} = \frac{\mid E_1 - E_2 \mid}{(E_1 + E_2)}$$

η Asymmetry, mass band

η Asymmetry, side band

η Asymmetry, side band subtracted
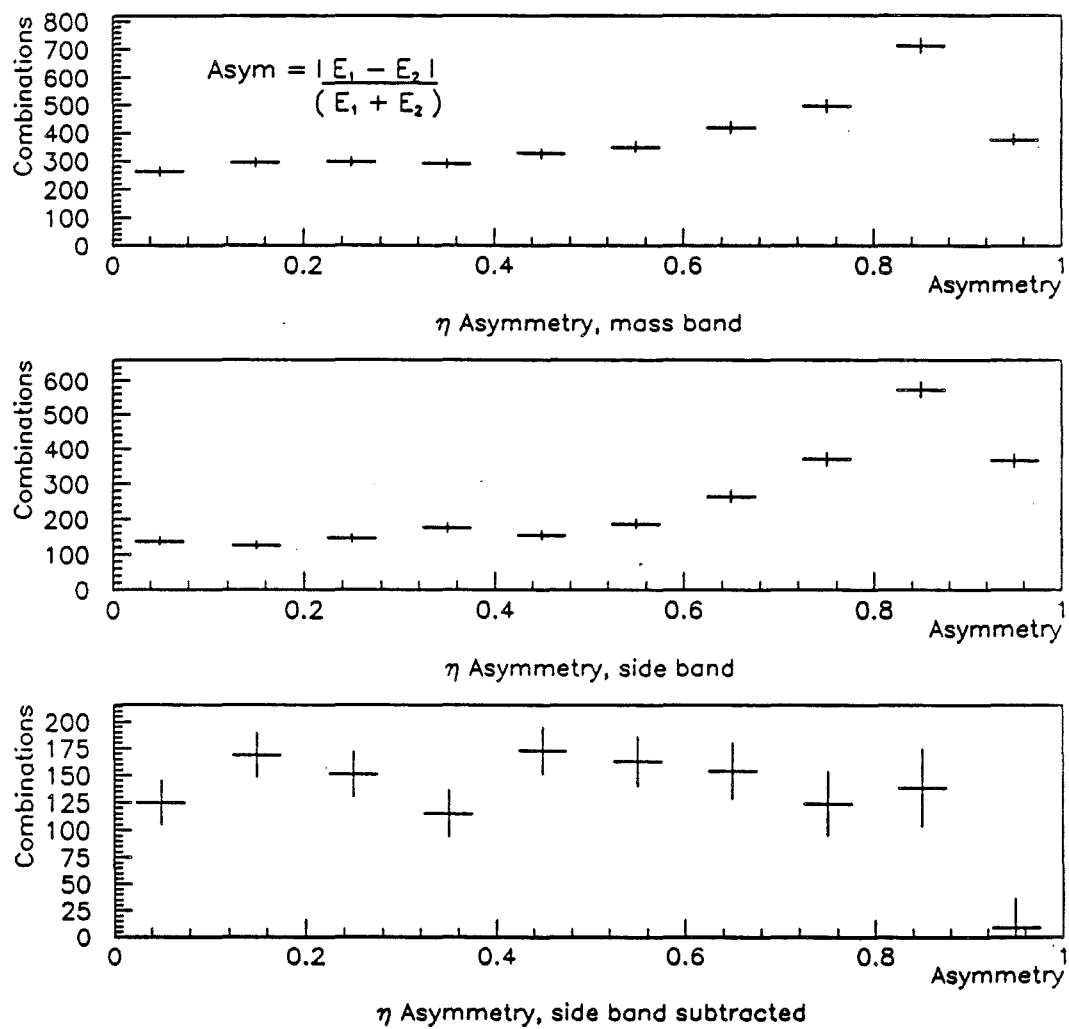
Figure 31 η Asymmetry

The energy asymmetry is defined as

$$\text{Asymmetry} = \frac{|E_i - E_j|}{(E_i + E_j)} \approx cos\theta^*$$ (5.1)

where E_n is the energy of the individual photons, and θ^* is the center of mass angle of the photons with respect to the η (π°) direction. For psuedoscalars, like the η and π°, the decay distributions should be flat in $cos\theta^*$.

Figure 31(a) shows the asymmetry distributions of photon pairs with a mass between 450 and 650 MeV/c. Figure 31(b) is the same plot for photon pairs with masses in one of the two *side bands* ($350 \leq mass \leq 450$ MeV/c and $650 \leq mass \leq 750$ MeV/c). Events in these side bands are used to approximate the characteristics of the background under the η peak. The typical procedure for many of the following steps will be to plot a quantity for the η region, the same quantity in the side band regions and the subtracted result. This *side band subtracted* result represents the result from the η alone. Figure 31(c) shows the background subtracted result. At high asymmetry, there is a large background subtraction and a small energy error translates into a large correction difference. For these reasons, η candidates with asymmetries larger than 0.75 are removed from the sample. Since one expects the asymmetry of the photons to be a uniform distribution, the asymmetry range allowed can be truncated and simply corrected by $1/(1 - A_{max})$ where A_{max} is the maximum allowed asymmetry.

The third curve in Figure 30 shows the effects of making a series of *cleanliness* cuts. These small cuts made the data sample more uniform. These cuts were:

- The vertex must be reconstructed in the beryllium target;

- The beam particle may not be tagged as a minority particle (K^- or π^+);

- The rapidity range was $-0.7 < Y < 0.7$.

Data from the copper foil was cut to avoid clouding the issue with any nuclear dependencies. Minority particles were cut to better identify the interacting hadrons. The rapidity range was cut to exclude the innermost region of the detector (where the geometric acceptance was low) and the outermost region (where the trigger efficiency was low) to avoid regions were corrections to the data would be large.

The final curve in Figure 30 shows the result of requiring the *Single Local* trigger. This distribution is shown in detail in Figure 32. There, the regions marked A and C show the side bands discussed above; region B is the mass band. Even though the effect of the *Single Local* requirement looks devastating on the previous plot, the signal to noise ratio is still $\approx 4 : 1$. This plot shows the data sample used for the cross section measurements shown in a following section.

5.2 LAC PERFORMANCE

<u>Mass Resolution</u> The invariant mass shown in the preceeding figures is calculated using

$$m^2 = 2E_i E_j (1 - cos\theta_{ij}) \qquad (5.2)$$

where E_i and E_j are the energies of the two photons and θ_{ij} is the opening angle between them. The widths of the π° and η peaks are consistent with an energy resolution given by:[14]

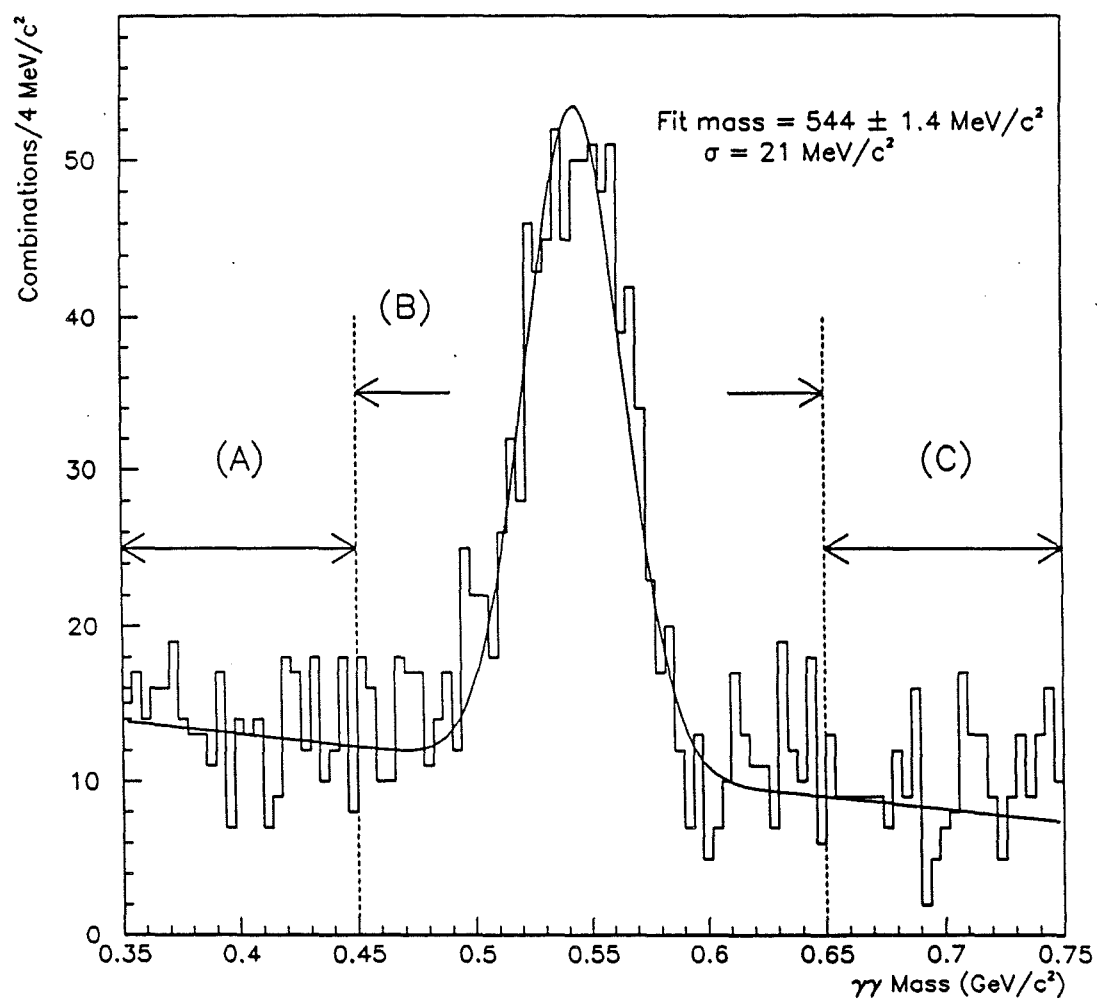$$\sigma^2 = (0.10)^2 + (0.15)^2 E + (0.02)^2 E^2 \qquad (5.3)$$

Figure 32   Two Photon Mass Distribution in η Region With All Cuts

where the first term is due to electronic noise in the amplifiers, the second reflects the intrinsic resolution of the LAC and the last term reflects gain uncertainties.

Energy Scale   As mentioned in Section 4.1.1, there are eight separate energy scales used for the LAC. Figure 33(a) shows the π° mass for each octant. The two octants within a quadrant are expected have the same energy scale, but differences between quadrants can be attributed to differences in high voltage and construction. The energy scale of each octant is determined by forcing the average π° mass to be $135 \, \text{MeV}/\text{c}^2$.[*] Figure 33(b) shows the average η mass for each octant. The scales on both plots have a displayed range of $\pm 5\,\%$. The dotted horizontal line indicates the accepted values of $134.95 \, \text{MeV}/\text{c}^2$ and $548.8 \, \text{MeV}/\text{c}^2$ for the π° and η masses, respectively. The average η mass comes out low for all octants, but all octants are within $1\,\%$ of the accepted value. The average of all octant averages is $546.3 \pm 0.7 \, \text{MeV}/\text{c}^2$.[†] Since there was no software constraint on the η mass, agreement to this level is satisfying.

5.3 CROSS SECTION CALCULATION

Once the data sample is selected, the cross sections are calculated using the formula

$$E\frac{d^3\sigma}{d^3p} = A\left(\frac{N}{N_{beam}N_{scat}}\right)\left(\frac{1}{2\pi \mathrm{p}_T \Delta \mathrm{p}_T \Delta Y}\right) \tag{5.4}$$

where,

---

[*] The results in Figure 33(a) are not exactly $135 \, \text{MeV}/\text{c}^2$ for each octant because the process of fixing the mass is an iterative procedure since the population changes every time the energy scale is changed. Differences of $0.25\,\%$ are deemed insignificant since that was the accuracy of the fitting method(s).

[†] This result is slightly different from that shown in Figure 32. The reason is that for this result the *Single Local* requirement was dropped to get enough statistics to split the sample by octants.
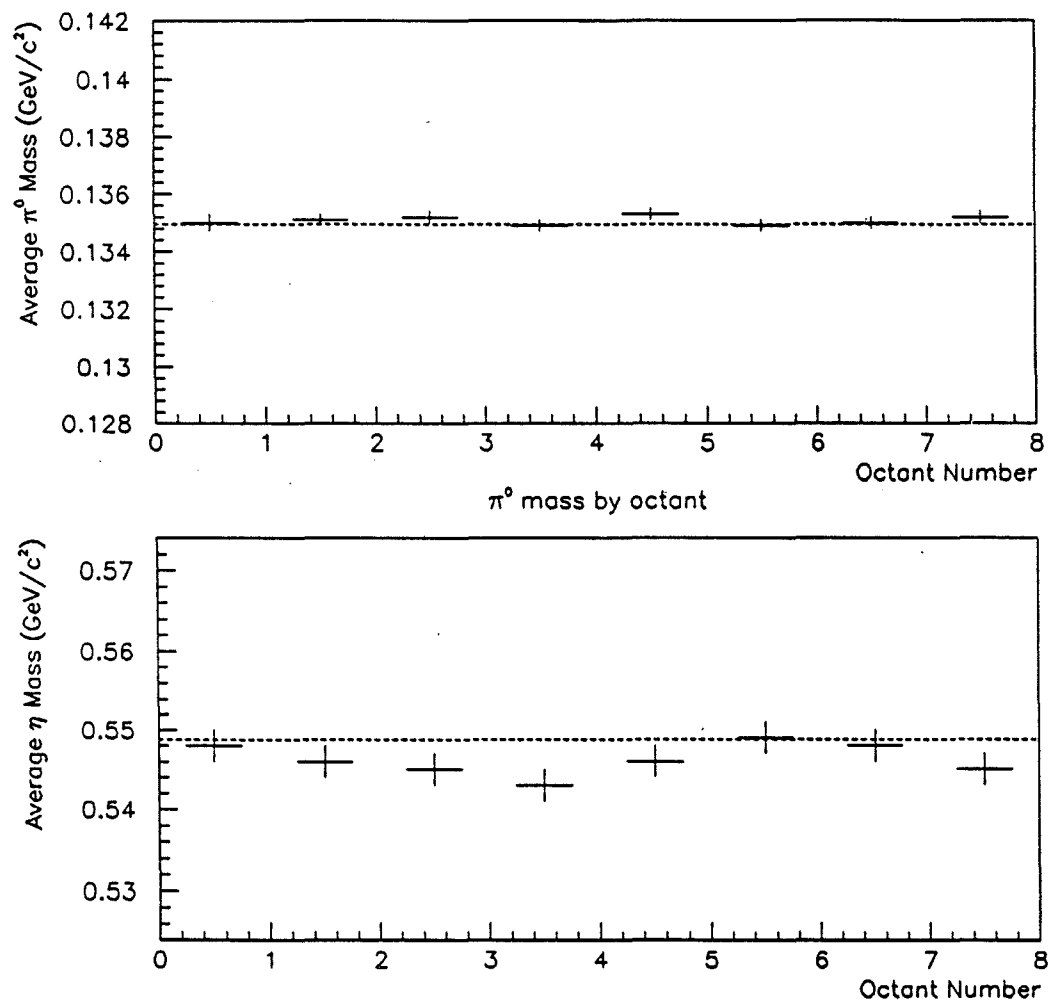
Figure 33 π° and η Mass by Octant.

- A is the normalization factor

- N is the number of particles reconstructed

- N_{beam} is the number of incident beam particles

- N_{scat} is the number of scattering centers (target nucleons) per unit area

- Δp_T is the size of the p_T bin

- ΔY is the rapidity interval.

The term $\frac{1}{2\pi \Delta P_T \Delta Y P_T}$ is called the phase space factor and normalizes the cross section to an element of phase space.

Typically N is not all the particles that were incident and a series of corrections must be made. These are imbedded in A and will be discussed below.

Geometric Acceptance and Reconstruction Efficiency   Monte Carlo methods were used to determine the geometric acceptance of the detector and the efficiency of the reconstruction code. The CERN simulation package $GEANT$[36] was used to model the response of the spectrometer. The output of the simulated events was then processed by the same $MAGIC$ reconstruction package that was used to reconstruct the data. Measuring the losses through these two stages determined the acceptance and reconstruction efficiency for the π° and η.

A two dimensional grid in p_T – rapidity space was made, covering the region from 3.5 to 9 GeV/c in p_T and -0.8 to 0.8 in rapidity. Rapidity steps were 0.1 and p_T steps were 0.5 GeV/c. At each point on this grid 1000 π°'s and η's events were simulated using $GEANT$ and the number of π° and η mesons

where both of the decay photons[*] were inside the fiducial volume[†] of the LAC was recorded. The ratio of this number to the total number simulated is the geometric acceptance of the detector.

Those events where both photons fell inside the fiducial region were reconstructed using *MAGIC* and the ratio of number reconstructed to the number accepted is the reconstruction efficiency. The product of these two ratios is displayed in Figure 34 for η and π° mesons. Differences between to two are largely accounted for by the greater geometric losses for the η, due to larger opening angle.

Trigger Corrections   This analysis uses the *Single Local* trigger for its data sample. As mentioned in Section 3.2, this is not the trigger of choice for studying η mesons, but has the advantage of being minimally affected by the image charge problem also described there. The *Single Local* trigger is, at this point, much better understood and more accurately modelled. Also, the Local • Global High trigger was found to fail $\approx$ 35 % of the time for unknown and seemingly random electronic reasons. For these reasons, the *Single Local* trigger is used.

This trigger required that p_T deposition in the LAC exceed a threshold level. Due to fluctuations in the p_T signal, the trigger efficiency was not a step function but rather followed a "turn-on" curve similar to the one shown in Figure 35. Because of this, there is a correction necessary at lower p_T for

---

[*] For the purpose of increasing statistics only the $\gamma\gamma$ decay mode was allowed for these two particles.

[†] The LAC was built in eight sections with structural material a the periphery of the octants. To prevent losses of energy down these cracks between octants there was a 2 cm "fiducial" cut made around the edges of an octant. This required that photons be at least 2 cm from the nearest octant boundary.
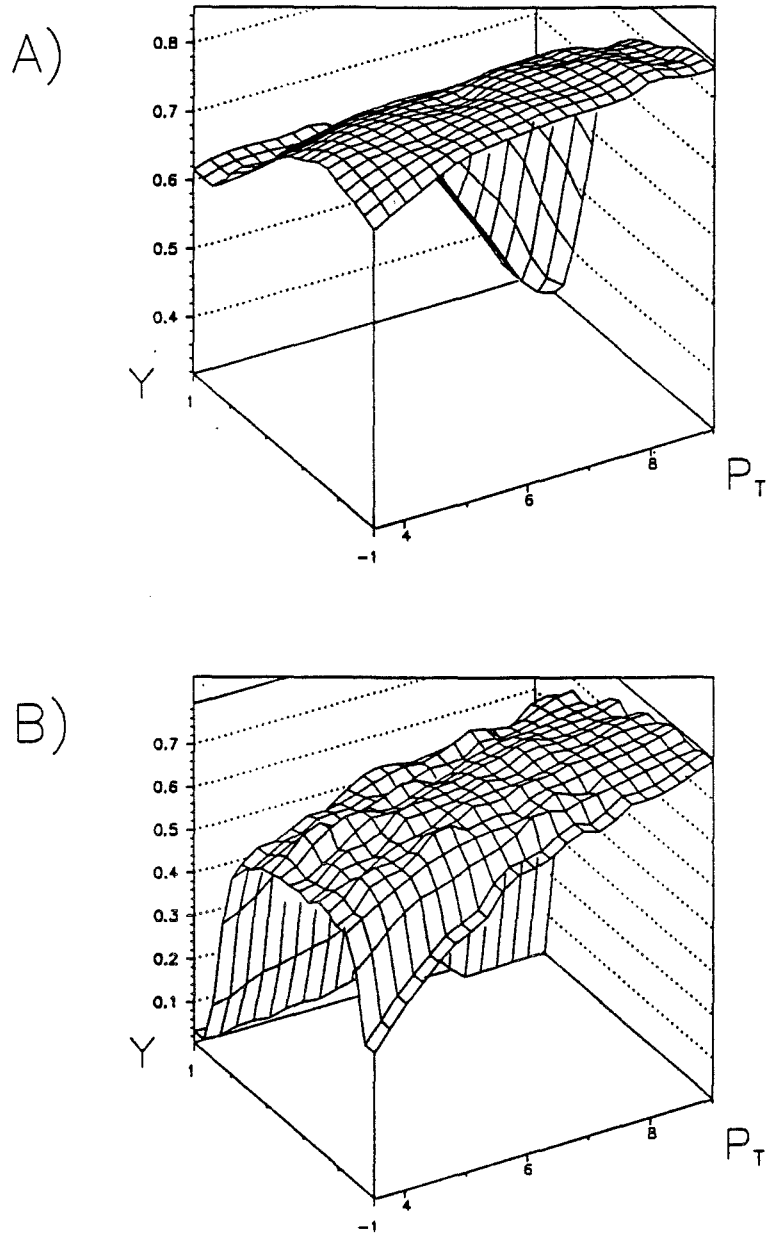
Figure 34   Geometric Acceptance and Reconstuction Efficiency Distribution
for a) π° mesons and b) η mesons.
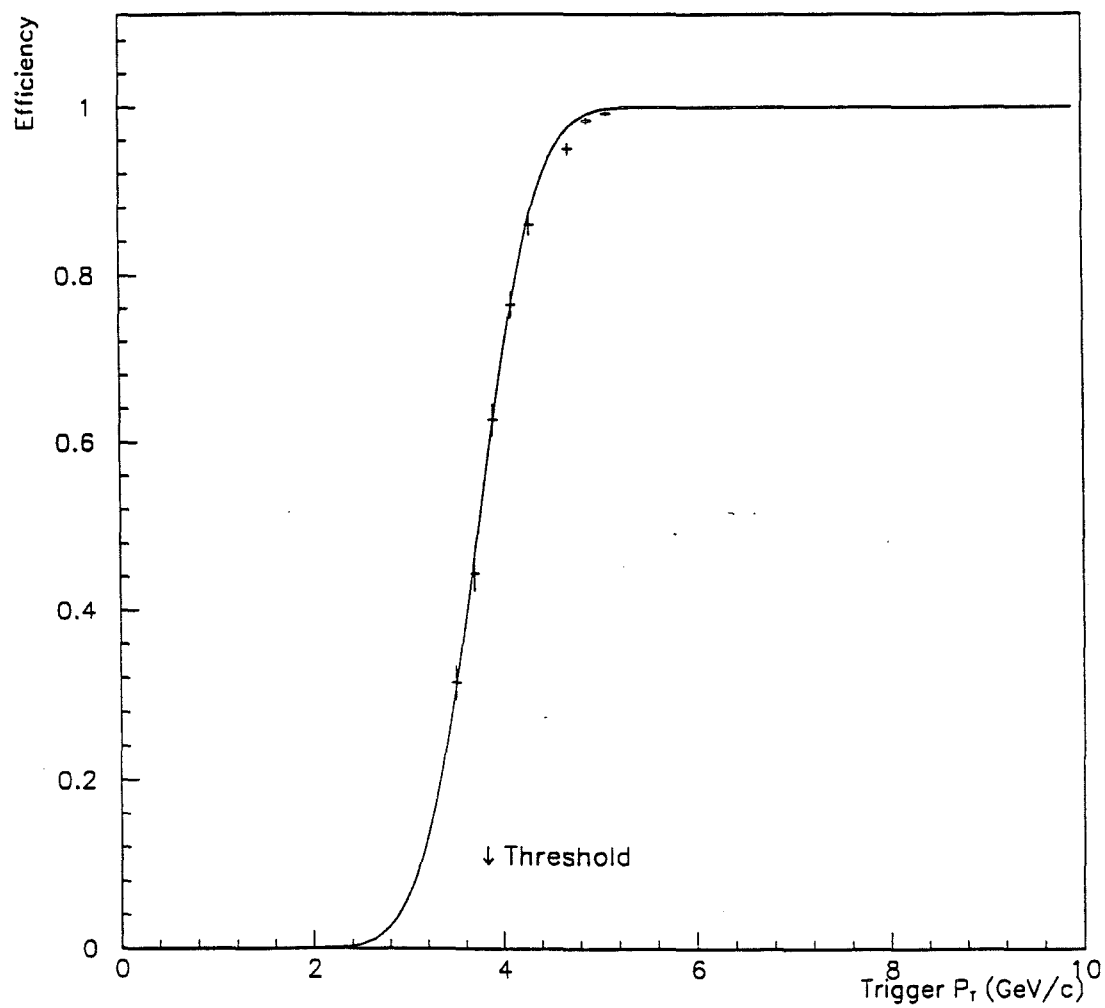
Figure 35 Trigger Efficiency vs. p_T for a Typical Octant

events that the trigger missed. This correction was determined by simulating the trigger in software and determining the probability an event had to trigger the experiment. The simulation was done using the Monte Carlo events generated for the acceptance measurements. The reconstructed photons in the trigger quadrant were projected back onto the R strips.[‡] These strip energies were then summed into groups of 16 and the highest sum was compared to the efficiency curve generated for that trigger region. The efficiency curve was generated by taking the ratio of the number of triggers that satisfied the high threshold to the number that should have satisfied the high threshold. The latter term was determined from events satisfying the low threshold trigger and using the strip energies to determine if the high threshold should have been satisfied.

Other Normalization Corrections   There are a series of small corrections that are made to the data to correct for losses of beam particles and photons. These are listed in Table 13. The following paragraphs detail the corrections and their motivations.

- Missing Octant   Since the *Single Local* trigger was constructed for each octant individually, it was possible for a given octant to be disabled or have a higher threshold than other octants. Rather than calculate eight separate cross sections, each di-photon pair was given a weight of $8/n$ where $n = $ the number of octants active at that p_T .

- Beam Count   Two corrections are necessary to the beam count. The first is due to situations where one beam bucket contained two (or more)

[‡] This process only used the R view because there is no information from the ϕ view used in the trigger modules.

	Beam and Target Type			
Correction	π^-on Be	π^-on Cu	p on Be	p on Cu
Missing Octant	Function of Run and p_T			
Geometric Acceptance	Function of p_T and Rapidity			
Reconstruction Efficiency	Function of Run and p_T			
Trigger Acceptance	Function of Run and p_T			
Double Beam Occupancy	0.98			
Asymmetry < 0.75	1.333			
π° Mass Cut	1.04			
η Mass Cut	1.04			
Photon Conversions	1.069			
Veto Wall	1.176			
Beam Absorption	1.010			
Density (gm/cm^3)	1.848	8.96	1.848	8.96
Atomic Number	9	29	9	29
Beam Absorption	1.043	1.004	1.056	1.005
Minority Contamination	1.014	1.014	1.06	1.06
Vertex Efficiency	Function of Reconstructed Vertex Position			

Table 13   Listing of Corrections Applied to the Data

particles. The beam counters did not distinguish between such instances and those with one particle in the beam bucket. This correction was determined to be $\approx 2\%$ using the beam rate and Poisson statistics.

The second correction was due to loss of scaler information for the final spill of some runs. This was due to a bug in the data acquisition software. The beam count for such runs was modified by the ratio (# of events/#

of events from all but last spill). This assumes that the beam flux during the last spill was the same as the run average.

- **Asymmetry**   The energy asymmetry of π° and η mesons was cut at 0.75. Since both of these particles are psuedoscalar mesons, one expects the asymmetry distribution to be uniform. For this reason, a correction of $1/0.75$ was applied to correct for lost mesons.

- **Mass Cut**   The mass cuts applied on the definition of the π° and η will cause some misreconstructed π° or η to be cut. By looking at losses in the π° region this effect was estimated to be $\approx 4\,\%$. The window for both particles was taken to be $\pm 4\,\sigma$ so the same value was used for the η band as well.

- **Veto Wall**   There was a loss of π° and η mesons due to accidental coincidence of a signal in the veto wall and a high p_T event. This loss was found to be $17\,\%$ for the π° and assumed to be the same for the η.

- **Beam Absorption**   The beam particles were counted using scintillators positioned 228 cm upstream of the target region. Any beam particle that interacted before reaching the target was unavailable for the production of a high p_T interaction in the target.[*] This was also true within the target in that beam particles interacting in the upstream target segments were lost to the downstream segments. On average, the beam traversed the material between the beam counters and the middle of the target material. Table 13 shows the corrections applied for the two beam polarities.

---

[*] The reaction particles from such an interaction are very likely to themselves traverse the target but since the p_T spectrum is such a strong function of interacting particle energy these incident particles are effectively removed from consideration.

- Conversions Both the π° and η decay within a few angstroms of their creation position. The photons from the decays have some probability of converting to an electron/positron pair before reaching the LAC. If this conversion takes place downstream of the analysis magnet, the position of the pair will be the same as the photon and the energy measurement will be approximately correct. However, if the conversion is upstream of the magnet, the electron and positron will be swept apart and the LAC will detect three separate particles. Such conversions would cause this analysis to lose these π°'s or η's. One can either try to reconstruct these conversion cases[†] or correct for the losses. In this analysis, a correction is made to the number of π° or η mesons found. The correction is based on the position of the reconstructed vertex and the amount of material remaining to be traversed before the downstream face of the analysis magnet.

5.4 RESULTS

The final results of our measurements are shown in Figures 36 and 37. Figure 36 shows the p_T distribution for the invariant differential cross section for the reaction $\pi^- + Be \rightarrow \eta + anything$ averaged over the rapidity range $|y| < 0.7$. Data span the p_T range from $3.5\,\mathrm{GeV/c}$ to $8.5\,\mathrm{GeV/c}$. Figure 37 shows the analogous data for $p + Be \rightarrow \eta + anything$ also averaged over the full rapidity range.

The ratio of η meson to π° production for both π^- and p beams is shown in Figure 38. Figure 38(a) shows the ratio of η/π° cross sections from π^- beam for

---

† This path has been followed by W. Desoi and Keith Hartman for their analysis.
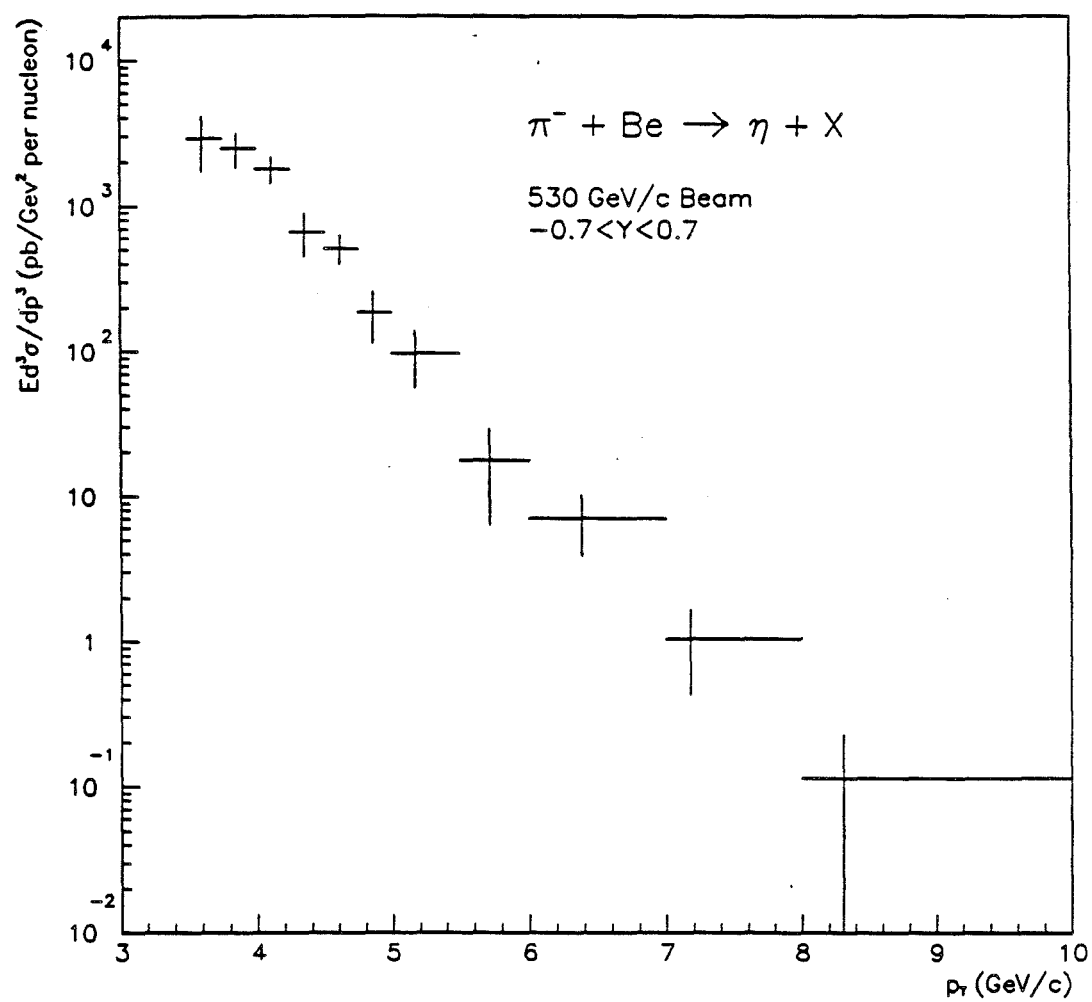
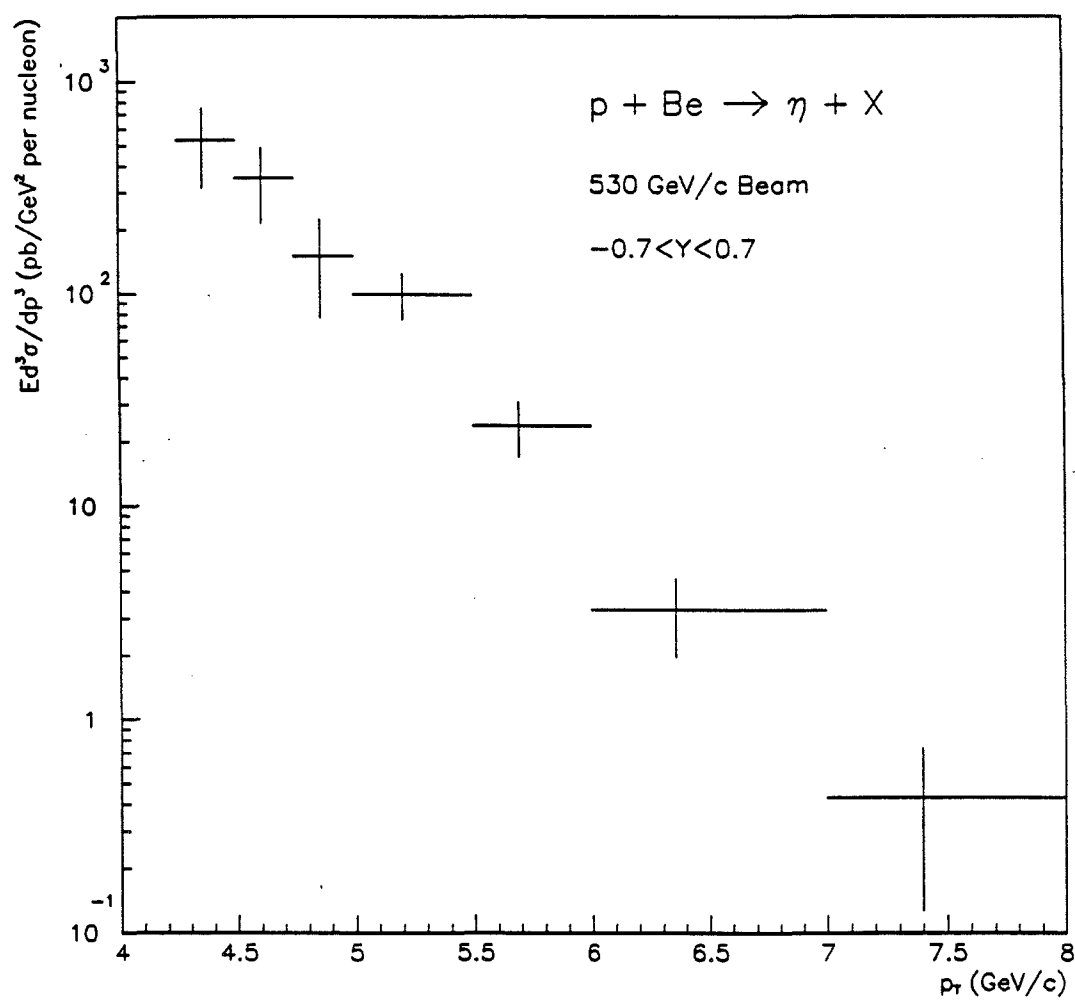Figure 36   Invariant Cross Section for $\pi^-\mathrm{Be} \to \eta\,\mathrm{X}$

Figure 37   Invariant Cross Section for pBe → ηX
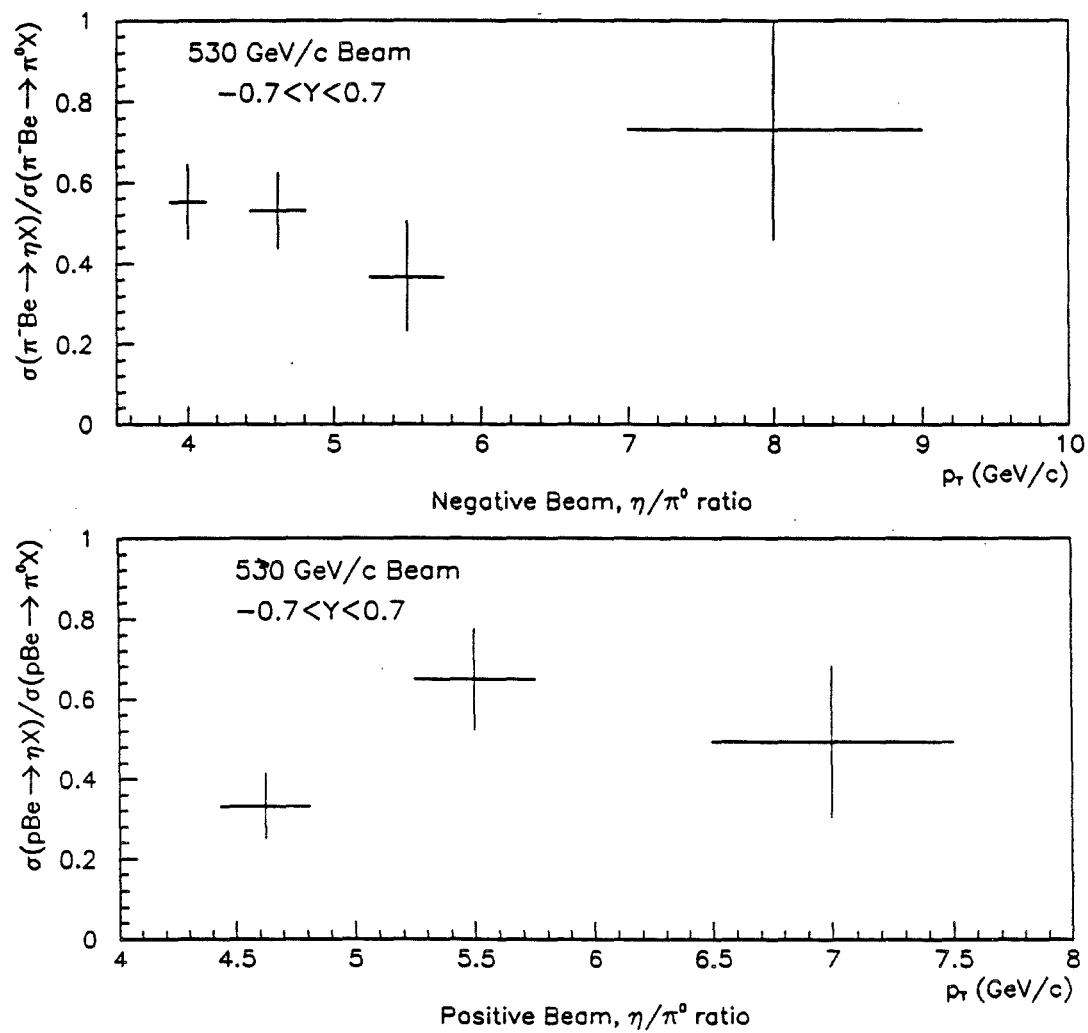
Figure 38   Ratio of η to π^o Production

the p_T range 3.75 GeV/c to 10.0 GeV/c. There is no significant variation with p_T and a mean value of 0.52 ± 0.06. The analogous ratio for proton data is shown in Figure 38(b). Again, the results are consistent with no dependence on p_T , but suggest, if anything, a slight rise with p_T. The range of p_T for proton data is 4.25 GeV/c to 8 GeV/c. The mean value for the ratio is 0.44 ± 0.06.

Figure 39 shows the η signal from K^- beam. The quantity measured was the ratio of production of η mesons from a K^- beam to that from a π^- beam. For this measurement a slightly different series of cuts were applied. The requirement for a *Single Local* trigger was dropped, as was the veto wall cut and the same octant requirement on the two decay photons. The asymmetry cut was tightened to Asym < 0.5, and the combination was dropped if either photon of the pair satisfied any of the following conditions:

- The photon was more than 50 ns out of time;

- There was a charged track pointing to within 1 cm of the photon shower;

- The ratio of energy deposited in the front of the EMLAC to the total was less than 0.2;

- The directionality was > 0.4.[*]

The ratio of η mesons from π^- beam to those from K^- beam was measured to be 1.32±0.32 for the p_T range 3.5 − 6.0 GeV/c.[†] These results will be discussed in the following chapter.

---

[*] The *directionality* is a measure of whether the electromagnetic shower points to the target. Photons coming from the target have a directionality of 0.0. Those coming parallel to the beamline have ≈ 1.0. Further details on this quantity can be found in Ref. 22.

[†] The count of η mesons from π^- beam was scaled, depending on the run, from 0.8% to 1.5% to correct for Cherenkov tagging efficiency and K^- fraction of the beam. A full description of minority particle tagging can be found in Ref. 37.

Figure 39 η Signal from K$^-$ Beam

127
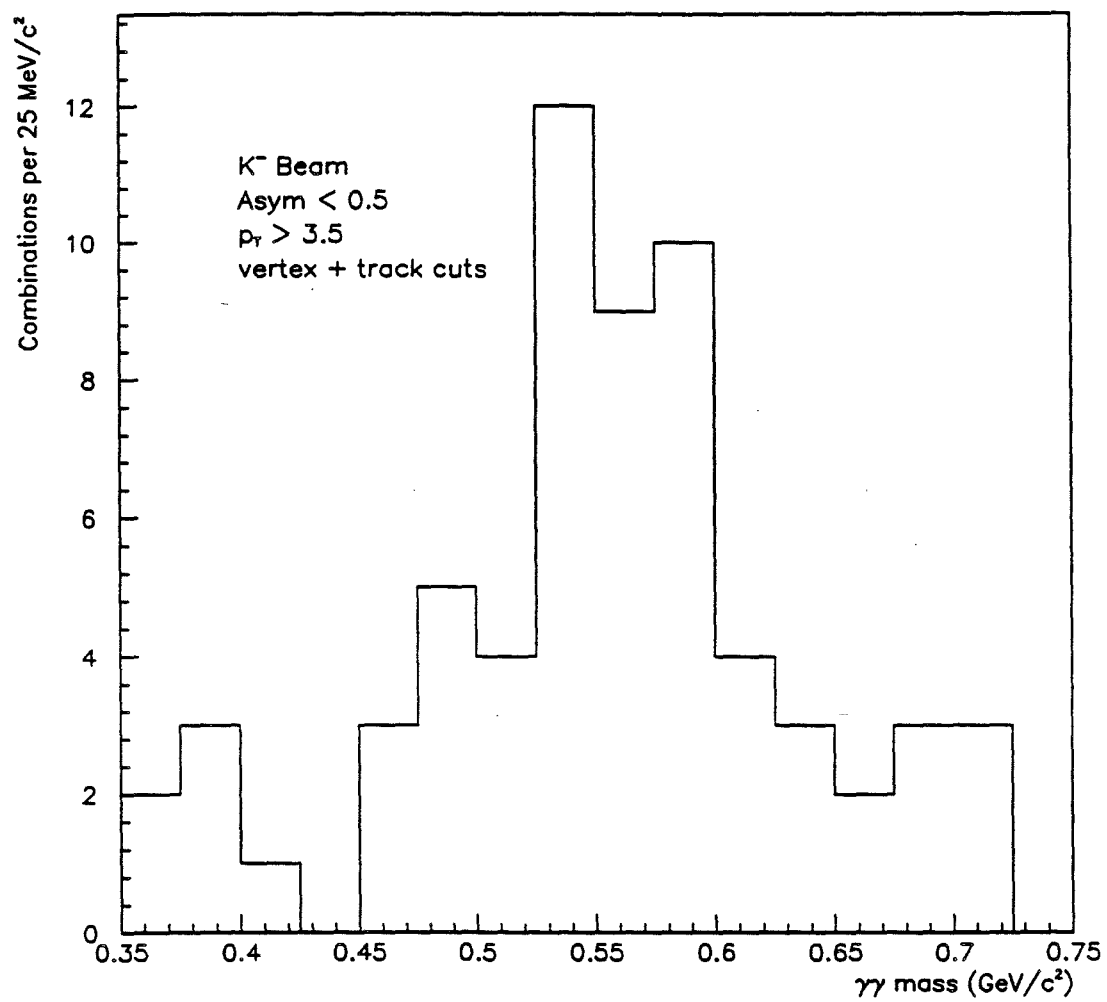
6. Conclusions

In this thesis the 1987-8 data from E706 has been analyzed to study the high p_T production of η mesons. As expected, the cross section was found to fall with p_T as expected and to have essentially the same p_T dependence as the π° yields. This was found to be true for production from both 530 GeV/c proton and π^- beams. The ratio of cross sections for production of η and π° mesons was found to be ≈ 0.5, in good agreement with previous measurements.[5-11] The production of η mesons from K^- beam was also studied and the ratio of cross sections for inclusive η production from K^- and π^- was found to be 1.32 ± 0.32. While this is not significantly different from unity, it provides a tantalizing hint that strange quark content in the beam particle may affect the production of η mesons. This result is also in close agreement with a previous measurement in a different kinematic region.[8]

The measured inclusive cross sections for $\pi^- \text{Be} \rightarrow \eta \text{X}$ and $\text{p Be} \rightarrow \eta \text{X}$ are summarized in Table 14, where the data is binned in p_T . The ratio of cross sections for η/π° is listed in Table 15. The ratio is consistent with being constant in p_T , with a mean value of 0.44 ± 0.06 for p beam and 0.52 ± 0.06 for π^- beam. In Figure 40, this ratio is compared to the results from experiments described in Chapter 1.* Our results are consistent with all those shown. The ratios from UA6,[11] WA70,[10] and Donaldson, et al.[8] are equal or slightly lower, and the ISR results (R806,[7] and AFS[5]) may be slightly higher. This suggests a possible beam energy dependence. The same results are plotted as a function of

---

* The ratio is compared rather than cross sections since effects due to systematic uncertainties are minimized in the ratio.

η Cross Section (pb/GeV/c^2 per nucleon)				
	π^- Beam		p Beam	
p_T bin	Avg. p_T	$E\frac{d^3\sigma}{dp^3}$	Avg. p_T	$E\frac{d^3\sigma}{dp^3}$
3.75	3.86	2470 ± 660		–
4.0	4.11	1790 ± 370		–
4.25	4.35	660 ± 220	4.36	530 ± 220
4.5	4.62	510 ± 120	4.61	350 ± 140
4.75	4.86	184 ± 71	4.86	150 ± 73
5.0	5.17	97 ± 41	5.21	99 ± 24
5.5	5.71	18 ± 11	5.69	23.9 ± 6.9
6.0	6.38	7.0 ± 3.2	6.36	3.3 ± 1.3
7.0	7.17	1.04 ± 0.62	7.40	0.43 ± 0.31
8.0	8.3	0.11 ± 0.11		–

Table 14 η Invariant Cross Section

Ratio of η Cross Section to π^0 Cross Section			
p_T bin	π^- Beam	p Beam	K^- Beam
3.75 – 4.25	0.551 ± 0.092	–	–
4.25 – 5.0	0.530 ± 0.094	0.332 ± 0.082	–
5.0 – 6.0	0.367 ± 0.135	0.649 ± 0.126	–
6.0 – 8.0	0.72 ± 0.28	0.49 ± 0.19	–
8.0 – 10.0	0.9 ± 1.2	–	–
Average	0.517 ± 0.058	0.435 ± 0.065	0.68 ± 0.17

Table 15   Ratio of η/π^0 Cross Sections
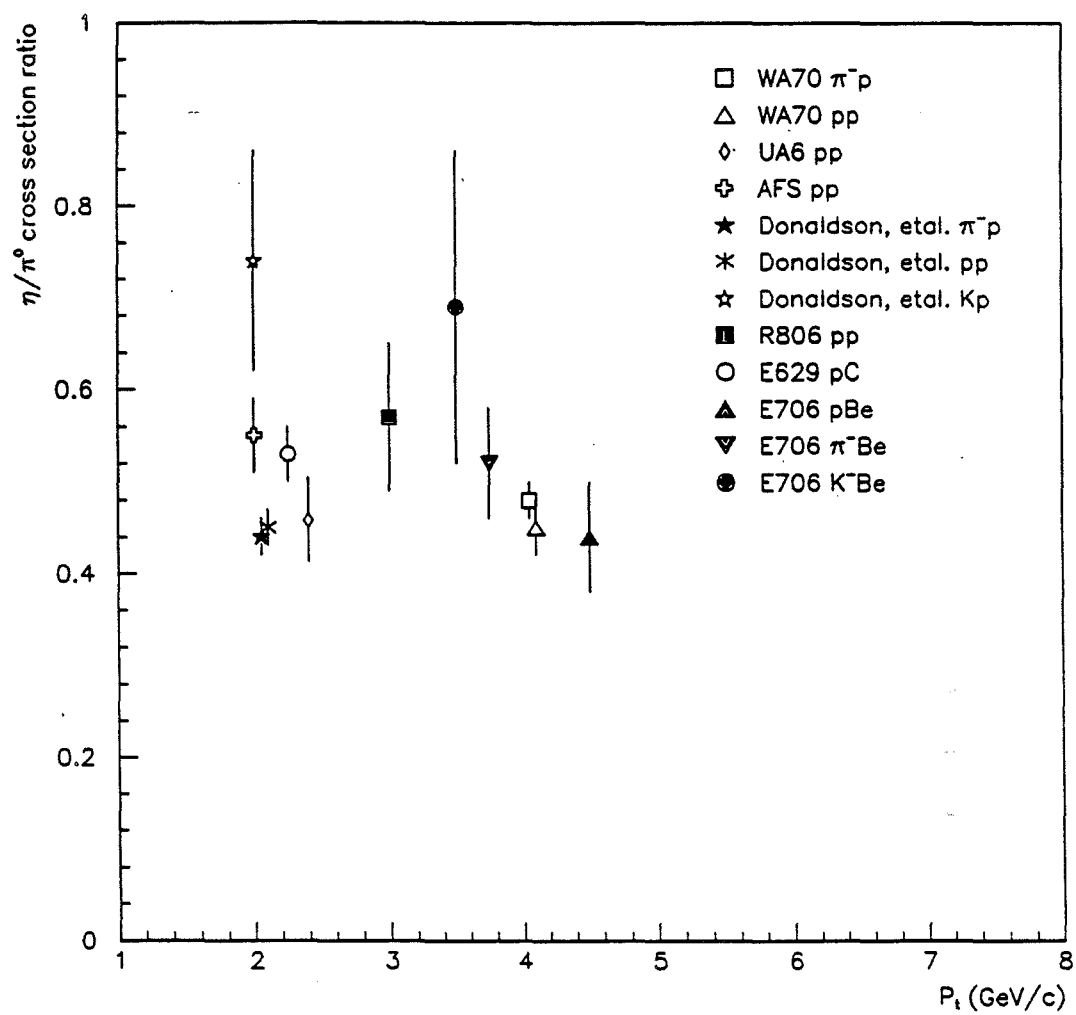
Figure 40   World Results on η/π° Ratio vs. p_T
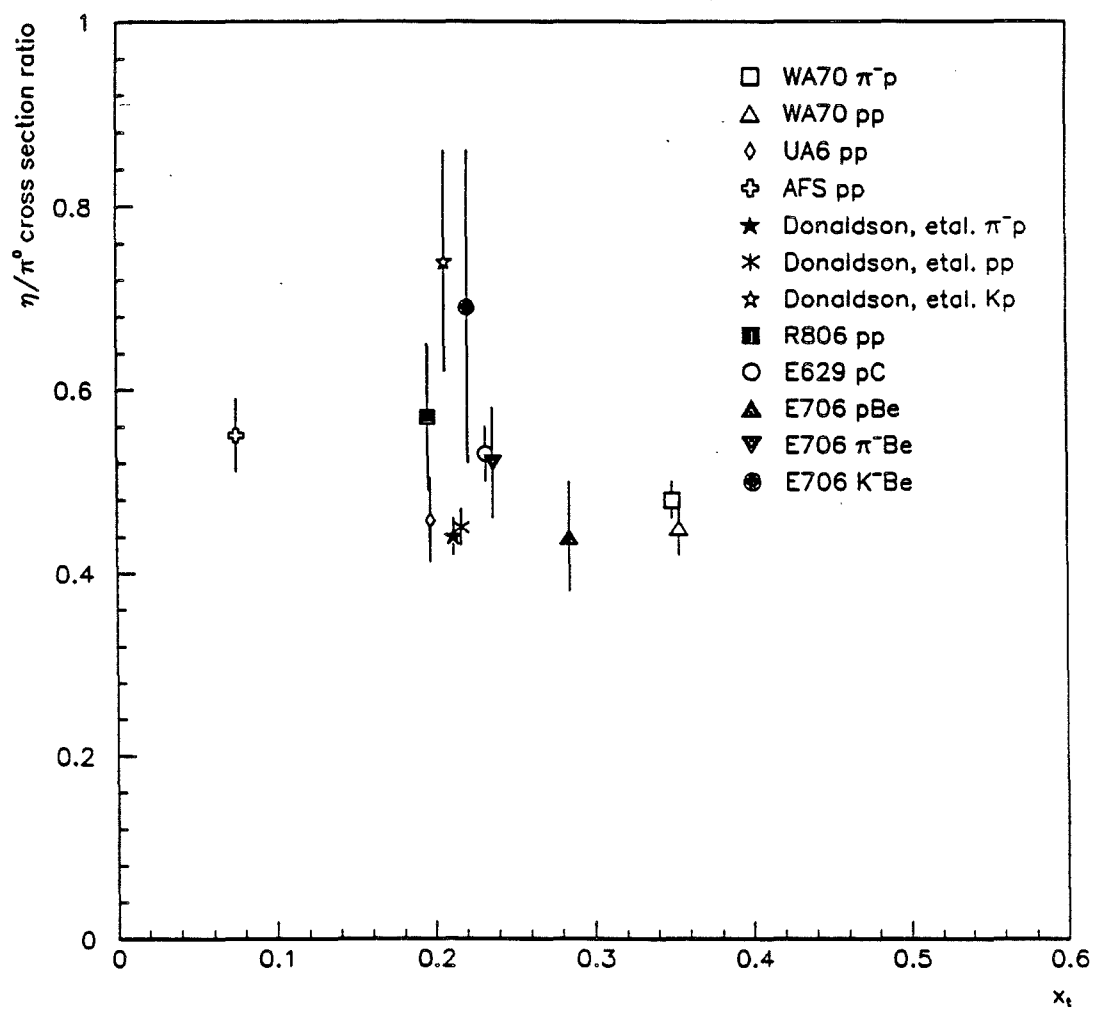
Figure 41   World Results on η/π° Ratio vs. x_T

x_T[†] Figure 41. Here one sees the hint of a trend to lower values of the ratio with increasing x_T . This is consistent with the increasing importance of the valence quark contribution to production at large x_T . In addition to the π^- and p beam data, there are also two results presented for the η/π° ratio from K beams. In the case of Donaldson, *et al.*, the result is an average of K^+ and K^-, whereas for our case the result is for K^- only. Furthermore, our value of η/π° for K^- is obtained by multiplying the measured $\eta(K^-)/\eta(\pi^-)$ ratio by the measured η/π° ratio for π^- beam. The calculation requires uses the result from Ref. 37 on the ratio of $\pi^\circ(K^-)/\pi^\circ(\pi^-)$, which is 0.92 ± 0.05.

In conclusion, we have shown that the results and quality of the measurements of η production, and the ratio of η/π°, are consistent with the best world data. From the upcoming physics run of E706, approximately a tenfold larger data sample is expected with improvements in the MW spectrometer. This holds promise of greatly reduced systematic uncertainties, and the ability to make precise comparisons between π^- and K^- induced production with the larger data sample. This will provide more quantitative conclusions than we have obtained thus far on the relative importance of gluon, sea and valence quark fragmentation in the production of η mesons.

---

† $x_T = 2p_T/\sqrt{s}$ is the transverse momentum fraction of the hadron. Baring scaling violations, for a given x_T value, experiments at different beam energies should have the same results.

REFERENCES

1. M.R. Pennington, *Rep. Prog. Phys.* **V46** (1983), 393–513.

2. J.F. Owens, *Rev. Mod. Phys.* **59 No. 2** (1987), 465–503.

3. T. Ferbel and W.R. Molzon, *Rev. of Mod. Phys.* **56** (1984), 181.

4. D.H. Perkins, *Introduction to High Energy Physics*, Addison-Wesley, (1982) 188-196.

5. T. Åkesson, *et al.*, *Physics Letters* **158B** (1985), 282.

6. F.W. Büsser, *et al.*, *Physics Letters* **55B,2** (1975), 232.

7. C. Kourkoumelis, *et al.*, *Physics Letters* **84B,2** (1979), 277.

8. G.J. Donaldson, *et al.*, *Physics Review Letters* **V40,11** (1978), 684.

9. J. Povlis, *et al.*, *Physics Review Letters* **V51,11** (1983), 967.

10. M. Bonesini, *et al.*, *Zeitschrift für Physik C* **42** (1989), 527–532.

11. J. Antille, *et al.*, *Physics Letters B*, **V194,4** (1987), 568.

12. W.F. Baker, Private communication.

13. Ioanis Kourbanis, PhD Dissertation, Northeastern University, 1989.

14. William Desoi, PhD Dissertation, University of Rochester, 1989.

15. E.Engels, *et al.*, *Nucl. Instr. and Meth.* **A279** (1989), 272.

16. E. Engels,*et al.*, *Nucl. Instr. and Meth.* **A253** (1987), 523.

17. Carl Bromberg, E706 Internal Note 94.

18. *CAMAC Instrumentation and Interface Standards*, IEEE 1982, ISBN 0-471-89737-X.

19. C. Fabjan, *Techniques and Concepts of High Energy Physics–III*, T. Ferbel, ed. (Plenum Pub. Corp.), 1985.

20. P. Gutierrez, *et al.*, "E706 Liquid Argon Calorimeter", *Proc. of the International Europhysics Conf. on High Energy Physics*, Bari, L. Nitti and G. Preparata, eds., (1986).

21. F. Lobkowicz, *et al.*, *Nucl. Instr. and Meth.* **A235** (1985), 332.

22. J.P. Mansour, PhD Dissertation, University of Rochester, 1989.

23. P. Lukens, and K. Ruddick, E-706 Internal Note 141.

24. Carlos Yosef, PhD Dissertation, Northeastern University, 1990.

25. G. Drake, *Nucl. Inst. Meth. in Phys. Res.* **A269** (1988), 68-81.

26. CDPACK Users Manual, Fermilab Computer Library

27. P. Gutierrez, E706 Internal Memo No. 126.

28. C. Blocker, *The Evils of Source Capacitance*, *Proc. Gas Sampling Calorimeter Workshop II*, Fermilab, (1985) 572–580.

29. V. Radeka, *IEEE Trans. Nucl. Sci.* **V21,1** (1974), 51–64.

30. M. Bertolaccini, *et al.*, *Nucl. Inst. Meth. in Phys. Res.* **A264** (1988), 399–406.

31. H.J. Klein, *et al.*, PATCHY Reference Manual, CERN Computing Library, 1983.

32. Fermilab Computing Department, "ACP Software User's Guide for Event Oriented Processing", FNAL #GA0001 (1988).

33. Sajan Easo, PhD Dissertation, Penn State University, 1989.

34. SPICE User's Guide, FNAL Computing Department Library PM0037, 1984.

35. P.D.D.S. Weerasundara, Private Communication.

36. R. Brun, *et al.*, *GEANT3* Users Guide, Cern Program Library No. DD/EE/84-1.

37. Armando Lanaro, PhD Dissertation, University of Rochester, 1989.

Appendix A

This appendix contains circuit diagrams for the LACAMP module described in Chapter 3. These are provided for reference purposes and as an aid to understanding the functionality of the LACAMP module. The diagram numbers are not complete because component placement diagrams have been removed for brevity.

AMPLIFIER
(ONE OF SIXTEEN)

BIASING
(ONE OF FOUR)

FAST OUT
(ONE OF EIGHT)

TO 4-ADDER
TO FAST OUTS
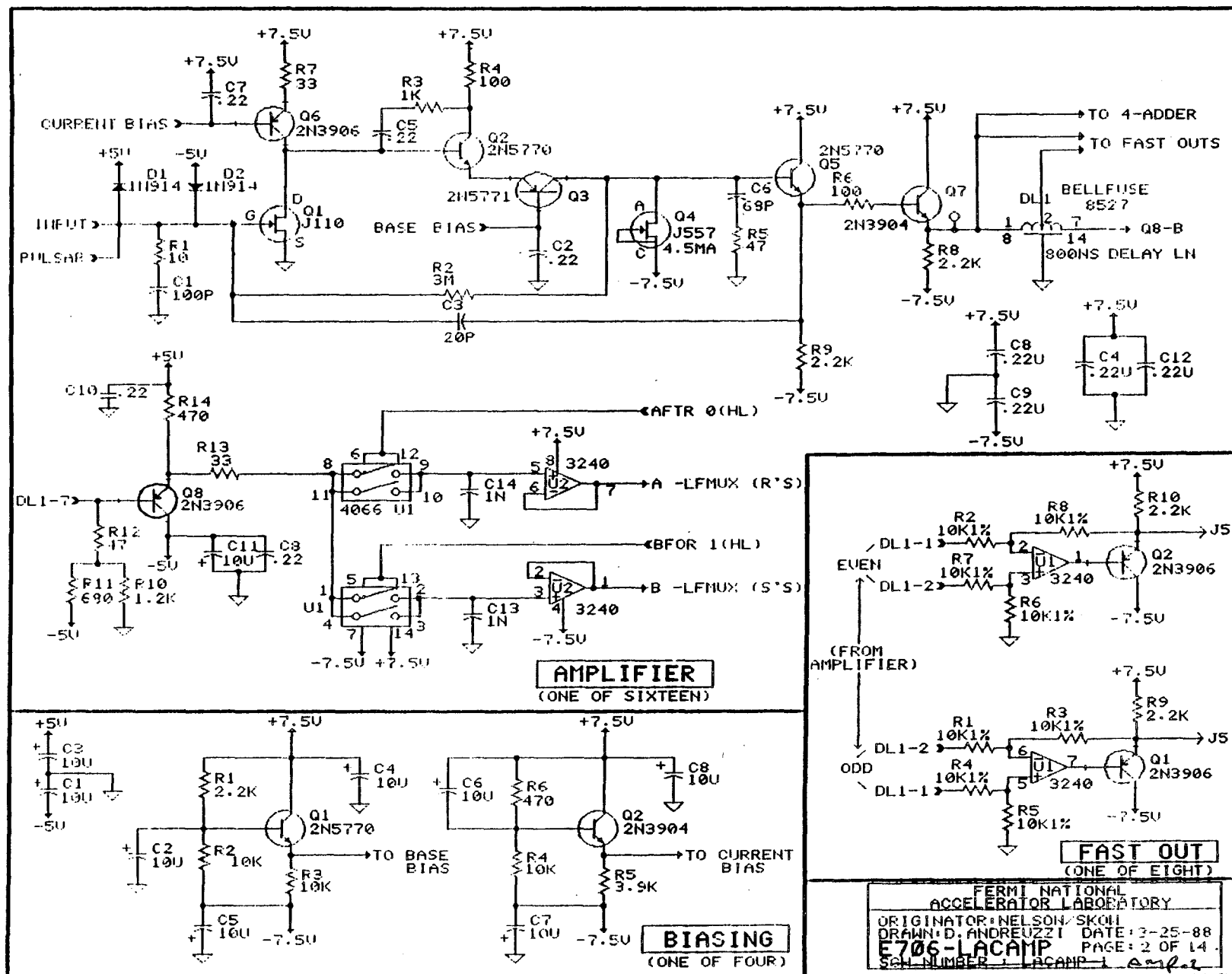
FERMI NATIONAL
ACCELERATOR LABORATORY
ORIGINATOR: NELSON/SKOH
DRAWN: D. ANDREUZZI   DATE: 3-25-88
E706-LACAMP   PAGE: 2 OF 14
SCH NUMBER : LACAMP-1   Amp.2

137

4-ADDER
(ONE OF FOUR)

BEFORE AND AFTER DRIVER

CALIBRATOR/PULSAR

FERMI NATIONAL
ACCELERATOR LABORATORY
ORIGINATOR: NELSON/D. SKOW
DRAWN: D. ANDREUZZI   DATE: 3-30-88
E706-LACAMP   PAGE: 4 OF 14
SCH. NUMBER 1 LACAMP-2

138

TVC
(ONE OF FOUR)

NOTE : TUCS 0 AND 2 ARE SIMILAR, AND DIFFER FROM TUCS 1 AND 3
(THAT ARE ALSO SIMILAR) ON THE PIN NUMBERS OF U1 AND U4
AS SHOWING.

TOP BUS DIGITAL SECTION

FERMI NATIONAL
ACCELERATOR LABORATORY
ORIGINATOR: DANE SKOW
DRAWN: D. ANDREUZZI   DATE: 4-12-88
E706-LACAMP   PAGE: 11 OF 14
SCH. NUMBER : LACAMP=5 Amp-11

140

BOT. BUS DIGITAL SECTION

TOP TDC MULTIPLEXING

TOP LF MUX

TOP ANALOG BUS

142

LF MUX
PICTORIAL CONNECTION

TDC MUX
PICTORIAL CONNECTION

NOTE: PIN 16=+7.5U
PIN 7 =-7.5U
PIN 8 = GRD.

E706-LACAMP PG. 7 OF 14
PICT.NUMBER : PCT-4

BOT BUS
J2

TOP BUS
J3

TO AMPLIFIER
CHANNELS
FROM MUQ MUX
OR PULSAR.

J5   J1   J4

```
 33  34                          8←33  34
 31  32 →0                       9←31  32
 29  30 →1                      10←29  30
 27  28 →2                      11←27  28
 25  26 →3                      12←25  26
 23  24 →4                      13←23  24
 21  22 →5                      14←21  22
 19  20 →6                      15←19  20
 17  18 →7                           17  18
 15  16 →8                           15  16
 13  14 →9                           13  14
 11  12 →10                          11  12
  9  10 →11                           9  10
  7   8 →12                           7   8
  5   6 →13                           5   6
  3   4 →14                           3   4
  1   2 →15                           1   2
```
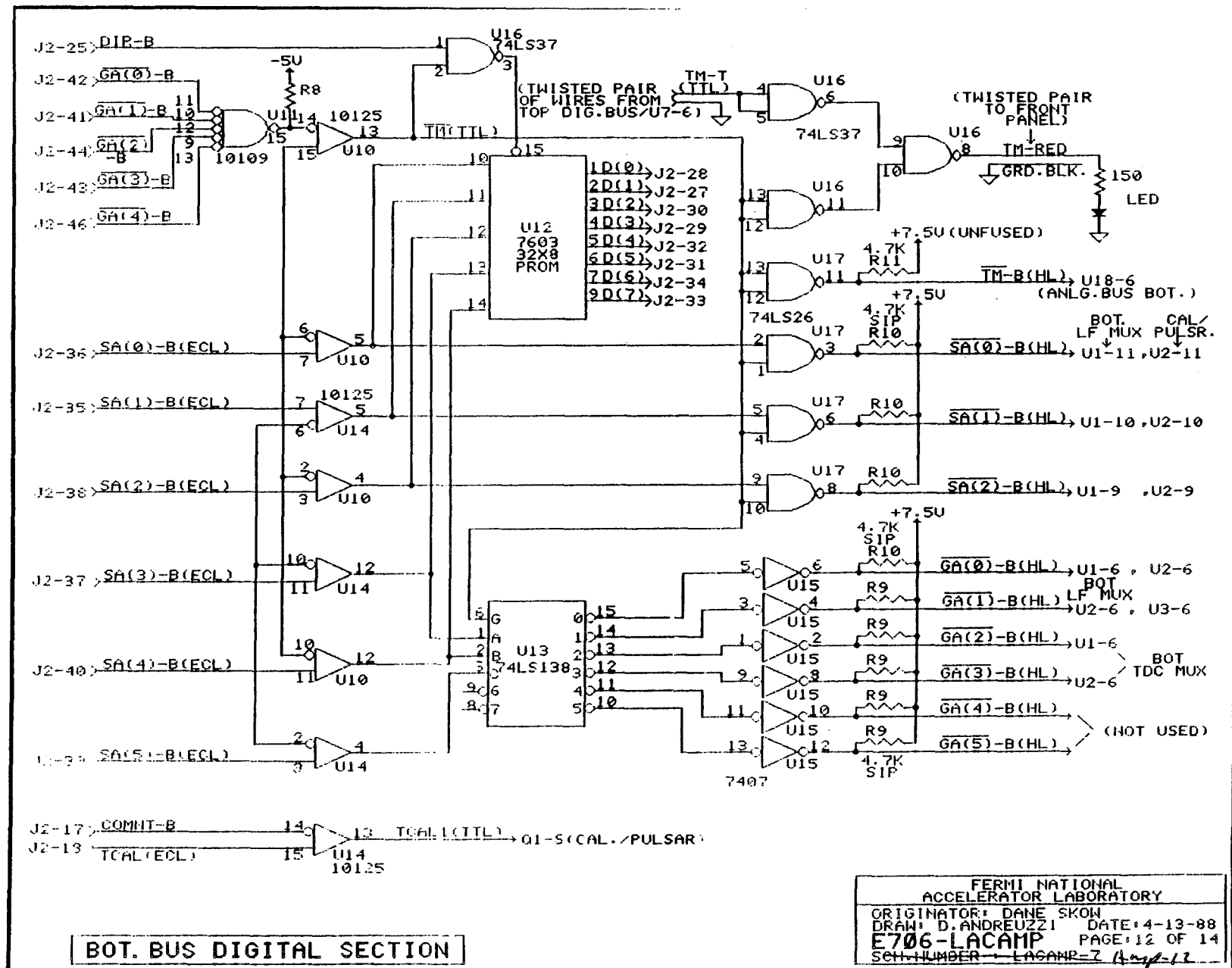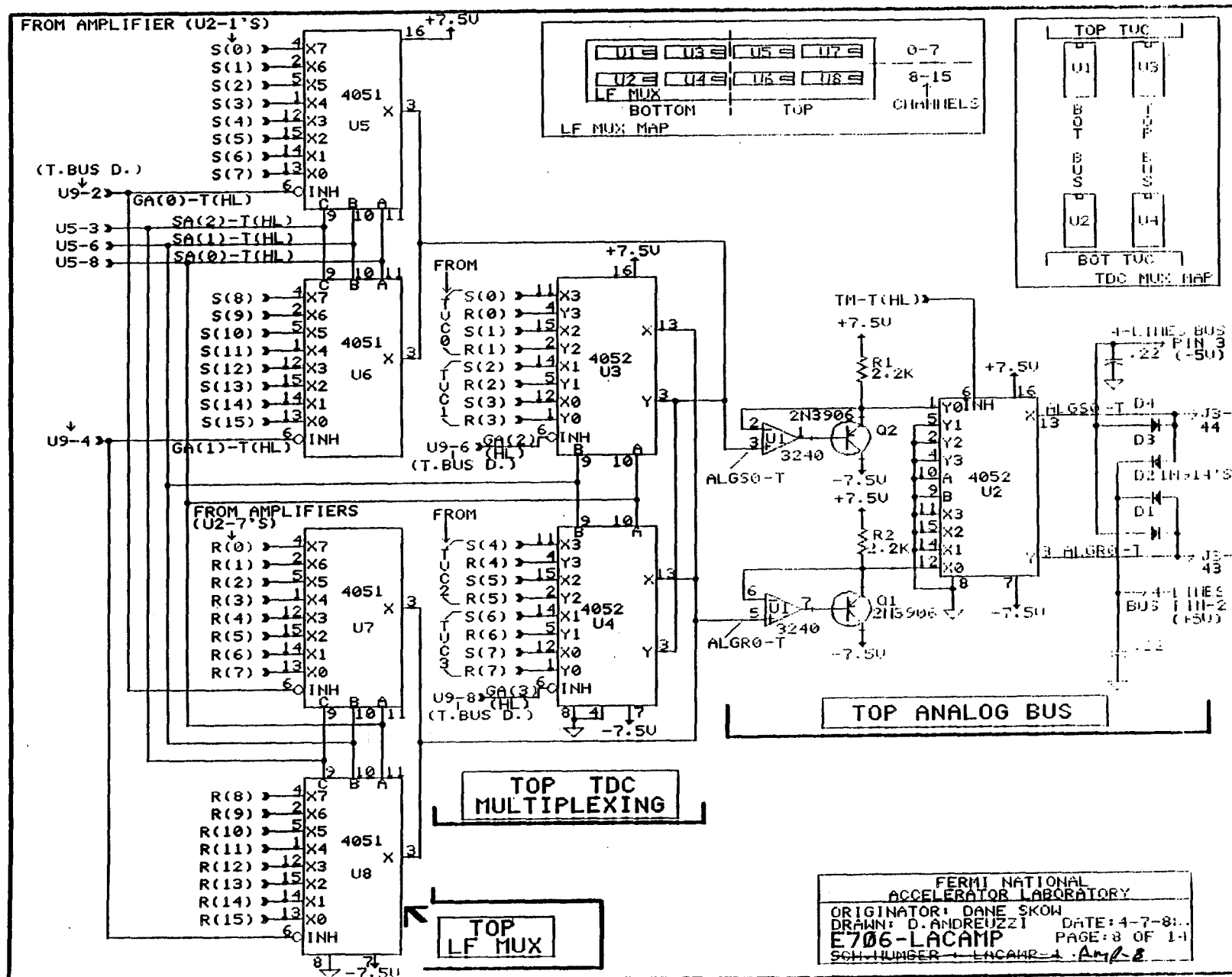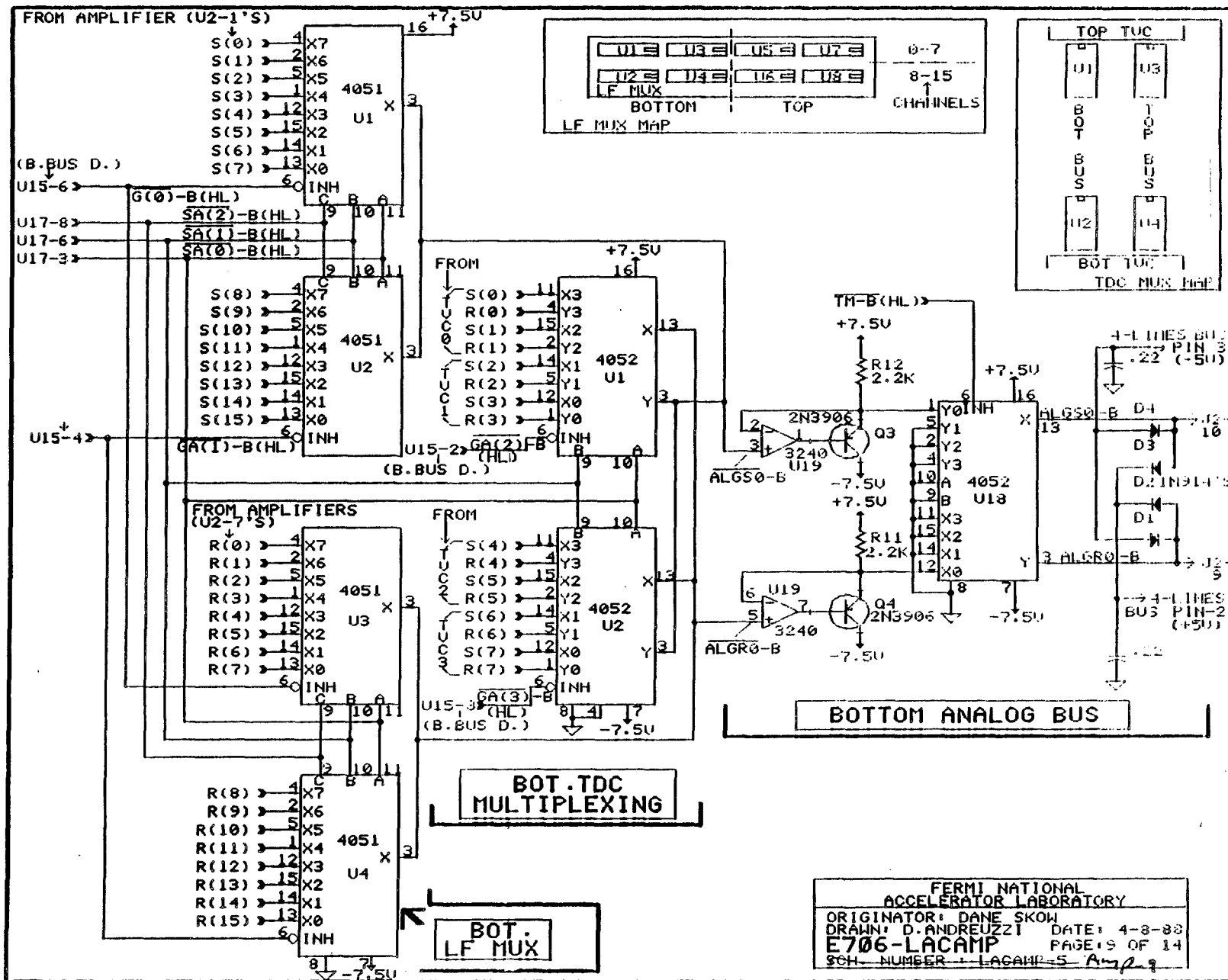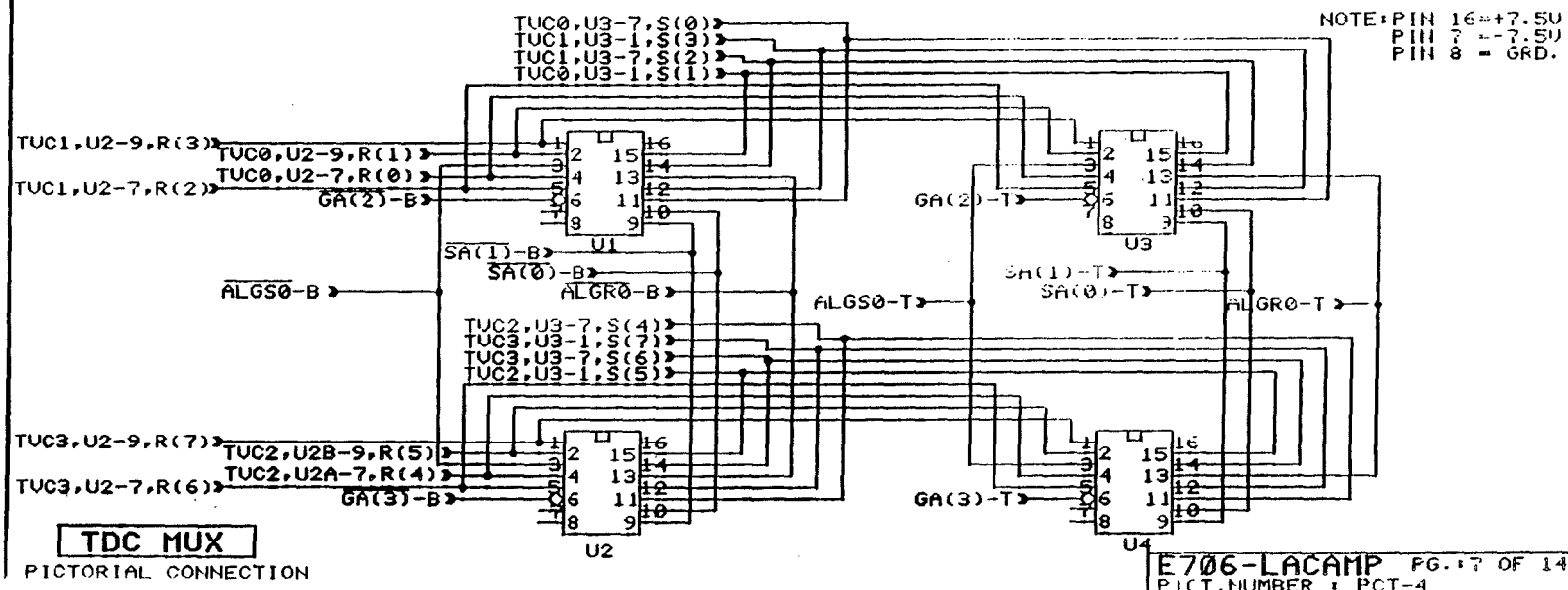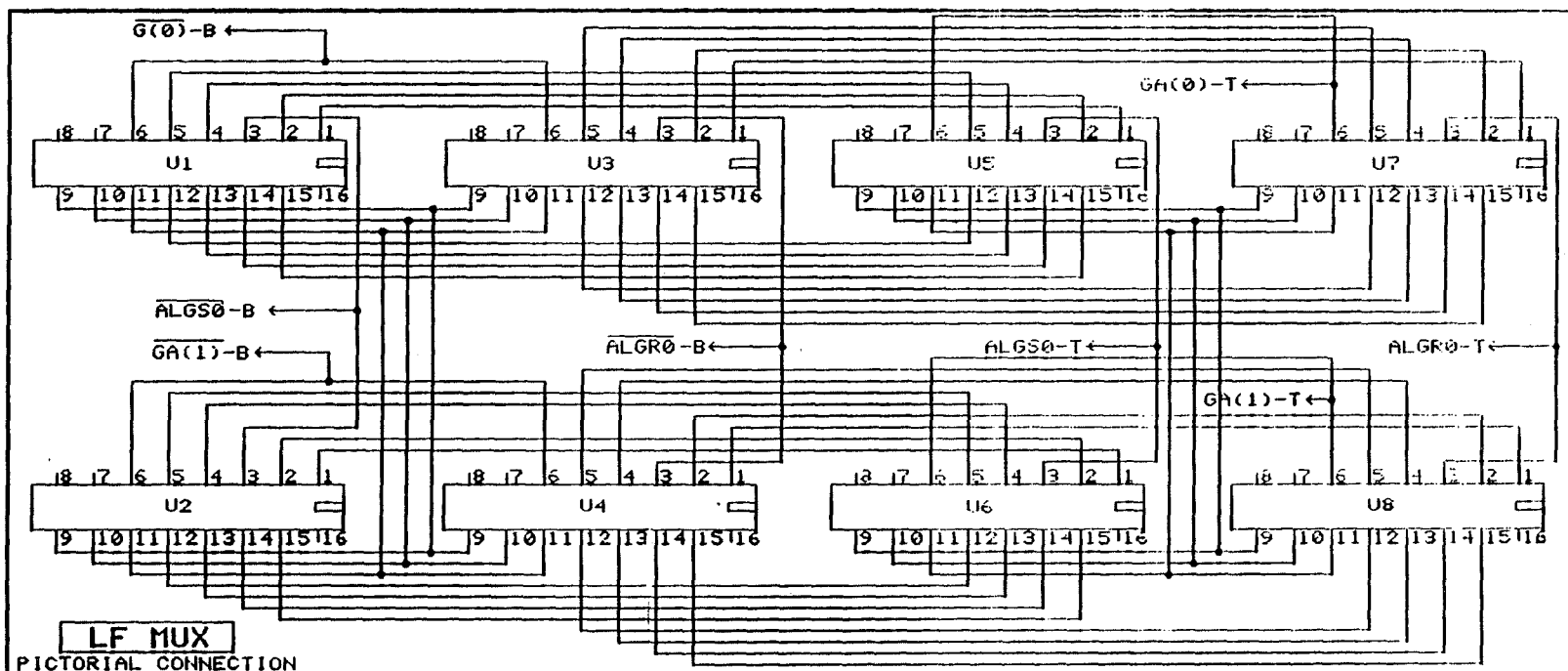
FROM FAST OUTS
TO READ OUT BOARD.
(FRONT PANNEL CONN.)

```
-6.0V-B←49   50→GND               +6.0V-T←49   50→GND
-8.5V-B←47   48→-16.0V-B          +16.0V-T←47   48→+8.5V-T
GLRST-B←45   46→GA(4)-B           ALGR1-T←45   46→ALGS1-T
 GA(3)-B←43   44→GA(2)-B          ALGR0-T←43   44→ALGS0-T
 GA(1)-B←41   42→GA(0)-B                  41   42
 SA(5)-B←39   40→SA(4)-B                  39   40
 SA(3)-B←37   38→SA(2)-B                  37   38
 SA(1)-B←35   36→SA(0)-B           AFTR1←35   36→BFOR1
  D(7)-B←33   34→D(6)-B            COMNT←33   34→R/S
  D(5)-B←31   32→D(4)-B            AFTR2←31   32→AFTR0
  D(3)-B←29   30→D(2)-B            BFOR0←29   30→RESET
  D(1)-B←27   28→D(0)-B            DIR-T←27   28→STRB-T
   DIR-B←25   26→STRB-B            USER STATUS←25  26  GND
USER STATUS←23   24→GND            D(7)-T←23   24→D(6)-T
         21   22                   D(5)-T←21   22→D(4)-T
         19   20                   D(3)-T←19   20→D(2)-T
 COMNT←17   18→TCAL                D(1)-T←17   18→D(0)-T
 VCALR←15   16→VCALS               SA(5)-T←15   16→SA(4)-T
         13   14→THRSH             SA(3)-T←13   14→SA(2)-T
ALGR1-B←11   12→ALGS1-B            SA(1)-T←11   12→SA(0)-T
ALGR0-B←9   10→ALGS0-B             GA(3)-T←9   10→GA(2)-T
 0VREF←7    8→+4VREF               GA(1)-T←7    8→GA(0)-T
         5    6                    GLRST-T←5    6→GA(4)-T
+16.0V-B←3    4→+8.5V-B            -8.5V-T←3    4→-16.0V-T
 +6.0V-B←1    2→GDN                -6.0V-T←1    2  GND
```

```
0←15  16
1←13  14
2←11  12
3←9   10
4←7    8
5←5    6
6←3    4
7←1    2
```

```
 33  34
 31  32
 29  30
 27  28
 25  26
 23  24
 21  22
 19  20
 17  18
```

TO AMPLIFIER
CHANNELS.
FROM MUQ MUX
OR PULSAR.

LAC AMP CONNECTORS
NOTE: CONNECTORS SHOWED FROM SOLDER SIDE.

145